U.PORTO
FEUP FACULDADE DE ENGENHARIA
UNIVERSIDADE DO PORTO

Asymmetries, co-current flow and interaction of Taylor drops rising in vertical tubes

A thesis submitted in part fulfilment of the requirement for the degree of Doctor, Doctoral Program in Chemical and Biological Engineering, Faculty of Engineering, Universidade do Porto, by

Filipe José Neto Direito

Supervised by
João Bernardo Lares Moreira de Campos
João Mário Rodrigues Miranda
at Centro de Estudos de Fenómenos de Transporte

centro de estudos de fenómenos de transporte
CEFT

Departamento de Engenharia Química
Faculdade de Engenharia da Universidade do Porto
Porto, Portugal
July 2017

POPH QUALIFICAR É CRESCER.
QREN QUADRO DE REFERÊNCIA ESTRATÉGICO NACIONAL PORTUGAL 2007.2013
GOVERNO DA REPÚBLICA PORTUGUESA
UNIÃO EUROPEIA
Fundo Social Europeu

Filipe José Neto Direito
deq11009@fe.up.pt

This thesis was developed for the Doctoral Program in Chemical and Biological Engineering, at:

Departamento de Engenharia Química
Faculdade de Engenharia da Universidade do Porto
Rua Dr. Roberto Frias, s/n, 4200-465, Porto, Portugal
www.fe.up.pt
feup@fe.up.pt

The work was developed in Centro de Estudos de Fenómenos de Transporte supervised by:

João Bernardo Lares Moreira de Campos
Departamento de Engenharia Química
Faculdade de Engenharia da Universidade do Porto
Rua Dr. Roberto Frias, s/n, 4200-465, Porto, Portugal
jmc@fe.up.pt

João Mário Rodrigues Miranda
jmiranda@fe.up.pt

This thesis was funded by FEDER funds through the Operational Programme for Competitiveness Factors COMPETE and National Funds through FCT (Fundação para a Ciência e a Tecnologia) under the project PEst-OE/EME/UI0532 and by Ph.D. Grant SFRH/BD/79264/2011.

Acknowledgments

To my family and friends.

To Professor João Campos for the personal and academic support, the availability and the guidance. For the inspiring leadership. Also for providing an environment of responsibility and freedom and for creating, providing and understanding the importance of a friendly working environment in the pursuit of success. To Dr João Mário Miranda for the personal and academic support, the guidance and the knowledge that shared. Also, for the amazing questions and ideas that raised throughout this work. The success of this work is thus specially dedicated to my supervisors, Professor João Campos and Dr João Mário Miranda.

To Dr José Daniel Araújo for the tremendous help during the very beginnings of my CEFT journey, but also for the sharing of amazing knowledge regarding slug flow throughout the entire period of this work.

To Ana Morgado and Luís Rocha, my co-authors in my second journal article, for their help in that part of my work. To them, as well, for their kindness and companionship.

A huge gratitude to João Carneiro. For the friendship, the companionship, the help, the doubts, the debates, and the amazing mood that he always creates in the workplace. Without João Carneiro, my journey in CEFT would have been totally different. Thank you very much. I hope I contributed to your own journey half of your contribution to mine.

To Dr Erica Doutel for the friendship and companionship and for all the help throughout this thesis.

To Soraia Neves and Marta Santos for their companionship.

To Dr Patrícia Sousa for the kindness and for creating a friendly environment in workplace. To Dr Patrícia Sousa also for sharing her experience in research and academic affairs.

To Dr Renato Sousa, Tânia Dinis and Samir Sadek for the kindness and companionship.

To Francisco Pimenta for the great tips regarding OpenFOAM and to Josefina Ferreira for the help with old lab materials.

I must also mention Joana Ferreira, Hélder Xavier Nunes, Filipe C. Silva, Mónica Silva, Antonio Jose Acero, Pierre Ballesta, Rui Ferreira, André M. Fonseca, Isabel Moreira, Andreia Silva.

To Pedro Magalhães for the companionship during lunch and breaks.

To Nuno Guerreiro and Luís Carlos Matos for the help in the lab.

To Professor Maria do Carmo Pereira and Dr Joana Loureiro for the help with the interfacial tension measurements.

To all other people that in some way contributed for this work.

To FEUP and CEFT.

Abstract

There is an increasing interest in multiphase flow patterns due to their relevance in several operations in industrial processes. The aim of the present work was to improve the knowledge of an important multiphase flow pattern: slug flow in liquid-liquid vertical tubes. The strategy defined was based on three pillars: tools, design of testing conditions and assessment of the elementary flow characteristics. Regarding the tools, Computational Fluid Dynamics (CFD) was chosen due to its flexibility and ease of use. Some lab experiments were also conducted, but only to validate the numerical results. The design of testing conditions followed a dimensional analysis that yielded relevant dimensionless numbers representing the forces involved in the flow. Finally, concerning the strategy to understand the phenomena, the first simulations were conducted with the simplest element in the flow: an axisymmetric Taylor drop rising in a tube filled with a denser stagnant liquid. Afterwards, complexity was added and the results interpreted (drop asymmetries, flowing continuous phase and drops interaction).

For drops rising in stagnant continuous phase, the results showed that interfacial tension and viscous forces decrease drop velocity, while buoyancy has the opposite effect. The disturbed distance in the continuous phase below the drop depends mainly on the drop Reynolds number, being small for axisymmetric drops. Regarding asymmetries, three different behaviors were found: an axisymmetric region, an asymmetric region for small viscosity ratios and an asymmetric region for high viscosity ratios.

By the insertion of co-current, the balance between gravity and convective co-current effects was found to be determinant to the drops behavior. Furthermore, the increase of the continuous phase velocity promotes inertial effects and the appearance of closed recirculations regions below the drop. High enough continuous phase velocity also caused the inner portion (near the tube axis) of the continuous phase to move, in average, at the drop velocity. A pre-existing gas-liquid correlation that predicts drop velocity was adapted according to the results of this work. Moreover, it is observed that the increase of the viscosity ratio approximates the macro scale data to a limit defined by micro scale behavior.

Interaction of two drops in axisymmetric conditions is very limited.

Due to the difficulties presented by asymmetric behavior, it was not possible to reach a full descriptive model for liquid-liquid slug flow. Hence, future work concerns overcoming challenges such as the serpentine-like effect found in some asymmetric ranges due to its importance in petroleum industry. More work is also required to produce enough data to develop a one-dimensional code able to easily predict liquid-liquid slug flow behavior.

In general, the present work succeeded in producing important knowledge regarding liquid-liquid slug flow.

Keywords: slug flow, Taylor drop, CFD, oil-water flow.

Sumário

Existe um crescente interesse em escoamentos multifásicos devido à sua importância em processos industriais. O objectivo do presente trabalho foi dar um contributo no sentido do aumento do conhecimento de um importante padrão de escoamento bifásico: o escoamento de gotas tubulares em tubos verticais. A estratégia definida assentou em três pilares: ferramentas, desenho das condições a testar e estratégia para avaliação das características do escoamento. Relativamente às ferramentas, a dinâmica de fluidos computacional (CFD) foi a escolhida devido à sua flexibilidade de utilização. O desenho das condições a testar, seguiu uma análise dimensional da qual resultaram números adimensionais representativos das forças envolvidas no escoamento. Finalmente, relativamente à estratégia para compreensão dos fenómenos, as primeiras simulações foram realizadas com o elemento mais simples do escoamento: uma gota de Taylor axissimétrica em movimento ascendente num tubo preenchido com um líquido mais denso parado. Depois, foi adicionada complexidade e os resultados interpretados (assimetrias nas gotas, fase contínua em escoamento e interacção entre gotas).

Para gotas em ascensão em fase contínua parada, os resultados demonstraram que as forças interfaciais e de viscosidade reduzem a velocidade da gota, enquanto que as forças de impulsão têm o efeito contrário. A distância perturbada na fase contínua abaixo da gota depende principalmente do número de Reynolds da gota, sendo este pequeno para gotas axissimétricas. Relativamente a assimetrias, três diferentes comportamentos, regiões num mapa de grupos adimensionais, foram observados: uma região axissimétrica, uma região assimétrica para razões de viscosidade pequenas e uma zona assimétrica para razões de viscosidade elevadas.

Adicionando o escoamento em co-corrente, o balanço entre os efeitos gravitacionais e convectivos revelou-se determinante para o comportamento das gotas. Além disso, o aumento da velocidade da fase contínua promoveu efeitos inerciais e o surgimento de recirculações fechadas abaixo da gota, esteira. Uma velocidade da fase contínua suficientemente elevada também fez com que a porção interna de fluido (junto ao eixo do tubo) de fase contínua se mova, em média, à velocidade da gota. Uma correlação já existente para gás-líquido que prevê a velocidade da bolha tubular foi extendida para escoamento líquido-líquido de acordo com os resultados deste trabalho. Adicionalmente, observou-se que o aumento da razão de viscosidades faz aproximar a macro escala de um limite definido pelo comportamento em micro escala.

A interacção entre duas gotas axissimétricas é muito limitada.

Devido a dificuldades em lidar com comportamentos assimétricos, ainda não foi possível desenvolver um modelo geral para o escoamento de gotas tubulares. Assim, o trabalho futuro passará por superar desafios tais como o efeito de gota em forma de serpentina observado em algumas regiões assimétricas, pois estas regiões são importantes para a indústria do petróleo. Também será necessário produzir mais dados de escoamento que permitam desenvolver um código unidimensional capaz de facilmente prever o comportamento do escoamento de gotas tubulares.

Em geral, o presente trabalho conseguiu aumentar significativamente o conhecimento que existia sobre o escoamento de gotas tubulares.

Palavras-chave: escoamento de gotas tubulares, gota de Taylor, CFD, escoamento óleo-água.

Contents

List of Figures

List of Tables

Nomenclature

Roman

C	constant in linear relationship between V_{TC} and U_{C}
D	tube diameter
Ca_{C}	capillary number
Co	Courant number
Eo	Eötvös number
$\vec{f_\sigma}$	interfacial tension force term in momentum equation
Fr	Froude number
$\mathrm{Fr}_{\mathrm{2D}}$	Froude number in the 2D axisymmetric model
$\mathrm{Fr}_{\mathrm{3D}}$	Froude number in the 3D model
g	acceleration of gravity
M	Morton number
N_{f}	inverse viscosity number
p	pressure
Re	Reynolds number
$S_{v_{\mathrm{P}}}$	Symmetry parameter
t	time
U_{C}	continuous phase superficial velocity
u^*	ratio between U_{C} and V_{T}
v	velocity
$v_{\mathrm{P}i}$	maximum vertical velocity component
V_{T}	drop terminal velocity
V_{TC}	drop velocity in co-current
Z_{I}	influence distance above the drop
Z_{III}	influence distance below the drop

Greek

α	volume fraction
$\Delta\rho$	density difference
ϕ	generic scalar variable
μ	viscosity
ρ	density
σ	interfacial tension

Subscripts and superscripts

$_{\mathrm{a}}$	average (fluid cell)
$_{\mathrm{C}}$	continous phase
$_{\mathrm{D}}$	dispersed phase
*	ratio between phases

1

Introduction

1.1 Motivation

Multiphase flows occur in several industries, such as chemical, nuclear or petroleum (Aziz et al., 2015; Babadagli, 2007; Bannwart et al., 2009; Bordeaux Rego et al., 2017; Clark, 1969; Omebereiyari et al., 2008; Seyfried and Freundt, 2000). One of the foremost multiphase patterns is slug flow.

The present work deals with liquid-liquid vertical slug flow at the macro scale. Liquid-liquid slug flow consists of long bullet-shaped drops flowing in a continuum of another liquid. The intermittent character of slug flow can be the cause of severe operational problems. On the other hand, slug flow can be used to transport viscous liquids and also to promote mass transfer between phases. In the particular example of exploitation and oil transportation in the petroleum industry, the usage of enhanced oil recovery techniques creates multiphase flows with oil and water-based phases.

Therefore, it is of major interest to understand liquid-liquid slug flow, in order to use it, or to avoid it. However, unlike the gas-liquid case, liquid-liquid slug flow is still not yet well explored and understood. The present work intends to fill the gap in vertical liquid-liquid slug flow knowledge. For the pursuit of such purpose, the flow of Taylor drops rising in vertical tubes is the scope of the present work.

1.1.1 Oil-water slug flow

Despite the increase in renewable energy technologies, petroleum industry will still be a major player in global economy for the next decades.

Oil reservoirs are typically at temperatures between 100 and 150 °C and at pressures in the 300 to 400 bar range (Verweij, 1993). Fluid motion in wells generally involves more than one phase, and the behavior depends on the magnitude of the acting forces (inertia, buoyancy, viscous and interfacial tension) (Brill and Mukherjee, 1999).

Total world oil reserves are estimated to be distributed by between conventional oil (30 %) and 40 % of heavy or extra-heavy oils and 30 % of oil sands and bitumen (Alboudwarej et al., 2006). In recent years, there is a growing interest in the exploitation of heavy oil wells (Alboudwarej et al., 2006). The physical properties of heavy oil make it difficult to extract – it has high density and high viscosity (can be more than as 1 kPa s – Alboudwarej et al. (2006)). Because of the operational difficulties, enhanced oil recovery techniques (EOR) are necessary (Babadagli, 2007; Lyons and Plisga, 1999; Thomas, 2008). Those techniques include water flooding, chemical flooding (surfactant, polymer, etc) or cyclic stream soak, which create multiphase flows with high content in two liquid phases: water and oil (Alboudwarej et al., 2006; Bordeaux Rego et al., 2017; Flores et al., 1999; Thomas, 2008; Sheng et al., 2015). Furthermore, water-oil flows might also be created in order to lubricate the transport of heavy oils in pipes (Kwon et al., 2015).

Studies on water-oil flow include that of Mandal et al. (2010) which used a 0.012 m diameter tube to study co-current flow of water and kerosene. Slug flow was found to exist in a wide range of flow conditions.

Yang et al. (2017) conducted co-current tests with a white oil and a polyacrylamide water solution, observing slug flow when high polymer concentration was used.

Serapião and Bannwart (2013) performed air-water-oil tests in a vertical 2.84 cm diameter glass tube, using an oil with a density of 971 kg m^{-3} and a viscosity of 5 Pa s. They found a three-phase flow of oil in water emulsion with intermittent long oil drops and air bubbles. This occurs for high oil superficial velocities comparing to water flow.

Deformed large drops of oil in water were found by Hasan and Kabir (1990); Bannwart et al. (2004).

Pietrzak et al. (2017) performed a three phase flow study in a 0.03 m diameter tube. For water dominant flow with low air superficial velocity, small drops of oil and bubbles were observed in a continuum of water, with intermittent large plugs of oil (some deformed drops). Other three phase flow studies include those of Spedding et al. (2000, 2005) and Woods et al. (1998).

The clear interest of understanding liquid-liquid flows in petroleum industry is often shadowed by the difficulties in operating lab or pilot scale installations, especially concerning high pressure and temperature conditions at oil wells and nearby tubing. Computational Fluid Dynamics (CFD) appears as an easy and efficient solution to this problem. With CFD, it is possible to study different flow patterns at severe operating conditions. Slug flow is one of the most important multiphase flow patterns, and the present work is an important step to understand more about liquid-liquid slug flow.

1.2 Introduction to liquid-liquid slug flow and Taylor drops

To understand slug flow, consider a case where two immiscible liquids flow in a vertical tube. One of those liquids, the heavier one, constitutes a continuous phase where drops of the other liquid, which constitute the dispersed phase, are present. If the flow rate of the dispersed phase undergoes a significant increase, very large drops occupying almost all the tube cross section, start to form – Taylor drops, by analogy to Taylor bubbles (Davies and Taylor, 1950; Mandal et al., 2008). A flow where a continuum of a liquid contains Taylor drops of another liquid is called liquid-liquid slug flow.

Slug flow is important due to its effects on heat and mass transfer rates in several industrial processes. Hydrocarbon transportation in pipes is another important example where slug flow happens. In particular, due to the increasing demand in oil well extraction, there is a growing interest in liquid-liquid slug flow occurrence in vertical pipes (Bannwart et al., 2004; Mandal et al., 2010).

The most basic element of slug flow is the Taylor drop. The present work deals with Taylor drops (dispersed phase) rising in a vertical tube filled with a denser liquid (continuous phase).

Taylor drops are typically long bullet-shaped drops. It is expected that a rising solitary drop reaches a constant velocity (V_T), in a very short distance from its injection or formation point. The heavier liquid that constitutes the continuous phase is forced, by the drop upward flow, to flow down in the narrow film that is formed between the drop and the pipe wall (Mandal et al., 2008). The flow in the film becomes fully developed and the drop velocity becomes independent of the drop length. The shape of the rear part of the drop is closely related to the flow regime and sometimes can show oscillations. Below the drop, depending on the regime, closed recirculations can be formed.

Another important characteristic of Taylor drops concerns the existence or non-existence of axisymmetry.

In order to understand Taylor drops continuous flow, one must consider first the simpler case, a Taylor drop rising in a stagnant liquid. That case is presented in the following subsection. The second subsection extends the analysis to a Taylor drop flowing in co-current with the continuous phase.

Note that the present work deals solely with Newtonian liquids.

1.2.1 Single Taylor drop in stagnant continuous phase

Hayashi et al. (2011) performed a dimensional analysis identifying the relevant forces involved in liquid slug flow in a stagnant liquid column: inertial, viscous, surface tension and buoyant. This is analogous to Taylor bubbles (Goldsmith and Mason, 1962; Fabre and Line, 1992; Morgado et al., 2016). However, in liquid-liquid, the viscosity of the dispersed phase (Taylor drop) is also relevant.

Five dimensionless numbers are needed to characterize liquid slug flow in a stagnant liquid column. The Froude number relates inertia and gravity forces:

$$\mathrm{Fr} = \frac{V_\mathrm{T}}{\sqrt{\Delta\rho\, gD/\rho_\mathrm{C}}}, \tag{1.1}$$

where ρ is the density, D stands for the tube diameter, g for the acceleration of gravity. Finally, $\Delta\rho = \rho_\mathrm{C} - \rho_\mathrm{D}$, where the subscripts "$_\mathrm{D}$" and "$_\mathrm{C}$" stand for dispersed and continuous phase. The Froude number includes the drop terminal velocity (V_T), and it is the main output from studies dealing with Taylor drop velocity.

Two other dimensionless numbers are also of foremost importance:

$$\mathrm{Eo} = \frac{\Delta\rho\, gD^2}{\sigma}, \tag{1.2}$$

$$\mathrm{M} = \frac{\Delta\rho\, g\mu_\mathrm{C}^4}{\rho_\mathrm{C}^2\, \sigma^3}, \tag{1.3}$$

where Eo is for Eötvös number (ratio between buoyancy and interfacial forces) and M the Morton number (gravity, viscosity and surface tension forces). μ stands for viscosity and σ for the interfacial tension between the two liquids.

The ratios between the liquids properties are the remaining dimensionless numbers required to complete the dimensional analysis:

$$\rho^* = \frac{\rho_\mathrm{D}}{\rho_\mathrm{C}}, \tag{1.4}$$

$$\mu^* = \frac{\mu_\mathrm{D}}{\mu_\mathrm{C}}. \tag{1.5}$$

The combination of Eötvös number, Morton number and viscosity ratio allow for the characterization of the Taylor drop phenomena.

When Eötvös number is high and the viscosity ratio is low enough, the liquid-liquid isolated drop case approaches the behavior of a Taylor gas bubble rising in a liquid contained in a macro tube. That happens because the gravity effects are predominant due to the high density difference and/or to the low interfacial tension force.

On the other hand, when Eötvös number is low, Morton is required to assess the importance of the viscous forces. Low Eötvös and high Morton numbers implicate a high viscosity of the continuous phase. On such occasions, if the viscosity ratio is high, such combination implies that, at the macroscale, both fluids have close densities and so viscous effects are predominant. For low Eötvös, low Morton numbers and low viscosity ratio, the flow should resemble a gas Taylor bubble flowing in a liquid contained in a micro tube (surface tension effects are predominant).

In the present work, the continuous phase is denser than the dispersed phase (rising drops): $\rho^* < 1$ Note also that the presented dimensionless numbers hold for Taylor drops because in gas liquid $\rho^* \approx 0$, $\Delta\rho \approx \rho_\mathrm{C}$ and $\mu^* \approx 0$.

Furthermore, the ratio between the diameter of the drop volume-equivalent sphere and the pipe diameter (d_S/D) gives information on the drop size.

Even though the presented dimensionless numbers suffices for the description of the phenomena, sometimes it is useful to combine them to yield other relations. As such, consider the inverse viscosity number,

$$\mathrm{N_f} = \left(\frac{\mathrm{Eo}^3}{\mathrm{M}}\right)^{1/4} = \frac{\sqrt{\Delta\rho\,\rho_C g D^3}}{\mu_c}. \tag{1.6}$$

1.2.2 Single Taylor drop in co-current flow

When Taylor drops rise in co-current flowing liquids (laminar regime), the velocity will be the result of the contributions of two effects: the terminal velocity and the co-current flow. Therefore, V_{TC} is here used for the drop velocity and U_{C} for the continuous phase velocity.

Due to the continuous phase flow, one must always consider the Reynolds number, which gives information on the flow regime:

$$\mathrm{Re_C} = \frac{\rho_{\mathrm{C}}\,U_{\mathrm{C}}\,D}{\mu_{\mathrm{C}}}. \tag{1.7}$$

In the present work, the regime of the continuous phase is laminar.

It is also important to consider the Reynold number based on the dispersed phase velocity:

$$\mathrm{Re_D} = \frac{\rho_{\mathrm{C}}\,V_{\mathrm{TC}}\,D}{\mu_{\mathrm{C}}}. \tag{1.8}$$

1.3 Gas-liquid slug flow literature overview

There is already an extensive knowledge on gas-liquid slug flow and Taylor bubbles. Moreover, there is an obvious analogy between Taylor drops and Taylor bubbles. Therefore, it is important to make a summary of gas-liquid slug flow.

Early studies include those of Davies and Taylor (1950); Dumitrescu (1943); Nicklin et al. (1962); White and Beardmore (1962); Zukoski (1966).

White and Beardmore (1962); Collins et al. (1978) performed studies that concluded about the relevant properties: gravity, continuous phase density and viscosity, surface tension and tube diameter. Furthermore, White and Beardmore (1962) mapped Froude number as a function of Morton number and Eötvös number.

The bubble terminal velocity rising in a stagnant liquid has been the subject of several works. Early studies set the Taylor bubble velocity in stagnant liquids to be between $0.328\sqrt{gD}$ and $0.351\sqrt{gD}$ for inertial dominated regime. This result has an important influence both on Taylor bubbles and Taylor drops as it sets an upper limit for the Froude number. Later works (Viana et al., 2003; Hayashi et al., 2011) relate the Froude number to the other dimensionless numbers and confirm the upper limit at about 0.35. Brown (1965) related bubble terminal velocity and its film thickness and velocity profile. Regarding the wake, Campos and Carvalho (1988) performed experiments where several regimes were identified.

Araújo et al. (2012) performed a detailed numerical study on Taylor bubbles, describing velocity profiles, film thickness and nose radius. Furthermore, bubble shapes and wake characteristics were also studied, where closed recirculations tend to appear for low Morton number and high Eötvös number (Araújo et al., 2012). Detailed numerical studies regarding the flow between interacting Taylor bubbles where performed by Araújo et al. (2013*b*,*a*).

Regarding the bubble velocity in co-current flow, Nicklin et al. (1962) found that the bubble velocity results from the sum of the terminal velocity and of the continuous phase velocity contribution. The latter is a linear contribution which depends on the system dimensionless groups (Fabre and Line, 1992) – a constant C multiplied by the continuous phase velocity. Collins et al. (1978) proposed $C = 2.27$ for laminar regime. In a later work, (Bendiksen, 1985) proposed a function of Eötvös number for laminar regime with an asymptotic limit on $C = 2.29$.

Pinto et al. (1998) obtained similar values. They also related the liquid Reynolds number to the wake region behavior. Nogueira et al. (2006) reported an experimental study where three types of wakes were observed at the rear of Taylor bubbles. Lu and Prosperetti (2009) performed a numerical study on the effect of Eötvös and Morton numbers. They reported a relationship between the distance, below the bubble, disturbed by the bubble flow and the velocity of the continuous phase, observing very long recirculations in some conditions. Quan (2011) studied numerically systems with a density ratio of 0.01, reporting bubble shapes and detailed velocity profiles. They observed that an increase in the continuous phase velocity elongates the bubble and tends to create flow separation below the bubble.

Thin protuberances on the bottom edges of the bubbles ("skirts" – (Viana et al., 2003; Ray and Prosperetti, 2014)) were also reported on the mentioned numerical studies of Lu and Prosperetti (2009); Quan (2011).

1.4 Taylor drops – literature overview

The earlier studies of Taylor drops rising in vertical tubes trace back to the works of Brown and Govier (1961); Govier et al. (1961); Zukoski (1966).

Mandal et al. (2007, 2009) made a theoretical analysis to predict the terminal velocity by adopting a viscous potential flow analysis. They obtained an equation explicit in Froude number (and on terminal velocity, as well), which is dependent on the density of the liquids, surface tension, pipe diameter and continuous phase viscosity. Moreover, the equation contains a drop shape parameter that depends on the drop nose shape. Equations developed in the above works (Mandal et al., 2007, 2009) are limited to conditions where the effect of drop viscosity is negligible.

Mandal et al. (2007, 2008) also performed experiments with values of $4 < \mathrm{Eo} < 230$ and $10^{-13} < \mathrm{M} < 10^{-10}$. Density ratios were between 0.65 and 0.88 and viscosity ratios between 0.68 and 1.2. The interfacial tension for the pairs of liquids used lies between 0.02 and 0.06 Nm^{-1}. They used a 1.5 m long perspex pipe, which allows for visualization of the inside. They used water, kerosene, brine, benzine, ciclohexane and 2-heptanona. Mandal et al. (2009) performed further experimental studies concerning identical systems. A wake region was observed, distinguishable due to the presence of small dispersed drops. They claim that the drop shape for their conditions was axisymmetric. In some drops, the bottom part showed oscillations with apparently no periodic pattern (analogous behavior can be found in Taylor bubbles).

Hayashi et al. (2011) performed lab experiments and CFD simulations to study the terminal velocity of a rising Taylor drop. The experimental conditions consisted of a density ratio around 0.8, a viscosity ratio between 0.1 and 20, and a surface tension between 0.02 and 0.04 Nm^{-1}, from the usage of glycerin-water solutions as continuous phase and several silicon oils as dispersed phase. The diameters of the tubes were between 11 and 31 mm, the Eötvös number between 10 and 100, and the Morton number ranged between 2×10^{-5} and 0.35. They focused on drop shapes cataloging and on the development of a correlation to predict Froude number. They claim that the density ratio does not influence Froude number and they also observed that when the continuous phase viscosity is much higher than the dispersed phase viscosity, Froude number approaches the known limit of 0.35. They propose an equation to predict Froude number in the range: $4.8 < \mathrm{Eo} < 228$; $1 < \mathrm{N_f} < 14700$; $10^{-12} < \mathrm{M} < 10^{4}$; $\mu^* < 70$; $0.002 < \mathrm{Re} < 4960$. This equation features an important difference to the previous ones: it takes into account the influence of the dispersed phase viscosity by including μ^*. For that equation, Hayashi et al. (2011) assumed that the terminal velocity is independent of the drop length when $d_S/D < 1.6$. Furthermore, Hayashi et al. (2011) forced the known limit of 0.35 for Froude number. They adjusted their correlation to the relation $\mathrm{Fr} = 0.01\mathrm{N_f}$ (viscous force dominant regime), as well as to experimental results from White and Beardmore (1962). They finally used simulation results to complete their correlation. That correlation was slightly changed by Kurimoto et al. (2013):

$$\mathrm{Fr} = \sqrt{\frac{A_2 \cdot A_3}{\frac{A_3}{0.35^2} + \frac{1+1.9\mu^*}{1+0.31\mu^*} A_1}}, \tag{1.9}$$

where A_1, A_2 and A_3 are defined by:

$$A_1 = \mathrm{Re}^{-1}\left(1 - 0.05\sqrt{\mathrm{Re}}\right), \tag{1.10}$$

$$A_2 = \left(1 + 3.87\,\mathrm{Eo}^{-1.68}\right)^{-18.4}, \tag{1.11}$$

$$A_3 = 0.0025\,(3 + A_2)\,. \tag{1.12}$$

Because of the presence, on both sides, of the Froude number and of the Reynolds number, the drop terminal velocity can only be obtained from equation 1.9 by an iterative process.

Kurimoto et al. (2013) also observed non-symmetrical Taylor drops under certain operating conditions.

Quan and Lou (2011) proposed a power law equation to predict Froude number, based on an axisymmetric numerical model.

$$\mathrm{Fr} = B\,{\mu^*}^{-0.27\pm0.05}, \tag{1.13}$$

where B depends on $\mathrm{N_f}$ and Eo.

1.5 Thesis objectives

The present work aimed to develop the knowledge on vertical liquid-liquid slug flow, which requires the fulfillment of the following steps:

- development and validation of a numerical model able to simulate the phenomena;
- description of the flow of an isolated Taylor drop in stagnant liquid;
- description and understanding of the role of instabilities and deviations from the axisymmetric behavior;
- description of the flow under co-current conditions and drops interaction.

In the near future, the objective is to collect the necessary data to develop a descriptive model (one-dimensional) to be applied in relevant industries, in particular in the petroleum exploitation.

1.6 Thesis layout

Following the present introductory chapter, the numerical and experimental methods are presented in Chapter 2. The results are in four chapters, each one based on a paper published or under review in scientific journals (see Table 1.1).

Table 1.1: Results chapters and corresponding publications

Chapter 3	Direito, F. J. N., Campos, J. B. L. M. and Miranda, J. M. (2016), ‘Rising of a single Taylor drop in a stagnant liquid − 2D laminar flow and axisymmetry limits’, *Physics of Fluids* **28** (5), 057101.
Chapter 4	Direito, F. J. N., Morgado, A. O., Rocha, L. A. M., Miranda, J. M. and Campos, J. B. L. M. (2017), ‘Experimental and numerical 3D study of a Taylor drop rising in a stagnant heavier liquid’, *Physics of Fluids* **29** (3), 037109.
Chapter 5	Direito, F. J. N., Campos, J. B. L. M. and Miranda, J. M. (2017), ‘A Taylor drop rising in a liquid co-current flow’, *International Journal of Multiphase Flow* **96**, 134-143.
Chapter 6	Direito, F. J. N., Campos, J. B. L. M. and Miranda, J. M. (2017), ‘Interaction between two consecutive axisymmetric Taylor drops flowing in a heavier liquid in a vertical tube’, *International Journal of Heat and Fluid Flow* **68**, 1-12.

The first results chapter deals with single axisymmetric Taylor drops rising in stagnant liquids (Chapter 3). This is the most basic formulation of liquid-liquid slug flow (Figure 1.1). The findings in this chapter are the starting point for all the other chapters. Furthermore, the chapter provides an extensive description of flow fields which enables the comparison between liquid-liquid and gas-liquid slug flow characteristics.

The second results chapter (Chapter 4) analyses isolated Taylor drops by means of a three dimensional numerical model, allowing for the assessment of the deviations from the axisymmetric behavior, thus expanding the studied range beyond the one studied in the preceding chapter. Moreover, it also analyses oscillations in the drops and their relationship to continuous phase flow oscillations in the influence region of the drop. Lab experiments were also conducted to validate the 3D model.

The complexity of the phenomena for axisymmetric drops conditions increases in the remaining two results chapters. Features are added to the flow in order to approximate the model to real slug flow (Figure 1.1). In Chapter 5, isolated drops rising in co-current flow are studied. In particular, the relationship between the drop velocity and the continuous phase velocity is assessed, as well as the influence of the drop in the continuous phase flow pattern, which is of major importance for drop interaction (see succeeding chapter).

The last results chapter (Chapter 6) deals with interaction between two axisymmetric drops in stagnant and co-current flowing continuous phase.

Finally, the thesis ends with a concluding chapter.

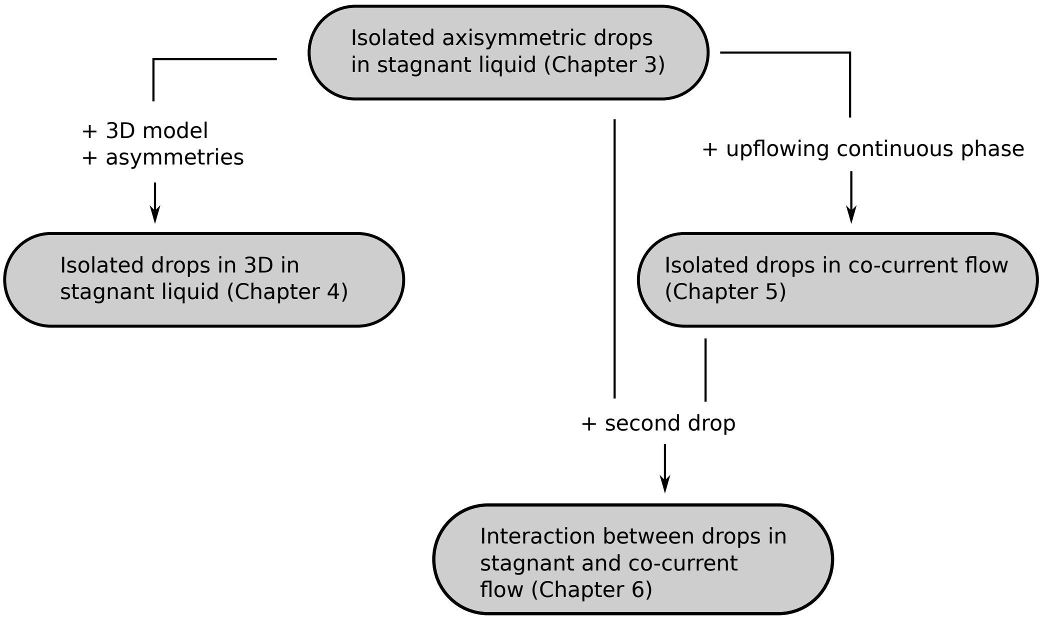

Figure 1.1: Results layout.

References

Alboudwarej, H., Felix, J., Taylor, S., Badry, R., Bremner, C., Brough, B., Skeates, C., Baker, A., Palmer, D., Pattison, K., Beshry, M., Krawchuk, P., Brown, G., Calvo, R., Triana, J. a. C., Hathcock, R., Koerner, K., Hughes, T., Kundu, D., De Cárdenas, J. L. and West, C. (2006), 'Highlighting heavy oil', *Oilfield Review* **18**(2), 34–53.

Araújo, J. D. P., Miranda, J. M. and Campos, J. B. L. M. (2013*a*), 'Flow of two consecutive Taylor bubbles through a vertical column of stagnant liquid-A CFD study about the influence of the leading bubble on the hydrodynamics of the trailing one', *Chemical Engineering Science* **97**, 16–33.

Araújo, J., Miranda, J. and Campos, J. (2013*b*), 'Simulation of slug flow systems under laminar regime: Hydrodynamics with individual and a pair of consecutive Taylor bubbles', *Journal of Petroleum Science and Engineering* **111**, 1–14.

Araújo, J., Miranda, J., Pinto, A. and Campos, J. (2012), 'Wide-ranging survey on the laminar flow of individual Taylor bubbles rising through stagnant Newtonian liquids', *International Journal of Multiphase Flow* **43**, 131–148.

Aziz, I. A. B., Brandt, I., Gunasekera, D., Hatveit, B., Havre, K., Weisz, G., Xu, Z. G., Nas, S. and Spilling, K. E. (2015), 'Multiphase Flow Simulation: Optimizing Field Productivity', *Oilfield Review* **27**(1), 26–37.

Babadagli, T. (2007), 'Development of mature oil fields A review', *Journal of Petroleum Science and Engineering* **57**(3-4), 221–246.

Bannwart, A. C., Rodriguez, O. M. H., de Carvalho, C. H. M., Wang, I. S. and Vara, R. M. O. (2004), 'Flow Patterns in Heavy Crude Oil-Water Flow', *Journal of Energy Resources Technology* **126**(3), 184.

Bannwart, A., Rodriguez, O., Trevisan, F., Vieira, F. and de Carvalho, C. (2009), 'Experimental investigation on liquidliquidgas flow: Flow patterns and pressure-gradient', *Journal of Petroleum Science and Engineering* **65**(1-2), 1–13.

Bendiksen, K. H. (1985), 'On the Motion of Long Bubbles in Vertical Tubes', *International Journal of Multiphase Flow* **11**, 797–812.

Bordeaux Rego, F., Botechia, V. and Schiozer, D. (2017), 'Heavy oil recovery by polymer flooding and hot water injection using numerical simulation', *Journal of Petroleum Science and Engineering* **153**(March), 187–196.

Brill, J. P. and Mukherjee, H. (1999), *Multiphase flow in wells*, Society of Petroleum Engineers Inc.

Brown, R. (1965), 'The Mechanics of Large Gas Bubbles in Tubes I. Bubble Velocities in Stagnant Liquids', *The Canadian Journal of Chemical Engineering* **43**(5), 217–223.

Brown, R. and Govier, G. (1961), 'High-Speed Photography in the Study of Two-Phase Flow', *The Canadian Journal of Chemical Engineering* **39**, 159–164.

Campos, J. and Carvalho, J. R. F. G. (1988), 'An experimental study of the wake of gas slugs rising in liquid', *Journal of Fluid Mechanics* **196**, 27–37.

Clark, N. J. (1969), *Elements of Petroleum Reservoirs (Henry L. Doherty series)*, revised ed edn, Society of Petroleum Engineers of AIME.

Collins, R., Moraes, F. F. D., Davidson, J. F. and Harrison, D. (1978), 'The motion of a large gas bubble rising through liquid flowing in a tube', *Journal of Fluid Mechanics* **89**(03), 497–514.

Davies, R. M. and Taylor, G. (1950), 'The Mechanics of Large Bubbles Rising through Extended Liquids and through Liquids in Tubes', *Proceedings of the Royal Society A: Mathematical, Physical and Engineering Sciences* **200**(1062), 375–390.

Dumitrescu, D. T. (1943), 'Strömung an einer Luftblase im senkrechten Rohr', *ZAMM - Zeitschrift für Angewandte Mathematik und Mechanik* **23**(3), 139–149.

Fabre, J. and Line, A. (1992), 'Modeling of 2-Phase Slug Flow', *Annual Review of Fluid Mechanics* **24**, 21–46.

Flores, J., Chen, X., Sarica, C. and Brill, J. (1999), 'Characterization of OilWater Flow Patterns in Vertical and Deviated Wells', *SPE Production & Facilities* **14**(2), 5–8.

Goldsmith, H. L. and Mason, S. G. (1962), 'The movement of single large bubbles in closed vertical tubes', *Journal of Fluid Mechanics* **14**(01), 42.

Govier, G., Sullivan, G. and Wood, R. (1961), 'The Upward Vertical Flow of Oil-Water Mixtures', *The Canadian Journal of Chemical Engineering* **39**, 67–75.

Hasan, A. and Kabir, C. (1990), 'A New Model for Two-Phase Oil/Water Flow: Production Log Interpretation and Tubular Calculations', *SPE Production Engineering* **5**(May), 193–199.

Hayashi, K., Kurimoto, R. and Tomiyama, A. (2011), 'Terminal velocity of a Taylor drop in a vertical pipe', *International Journal of Multiphase Flow* **37**(3), 241–251.

Kurimoto, R., Hayashi, K. and Tomiyama, A. (2013), 'Terminal velocities of clean and fully-contaminated drops in vertical pipes', *International Journal of Multiphase Flow* **49**, 8–23.

Kwon, H., Choi, J. I. and Seo, J. K. (2015), 'An electrical impedance monitoring method of water-lubricated oil transportation', *Flow Measurement and Instrumentation* **46**, 327–333.

Lu, X. and Prosperetti, A. (2009), 'A numerical study of taylor bubbles', *Industrial and Engineering Chemistry Research* **48**(1), 242–252.

Lyons, W. C. and Plisga, G. J. (1999), *Standard handbook of petroleum and natural gas engineering*, Elsevier.

Mandal, T., Das, G. and Das, P. (2008), 'Motion of Taylor Bubbles and Taylor Drops in Liquid-Liquid Systems', *Industrial & Engineering Chemistry Research* **47**(18), 7048–7057.

Mandal, T., Das, G. and Das, P. (2010), 'An appraisal of liquidliquid slug flow in different pipe orientations', *International Journal of Multiphase Flow* **36**(8), 661–671.

Mandal, T. K., Das, G. and Das, P. K. (2007), 'Prediction of rise velocity of a liquid Taylor bubble in a vertical tube', *Physics of Fluids* **19**(12), 128109.

Mandal, T. K., Das, G. and Das, P. K. (2009), 'Liquid Taylor Bubbles Rising in a Vertical Column of a Heavier Liquid: An Approximate Analysis', *Journal of Fluids Engineering* **131**(1), 011303.

Morgado, A., Miranda, J., Araújo, J. and Campos, J. B. (2016), 'Review on vertical gas-liquid slug flow', *International Journal of Multiphase Flow* **85**, 348–368.

Nicklin, D., Wilkes, J. and Davidson, J. (1962), 'Two-Phase Flow in Verical Tubes', *Trans. Inst. Chem. Eng* **40**.

Nogueira, S., Riethmuller, M., Campos, J. and Pinto, a. (2006), 'Flow patterns in the wake of a Taylor bubble rising through vertical columns of stagnant and flowing Newtonian liquids: An experimental study', *Chemical Engineering Science* **61**(22), 7199–7212.

Omebereiyari, N., Azzopardi, B., Lucas, D., Beyer, M. and Prasser, H. (2008), 'The characteristics of gas/liquid flow in large risers at high pressures', *International Journal of Multiphase Flow* **34**(5), 461–476.

Pietrzak, M., Płaczek, M. and Witczak, S. (2017), 'Upward flow of air-oil-water mixture in vertical pipe', *Experimental Thermal and Fluid Science* **81**, 175–186.

Pinto, A., Pinheiro, C. and Campos, J. (1998), 'Coalescence of two gas slugs rising in a co-current flowing liquid in vertical tubes', *Chemical engineering science* **53**(16), 2973–2983.

Quan, S. (2011), 'Co-current flow effects on a rising Taylor bubble', *International Journal of Multiphase Flow* **37**(8), 888–897.

Quan, S. and Lou, J. (2011), 'Viscosity-ratio-based scaling for the rise velocity of a Taylor drop in a vertical tube', *Physical Review E* **84**(3), 1–6.

Ray, B. and Prosperetti, A. (2014), 'On skirted drops in an immiscible liquid', *Chemical Engineering Science* **108**, 213–222.

Serapião, A. B. S. and Bannwart, A. C. (2013), 'Knowledge Discovery for Classification of Three-Phase Vertical Flow Patterns of Heavy Oil from Pressure Drop and Flow Rate Data', *Journal of Petroleum Engineering* **2013**.

Seyfried, R. and Freundt, A. (2000), 'Experiments on conduit flow and eruption behavior of basaltic volcanic eruptions', *Journal of Geophysical Research* **105**(B10), 23727.

Sheng, J. J., Leonhardt, B. and Azri, N. (2015), 'Status of polymer-flooding technology', *Journal of Canadian Petroleum Technology* **54**(2), 116–126.

Spedding, P., Donnelly, G. and Cole, J. (2005), 'Three Phase Oil-Water-Gas Horizontal Co-Current Flow I. Experimental and Regime Map', *Chemical Engineering Research and Design* **83**(4), 401–411.

Spedding, P., Woods, G., Raghunathan, R. and Watterson, J. (2000), 'Flow Pattern, Holdup and Pressure Drop in Vertical and Near Vertical Two-and Three-Phase Upflow', *Chemical Engineering Research and Design* **78**(3), 404–418.

Thomas, S. (2008), 'Enhanced oil recovery: An overview', *Oil & Gas Science and Technology* **63**(1), 9–19.

Verweij, J. M. (1993), *Hydrocarbon migration systems analysis*, Elsevier.

Viana, F., Pardo, R., Yánez, R., Trallero, J. L. and Joseph, D. D. (2003), 'Universal correlation for the rise velocity of long gas bubbles in round pipes', *Journal of Fluid Mechanics* **494**, 379–398.

White, E. and Beardmore, R. (1962), ‘The velocity of rise of single cylindrical air bubbles through liquids contained in vertical tubes’, *Chemical Engineering Science* **17**(5), 351–361.

Woods, G., Spedding, P., Watterson, J. and Raghunathan, R. (1998), ‘Three-phase oil/water/air vertical flow’, *Chemical Engineering Research and Design* **76**(5), 571–584.

Yang, Q., Han, Y., Liu, W., Zhang, H., Ren, Y. and Jin, N. (2017), ‘Investigation on the effect of polymer in vertical oil-water two-phase flow using nonlinear analysis’, *Experimental Thermal and Fluid Science* **80**, 1–18.

Zukoski, E. E. (1966), ‘Influence of viscosity, surface tension, and inclination angle on motion of long bubbles in closed tubes’, *Journal of Fluid Mechanics* **25**(04), 821.

2

Methods

2.1 Introduction

This work takes advantage of the powerful tools provided by Computational Fluid Dynamics (CFD). The present chapter contains a first section where a brief introduction to CFD is presented. Following this section, a new one provides the details regarding the numerical model used.

To validate CFD results, some laboratory experiments were performed. The last section, in this chapter, presents the techniques employed.

2.2 Computational Fluid Dynamics

Computational continuum mechanics comprises the simulation of continua using computational methods to implement physical laws. In particular, Computational Fluid Dynamics (CFD) is the application of a numerical code to simulate fluid flow and interrelated phenomena, such as heat and mass transfer or/and chemical reaction (Date, 2005).

Applications of CFD can be found in several areas such as: aerodynamics, ship building and navigation, power plants, turbomachinery, chemical processes, building ventilation, oceanography and biomedical applications.

CFD has several advantages when compared to lab experiments. It allows for easy and quick step-up changes, as well as scaling up or down. Furthermore, CFD is able to simulate operating conditions or materials behaviour that are difficult or dangerous to deal with. Another advantage of CFD concerns the detailed information on fluid flow field and other related parameters (Versteeg and Malalasekera, 1995).

CFD is based on the implementation of computer codes that represent physical laws (Date, 2005). Due to the nonlinearity of most of the equations involved in CFD studies and to the non-uniformity of the domain, the problems can only be solved employing space and time discretization of the conservative equations (Weller and Tabor, 1998). Therefore, differential equations and other nonlinear equations are substituted by algebraic equations, which are "understood" and solved by the computer. The most common techniques are: finite- differences, finite-elements and finite-volumes. The finite-elements subdivide the problem into smaller parts in pre-determined locations and the residual of the whole algebraic system are minimized (Versteeg and Malalasekera, 1995). The finite-differences approximate the equations by means of finite differences between the values in two or more nodes of the mesh. In the finite-volumes, the domain is divided into a set of discrete small volumes (or elements, or cells). The model equations are volume-integrated over each one of those small volumes (Versteeg and Malalasekera, 1995). The finite-volumes method (Figure 2.1) will be used along all the present work.

In order to solve this set of equations that define the problem, an iterative method is usually used, and a criteria is defined to choose the moment to finish the iterative procedure (Wesseling, 2010). Three kinds of numerical errors are inherent to a CFD simulation: discretization, convergence and rounding (Wesseling, 2010). The latter is due to the limits of computer memory. Discretization errors arise due to the truncation of linearized equations. The convergence error has to do with the convergence to the correct solution of the iterative procedure used to solve the set of algebraic equations.

2.2.1 The parts of a CFD model

The most important elements of a CFD simulation are: the computational domain and its mesh, the discretized equations that model the physical problem and the numerical methods to solve the algebraic equations. Because of the finitude of the domain, special mathematical conditions are imposed at the

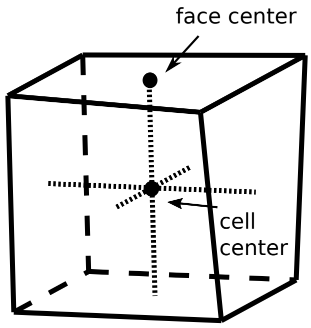

Figure 2.1: A cell in finite-volume method.

boundaries: the so called boundary conditions. Furthermore, initialization values as well as fluid physical properties are also required.

The domain and the mesh

The assembly of the numerical model starts by defining the domain, i.e., the geometry necessary to the simulation. This can be as diverse as a simple tube (a cylinder), a ship, or the intricate system of small tubes involved in injection molding. From the geometry, one can then construct a grid, or mesh, to indicate the code where must perform the relevant computations. For the finite-volumes method, the result of such step is a a structure of contiguous cells (2D or 3D). The number of cells is obviously finite and so a fundamental issue deals with the amount of cells of a grid. Generally, the larger the number (better mesh refinement), the more accurate the solution will be. Besides, increasing accuracy by providing a finer discretization, the mesh will describe curved or irregular surfaces better. For instance, with a finite number of nodes, one cannot create a "perfect" sphere, but, the more refined the mesh is, the better will be the approximation. However, as the mesh elements constitute computation locations, increasing the number of elements, it increases the number of computations steps and, therefore, the computational resources required. Such increase has consequences at three levels: computer memory, data storage due to the amount of information and time required to perform a simulation due to the increased number of numerical procedures. Moreover, consider the Courant number (a dimensionless number which is a consequence of the Courant-Friedrichs-Lewy condition) (Anderson, 1995),

$$\mathrm{Co} = u_x \frac{\Delta t}{\Delta x} \leq \mathrm{Co}_{\mathrm{max}}, \tag{2.1}$$

which, in a transient simulation, usually have a maximum value in order to assure a better solution and the stability of the simulation. Hence, the increase in the number of cells implies smaller time-steps, causing a transient simulation to be even slower. Furthermore, post-processing also gets harder. Therefore, while simple simulations can be performed on a small laptop, simulations with several millions of elements generally run on workstations or computer clusters. Because of the balance between accuracy and computational resources available, meshes are sometimes constructed with non-uniform levels of refinement: finer where large variations of the variables in study occur and coarser in the other locations. One of the most common techniques to deal with the computations effort concerns reducing the problem to a simpler geometry, for example, a two dimensional geometry, or the insertion of symmetry conditions. As it is not always possible to do so, the better mesh configuration is decided by comparing the simulation results to experimental data or theoretical solutions, the so called validation procedure.

Another detail about meshes concerns how the nodes location is defined. In some cases the location can be defined by equations – structured grids, while in others, every location must be explicitly defined – unstructured grids. There are solvers (the iterative procedure to solve the pressure-velocity coupled equations – see Section 2.2.1) created to define structured grids (which are more efficient regarding computational resources), however, unstructured grids, have been gaining space. In the most complex geometries, a structured grid can be almost impossible to employ (Versteeg and Malalasekera, 1995).

Discretization techniques and solvers

The finite volumes method can be summarized as a technique that approximates the derivatives of a certain variable in a cell by means of polynomial differences (usually linear or quadratic) stated in the neighboring of each cell.

Three main steps occur in a finite volumes method (Versteeg and Malalasekera, 1995): the first is the integration of the governing equations over all the mesh elements; the second consists in the transformation of the integral equations into algebraic equations by means of finite differences approximations; the last step consists in solving the equations by an iterative method. In the finite volumes method, the conservation of a property ϕ is, therefore (Versteeg and Malalasekera, 1995):

$$\dot{\phi}_{\mathrm{CV}} = \phi_{\mathrm{convectionin}} + \phi_{\mathrm{diffusionin}} + \phi_{createdCV}. \tag{2.2}$$

This equation indicates that, the rate of change of a property equals the net flux into the control volume (due to convection and diffusion) plus the net rate of creation or consumption of the property inside the control volume.

In CFD, the fluids are treated as a continuum and thus, the unknown variables are density, temperature, velocity and pressure (Versteeg and Malalasekera, 1995). Velocity is usually obtained from the momentum equations. Liquids and gases flowing at low speeds can be regarded as incompressible (Versteeg and Malalasekera, 1995). Because of that, there is no interrelation between the energy equation and the momentum and mass conservation equations. Therefore, if the problem does not involve heat transfer, the energy equation is not included in the CFD model. For incompressible flows, the solvers are usually pressure-based. Pressure-based solvers usually manipulate continuity and momentum equations to obtain the pressure field. On the other hand, in density-based solvers (employed usually for compressible flows), the continuity equation is used to obtain the density field, while the pressure field results are from the equation of state. In this work, the model is pressure based. Due to the nonlinearity and coupling of the equations an iterative process is required.

The iterative process for solving the pressure-velocity coupling can be segregated or coupled. In a coupled solver, the set of governing equations are solved in simultaneous. On the other hand, a segregated algorithm solves the governing equations sequentially. This strategy is memory-efficient but the convergence might be harder (Ansys Fluent, 2011). In the present work, the algorithm is segregated. Its workflow can be summarized in few steps (Ansys Fluent, 2011) (Figure 2.2). It starts by updating the properties. Next, velocity field is computed. Then, a pressure-correction (when it is needed) is done and continuity equations are solved. Afterwards, pressure and velocity fields are updated. Finally, equations such as energy, turbulence and others are solved. After all these steps, convergence is checked. If the criteria are not met, the previous steps must be repeated.

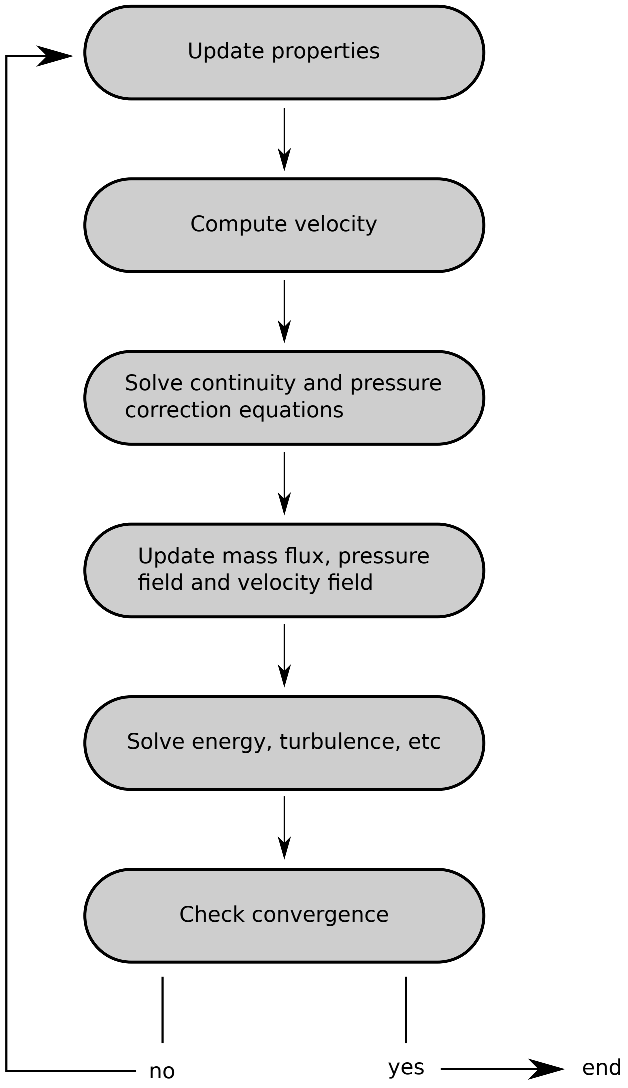

Figure 2.2: Segregated algorithm steps.

Boundary conditions

The determination of the flow characteristics on a cell is dependent on the fluxes between the cell and its neighbors. A special set of cells are those lying on the boundaries of the domain (such as walls or inlets and outlets). It is, therefore, required a special mathematical treatment for such locations.

Typical inlet boundary condition might concern the definition of the flow profile. For example, if a fully developed laminar flow enters a rectangular domain in a direction x orthogonal to y, then the velocity profile might be described by:

$$u(y) = y_{x=0}\left(1 - y^2/l^2\right). \tag{2.3}$$

Another common inlet and outlet boundary condition consists in setting that a field ϕ attains a fully developed state, and so the derivative of that specific property is null alongside the flow direction at the boundary in consideration. As such, if n is the coordinate orthogonal to the boundary:

$$\frac{\partial \phi}{\partial n} = 0. \tag{2.4}$$

This condition of normal zero gradient is most of the times used as wall boundary condition (Anderson, 1995).

Concerning the velocity on the wall of a solid surface, the most common condition is the no-slip condition, which specifies that the fluid velocity in the wall matches the velocity of the wall itself (in magnitude and direction).

The pressure field is solved in terms of relative pressure and a reference pressure value and location is normally set (Patankar, 1980). In problems consisting of inlet and outlet of the control volume, it is common to set the pressure at one side, and the velocity at the other side (Versteeg and Malalasekera, 1995).

Simulation post-processing

The post-processing of a CFD simulation is required in order to interpret the results and analyze the flow parameters. The most recent post-processing tools allow for complex data manipulation and image generation. Depending on the field, it might be of interest to present concentration, velocity, pressure, shear stress or simply the viscosity field. One can observe 3D effects or observe planes and cuts.

Some of the most common results concern the representation of the velocity field as arrows (vectors) (Figure 2.3). Such representation is useful because it provides information on both direction and magnitude of the velocity. The introduction of a color to the arrows can add further information to the representation.

Concerning the velocity field, one can draw also streamlines (Figure 2.3), which are curves tangent to the velocity vectors that provide an instantaneous path of the elements of fluids. With streamlines, one can analyze which regions have higher flow rates or those where there are dead volumes or recirculations. Concerning particle tracking, streaklines and pathlines can be used. Unlike streamlines which, as said, are instantaneous, and thus, correspond to a snapshot of the flow field, streaklines and pathlines depend on the flow history (time). Streaklines correspond to the path that fluid particles with the same origin have undergone. This is analogous to inject a dye in a fixed point and observe the path or several paths the dye undergoes. A pathline correspond to follow a fluid particle along the time. It is equivalent of following a fluid particle by analyzing the streamlines in every moment. Therefore, on steady flows, pathlines and streamlines are coincident. Moreover, because there is no reason, in steady flow, for two

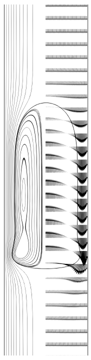

Figure 2.3: Streamlines (left) and velocity vectors (right).

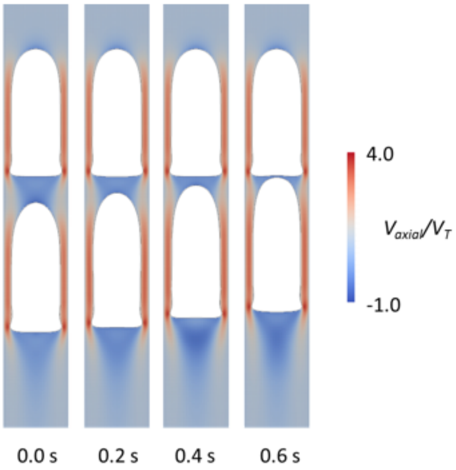

Figure 2.4: Example of colored contours (for the normalized axial velocity component).

particles coming from the same location to follow different paths, the streaklines are also coincident with the pathlines and streamlines. An important characteristic of the streamlines is that they are dependent on the reference frame, as they depend on the velocity field.

For scalars, the representation of colored contours (Figure 2.4), usually provides a fast way of data analyses. Scalar values along a line are also common, as well as their representation as a function of time.

2.3 Numerical model

In the present work, the rise of Taylor drops in another liquid in vertical tubes was simulated. The present section discusses some details regarding the numerical model used.

The simulations were run using the software package Ansys Fluent, versions 14, 15 and 16 (no differences between them concerning the physical phenomena in study). After the domain and grid are created, a field initialization was performed, which includes the establishment of the drop flow. The Ansys Fluent implementation of the Volume of Fluid method (VOF) was used with a pressure-based solver. In the model, there is not any imposition of temperature, heat transfer, mass transfer or reaction. The flow is laminar and the fluids are incompressible and immiscible.

Even though the goal is to find a steady-like state concerning the drop and the flowing continuous phase, the simulations were run in transient conditions. Transient conditions were used because the

Table 2.1: Summary of numerical method options.

time discretization	first order implicit	section 2.3.1, Discretization and other algorithms
pressure-velocity coupling	PISO	section 2.3.1, The VOF solver and interface reconstruction
volume fraction and interface	geometric reconstruction	section 2.3.1, The VOF solver and interface reconstruction
scalar gradients	Green-Gauss node based	section 2.3.1, Discretization and other algorithms
pressure	pressure staggering option	section 2.3.1, Discretization and other algorithms
momentum	QUICK	section 2.3.1, Discretization and other algorithms

numerical procedure initiates with a drop with a virtual shape (as explained further in the text) and also, in some conditions, the drop oscillates, even when the terminal velocity is reached.

For some conditions, a two dimensional model (2D) symmetric in respect to the tube axis (axisymmetry) was used. In comparison to the three dimensional model (3D), this provides a much lower weight simulation. However, it was found that, for some conditions, a 3D model was required. The first subsection of the numerical model presentation, concerns the 2D axisymmetric model (Figure 2.5). Afterwards, the 3D model is presented by pointing out the differences to the 2D model.

2D and 3D numerical models follow the validated gas-liquid models already in usage in the research group (Araújo et al., 2012, 2013, 2015). Table 2.1 summarizes the solvers and methods used in this work.

2.3.1 The two dimensional axisymmetric model

The axisymmetric 2D model considers that there is symmetry in the flow. In order to understand the concept suppose that, in the tube, several longitudinal wall to center cuts are done (similar to slicing a cake – Figure 2.6). When the velocity and scalar fields are the same in all the slices (rectangular shape), then it is axisymmetric. On such occasions, there is no need to simulate the whole tube, but just one of the slices. This provides an efficient route for the simulations. In the axisymmetric model, the flow has only axial (in this work vertical) and radial directions (Lewis et al., 2004). At the axis, the symmetry condition imposes for any field ϕ:

$$\frac{\partial \phi}{\partial r} = 0. \tag{2.5}$$

The model validation is discussed in Chapter 3.

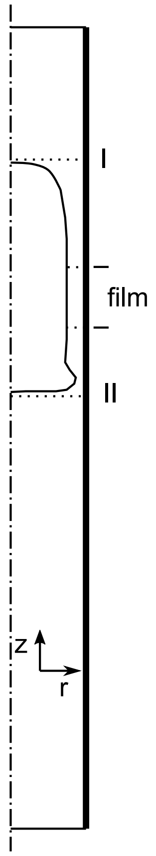

Figure 2.5: Axisymmetric domain with drop.

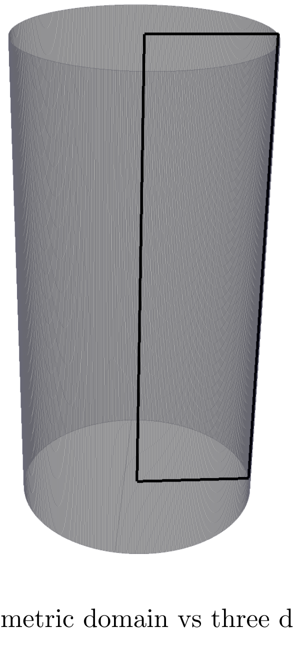

Figure 2.6: Axisymmetric domain vs three dimensional domain.

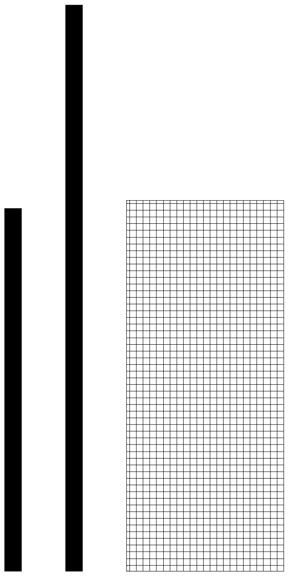

Figure 2.7: Mesh 52 × 1144, mesh 52 × 1720 and zoomed in detail of mesh.

Domain and mesh

Axial symmetry (around the cylinder axis) was used to minimize computational effort. The domain consisted of a rectangle with a width $D/2$ and $11D$ long ($16.5D$ for two drop cases). The domain needs to be long enough to ensure a continuous undisturbed phase at the entrance and at the exit. The mesh consisted of a 52 × 1144 (52 × 1720 for two drop cases) grid of quadrilateral and uniformly distributed cells. The number of cells in the film flow region between the drop and the wall had between 10 and 15 cells. A finer grid (7.8 times more cells) was also used in preliminary tests, but showed identical results and it was dropped due to computation time.

For coalescence (Chapter 6), a longer domain was used. In order to keep the same refinement, the number of elements in the axis direction was increased from 1144 to 1720. The meshes used are shown in Figure 2.7.

Governing equations

The conservation of momentum is modeled by the incompressible Navier-Stokes equation:

$$\frac{\partial\left(\rho_a \vec{v}\right)}{\partial t} + \nabla \cdot \left(\rho_a \vec{v}\vec{v}\right) = -\nabla p + \rho_a \vec{g} + \nabla \cdot \mu_a \left(\nabla \vec{v} + \left(\nabla \vec{v}\right)^T\right) + \vec{f_\sigma}, \tag{2.6}$$

where p is the pressure, ρ_a the density, v the velocity and μ_a the viscosity. It contains four force terms: pressure, gravity, viscosity and interfacial tension ($\vec{f_\sigma}$). The interfacial tension determines the relationship between the pressure difference in the two sides of the interface and the local curvature:

$$\Delta p = \sigma \left(\frac{1}{R_1} + \frac{1}{R_2}\right), \tag{2.7}$$

where R_1 and R_2 are the curvature radii.

The continuity equation (Munson et al., 2005; Campos, 2013) states:

$$\frac{\partial \rho_a}{\partial t} + \nabla \cdot \left(\rho_a \vec{v}\right) = 0. \tag{2.8}$$

For axisymmetric flow, no flow normal to the zr-plane exists and the scalar momentum equations can be written as (Feng et al., 2016):

$$\begin{aligned}\frac{\partial \rho_a v_r}{\partial t} + \frac{1}{r}\frac{\partial r \rho_a v_r^2}{\partial r} + \frac{\partial \rho_a v_r v_z}{\partial z} = &- \frac{\partial p}{\partial r} + 2\left(\frac{\partial}{\partial r}\left(\mu_a \frac{\partial v_r}{\partial r}\right) + \frac{\partial}{\partial r}\left(\mu_a \frac{v_r}{r}\right)\right) \\ &+ \frac{\partial}{\partial z}\left(\mu_a\left(\frac{\partial v_z}{\partial r} + \frac{\partial v_r}{\partial z}\right)\right) + f_{\sigma,r},\end{aligned} \tag{2.9}$$

where $f_{\sigma,r}$ is the radial component of the surface tension force term, and

$$\begin{aligned}\frac{\partial \rho_a v_z}{\partial t} + \frac{1}{r}\frac{\partial r \rho_a v_r v_z}{\partial r} + \frac{\partial \rho_a v_z^2}{\partial z} = &- \frac{\partial p}{\partial z} + \frac{1}{r}\frac{\partial}{\partial r}\left(\mu_a r\left(\frac{\partial v_z}{\partial r} + \frac{\partial v_r}{\partial z}\right)\right) \\ &+ 2\frac{\partial}{\partial z}\left(\mu_a \frac{\partial v_z}{\partial z}\right) - \rho_a g + f_{\sigma,z},\end{aligned} \tag{2.10}$$

where $f_{\sigma,z}$ is the axial component of the surface tension term.

The VOF solver and interface reconstruction

The Volume of Fluid method (VOF) was conceived to treat free surfaces in incompressible problems by solving the momentum equations and tracking the volume fraction of each species in all the domain (Hirt and Nichols, 1981).

In order to deal with the two-phase flow through VOF, a variable α_i is defined to track the position of the interface, in this work liquid-liquid interface. The value of α_i is 1 at any point occupied exclusively by the fluid i, 0 if no i exists there, or a number between 0 and 1, if both fluids exist in the same mesh volume. Notice that a number between 0 and 1 does not mean that the two liquids are mixed (immiscible materials). In any cell:

$$\alpha_{\mathrm{C}} + \alpha_{\mathrm{D}} = 1, \tag{2.11}$$

where "C" stands for continuous phase and "D" for dispersed phase.

The tracking of the interface is done by solving the continuity equation for the dispersed phase (Hirt and Nichols, 1981):

$$\frac{\partial}{\partial t}\left(\alpha_{\mathrm{D}}\right) + \nabla \cdot \left(\alpha_{\mathrm{D}} \vec{v}\right) = 0. \tag{2.12}$$

In the present work, an explicit scheme was used for solving the VOF method. The advantage of the explicit scheme over the implicit one relies on the fact that the latter requires the values in the current time step for the volume fraction values, thus requiring an iterative process. The VOF explicit scheme is based on the following equation:

$$\frac{\alpha_{\mathrm{D}}^{n+1}\rho_{\mathrm{D}}^{n+1} - \alpha_{\mathrm{D}}^{n}\rho_{\mathrm{D}}^{n}}{\Delta t} V_{\mathrm{cell}} + \sum_f \left(\rho_{\mathrm{D}} u_f^n \alpha_{\mathrm{D},f}^n\right) = 0, \tag{2.13}$$

where "n" and "n+1" refer to two consecutive time steps (Δt), and f to the property in the cell face. V_{cell} is the cell volume.

Volume fraction phase values are, in the present work, computed using a geometric reconstruction scheme (Youngs, 1982), explained in detail below.

In order to compute the face fluxes (in interface regions), several schemes are available. In the present work, preliminary tests (following strategies like the ones in Deshpande et al. (2012); Hoang et al. (2013); Magnini et al. (2016)) were conducted to choose the best one. An overview on the options is now provided.

Ansys Fluent has implemented a non-linear combination of upwind and downwind differencing schemes and also a second order reconstruction method based on a slope limiter. It also provides a scheme based on the method proposed by Ubbink (1997) (CICSAM in Ansys Fluent).

The previous methods showed poor results in the preliminary tests. Furthermore, upwind schemes are unsuitable for computing the interface due to the diffusive nature (Ansys Fluent, 2011). Therefore, the chosen method was the geometric reconstruction (Youngs, 1982). This scheme represents the interface between two fluids using a piecewise-linear approach. It is accurate but also time-consuming. The method starts by computing a slope for an interface within the cell, based on the volume fraction of the phases. Afterwards, it computes the fluid transport by advection through each face by using the created linear interface and the face velocity components. Finally, it determines the new cell volume fraction balancing the advection fluxes.

Discretization and other algorithms

Temporal discretization is required for transient simulations. First order implicit time integration was used in this work to perform the time discretization of the velocity and scalar fields. Let function $F(\phi)$ represent any spatial discretization. If "n" and "n+1" represent two consecutive steps, the following equation must converge each time-step:

$$\frac{\phi^{n+1}-\phi^{n}}{\delta t}=F\left(\phi^{n+1}\right). \tag{2.14}$$

For spatial discretization, Fluent implements an "upwind" scheme, which stores the scalar values at the cell centers and interpolates the values at the cell faces, taking into account the direction of the normal velocity. The first order upwind scheme assumes that cell center values are representative of the whole cell. Therefore, the face value is equal to the cell center value in the upstream cell. In the second order upwind scheme, the face value is computed taking into consideration the cell center and the face center, as well as the gradient and the scalar value in the upstream cell (Ansys Fluent, 2011). Fluent also provides a power-law scheme. This consists in the interpolation of the face value using a one-dimensional convection-diffusion equation. A third order method is also provided by Ansys Fluent. The third order MUSCL Scheme mixes a central differencing scheme and a second order upwind scheme. The QUICK (Leonard, 1979) scheme consists on a weighted average of second order upwind scheme and central interpolations of the variable in study:

$$\phi_f=\theta(\text{central second order})+(1-\theta)\,(\text{second order upwind}), \tag{2.15}$$

Traditionally, θ is set to a fixed value of 1/8 (Leonard, 1979). However, Ansys Fluent employs a different strategy, and uses a non-constant θ.

In the present work, the momentum equation is solved with the QUICK scheme, due to its accuracy (Versteeg and Malalasekera, 1995; Ansys Fluent, 2011; Araújo et al., 2013). Undershoots and overshoots that can arise in QUICK scheme (Versteeg and Malalasekera, 1995) are dealt by the variable θ (Ansys Fluent, 2011). The diffusion terms are computed by second-order central-differences.

Regarding gradients, Green-Gauss theorem is used to compute scalar gradients at the cell center as well as velocity derivatives. Let ϕ be any scalar, then, at the cell center:

$$\nabla\phi = \frac{1}{V_{\text{cell}}}\sum_{f}\bar{\phi_f}\bar{A_f}. \tag{2.16}$$

One of the options to evaluate the average scalar values in the face ($\bar{\phi_f}$) is the arithmetic average of the values in the neighboring cells (cell centers) – cell-based.

A more accurate method was, though, used in this work – the Green-Gauss node-based model. The Green-Gauss node-based model (Figure 2.8) determines $\bar{\phi_f}$ by computing the arithmetic average of the node values ($\bar{\phi_n}$) delimiting a face:

$$\bar{\phi_f} = \frac{1}{\text{number of nodes}}\sum_{\text{nodes}}\bar{\phi_n}. \tag{2.17}$$

In order to compute the values at the nodes ($\bar{\phi_n}$), weighted averages of the cell center values surrounding each node are computed (Figure 2.8). Ansys Fluent solves a constrained minimization problem, computing exact values of a linear function at a node from the neighboring cells center values (Ansys Fluent, 2011). With this scheme, second-order spatial accuracy is preserved.

Concerning the pressure, the chosen scheme was PRESTO! (Ansys Fluent, 2011). This scheme is analogous to the staggered grid schemes (Patankar, 1980).

For the pressure-velocity coupling, Ansys Fluent provides a coupled algorithm, as well as segregated algorithms (SIMPLE, SIMPLEC and PISO) – refer to Figure 2.2 for a summary on the segregated algotithms. SIMPLE and SIMPLEC enforce mass conservation by relating velocity and pressure (Ansys Fluent, 2011). An iterative process starts by creating initial guesses for velocity and pressure fields. Firstly, the guessed pressure field is used to solve the momentum equation. Afterwards, the continuity equation is used to compute a pressure correction which is then used to update velocity and pressure fields (Versteeg and Malalasekera, 1995). In the process, the face fluxes are progressively guessed and corrected (Ansys Fluent, 2011; Versteeg and Malalasekera, 1995).

PISO scheme (Issa, 1986) (which stands for Pressure-Implicit with Splitting of Operators) can be regarded as an improvement of the SIMPLE and SIMPLEC algorithms (Ansys Fluent, 2011). One of the problems of these algorithms lies in the fact that, after pressure correction, the velocities and fluxes do not satisfy momentum equation. Therefore, the calculation procedure must be repeated until the momentum balance closes (Ansys Fluent, 2011). PISO moves the repeated calculations to the pressure-correction step – momentum correction.

Ansys Fluent also provides an option to include a body forces corrector (“implicit body forces”) for segregated algorithms. It acts by taking into account the partial equilibrium between pressure gradient and body forces (Ansys Fluent, 2011). Because the solution becomes more robust and convergence is faster, all simulations in this work were run with this option.

Interfacial forces are modeled by the Continuum Surface Force method (Brackbill et al., 1992). This method creates the interface between both liquids as a transition region of finite thickness, where the surface tension force is proportional to the curvature at each location. The surface tension term, $\vec{f_\sigma}$, in momentum equation is:

$$\vec{f_\sigma} = \sigma\kappa\frac{\rho_a\nabla\alpha_{\text{D}}}{0.5\left(\rho_C + \rho_{\text{D}}\right)}. \tag{2.18}$$

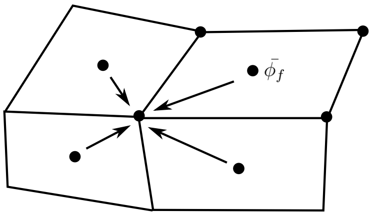

Figure 2.8: Green-Gauss node based representation.

The κ refers to the curvature of the interface and is computed by:

$$\kappa = -\nabla \cdot \frac{\nabla \alpha_{\mathrm{D}}}{|\vec{\nabla} \alpha_{\mathrm{D}}|}. \tag{2.19}$$

Notice that for cells that do not contain interface, Equation 2.19 yields $\kappa = 0$, so $\vec{f_\sigma} = \vec{0}$, the surface tension term in Equation 2.6 falls. This model (such as the alternative Continuum Surface Stress) might introduce parasitic currents in the interface calculation caused by the imbalance between pressure and surface tension forces (Ansys Fluent, 2011).

Boundary conditions and fluids properties

An important design option must be now introduced: a reference frame attached to the drop nose. This reference frame determines that the tube wall moves downward at an imposed speed, the drop speed. Therefore, the drop is always inside the domain and the no-slip condition is assumed in the wall. This strategy avoids the need of a very long domain (Figure 2.9).

The reference frame attached to the nose means that the continuous phase velocity is affected in the simulation. The top of the tube is an inlet of the domain and the bottom an outlet. Regarding the outlet, a pressure-outlet (Ansys Fluent name) boundary condition must be used. This means that the pressure must be imposed on this location.

The inlet flow boundary condition depends on the case being modeled. In the present work, two cases were studied: a stagnant continuous phase and a rising continuous phase (laminar flow). Because of the reference frame, for the inlet, a uniform downward velocity (equal in magnitude to the drop terminal velocity and wall speed) was imposed for the stagnant continuous phase. For the laminar flow case the drop terminal velocity must be subtracted from the parabolic profile. Hence:

$$u(r) = -V_{\mathrm{TC}} + 2\,U_{\mathrm{C}} \left(1 - (2r/D)^2\right). \tag{2.20}$$

The boundary condition in the tube axis was already discussed above when presenting the axisymmetric concept.

Convergence and other simulation parameters

In certain locations of the domain, both fluids might be present, $\alpha_{\mathrm{D}} \neq 0 \wedge \alpha_{\mathrm{D}} \neq 1$. This does not represent mixture, but the interface between the liquids.

This interface is not abrupt. Instead, a small numerical dispersion of the volume fraction occurs (refer to the Continuum Surface Force method in 2.3.1). In this work, it is assumed that the interface is represented by $\alpha = 0.5$. Ansys Fluent computes the momentum equation in these elements supposing

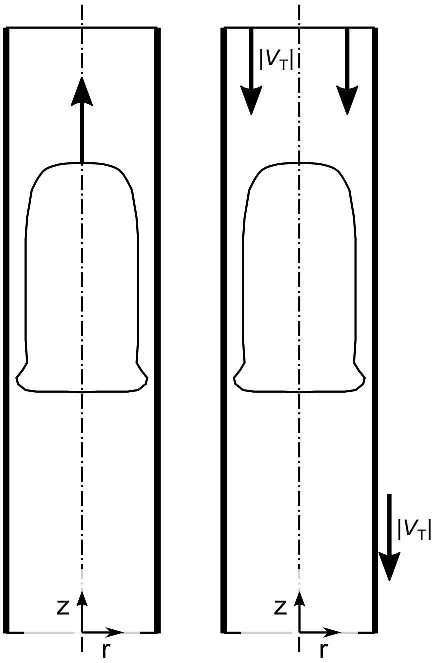

Figure 2.9: Earth reference frame (left) and reference frame attached to the drop nose (right).

linear contributions of each phase for the density and viscosity:

$$\rho_\mathrm{a} = \alpha_\mathrm{C}\rho_\mathrm{C} + \alpha_\mathrm{D}\rho_\mathrm{D}, \tag{2.21}$$

$$\mu_\mathrm{a} = \alpha_\mathrm{C}\mu_\mathrm{C} + \alpha_\mathrm{D}\mu_\mathrm{D}. \tag{2.22}$$

Some authors suggest, instead, the usage of the harmonic mean (Carlson et al., 2008; Quan, 2011; Tuković and Jasak, 2012) to correct the continuity of viscous stresses (Patankar, 1980; Gunsing, 2004; Hayashi et al., 2011):

$$\frac{1}{\mu_\mathrm{a}} = \frac{\alpha_\mathrm{C}}{\mu_\mathrm{C}} + \frac{\alpha_\mathrm{D}}{\mu_\mathrm{D}}. \tag{2.23}$$

Such suggestion was employed in preliminary simulations, but the results showed no significant differences. Due to the increased time computation, this strategy was dropped.

Concerning the time-step size, a maximum Courant number of 0.25 was imposed. This value is found in several drop-like multiphase studies (Gerlach et al., 2006; Taha and Cui, 2006; Magnini et al., 2016). Furthermore, the Courant number of 0.25 had yielded good results in previous works within the research group (Araújo et al., 2012, 2013).

In Ansys Fluent, continuity and velocity equations are treated differently when computing the residuals needed to assure convergence (Ansys Fluent, 2011). For the continuity equation, Ansys Fluent sums the rate of mass creation in each cell. The largest value in the first five iterations is stored. The continuity residual at each iteration is then computed by the ratio between the sum of the mass creation in each cell and the stored value.

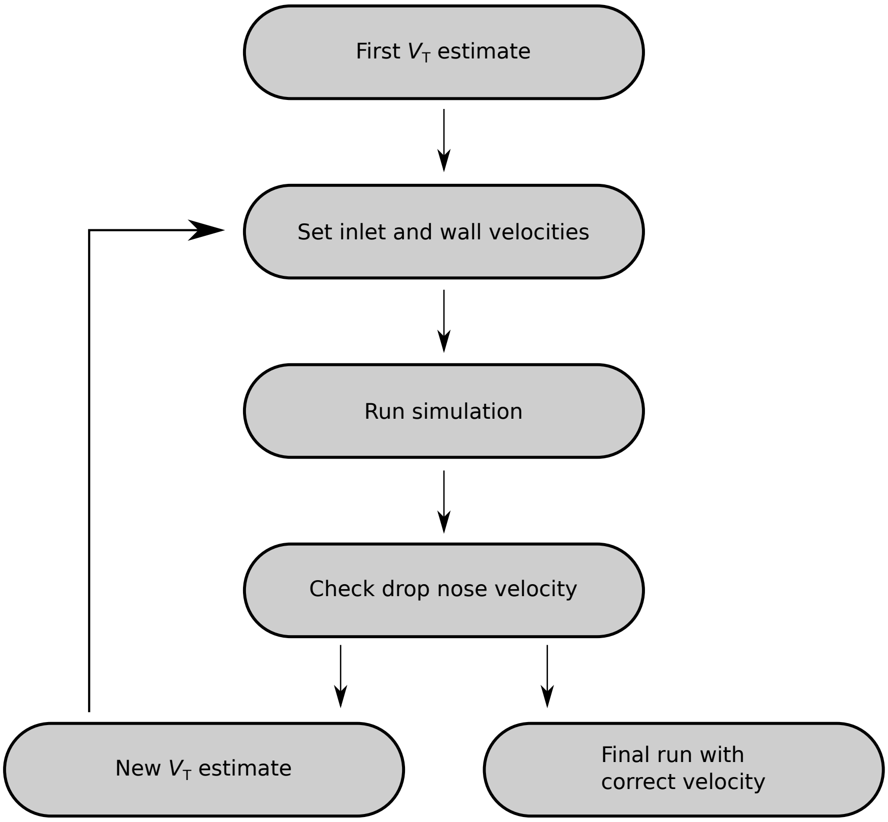

Figure 2.10: Procedure for finding drop velocity.

The velocity residuals for the x-direction are given by:

$$\text{residuals} = \frac{\sum\limits_{\text{cells}} |\sum\limits_{\text{nb}} (a_{\text{nb}} v_{x,\text{nb}} + b + a_{\text{p}} v_{x,\text{nb}})|}{\sum\limits_{\text{cells}} |\, a_p \,||\vec{v}||\,|}, \tag{2.24}$$

where the coefficients a refer to the center coefficients “p” and “nb” of the neighbouring cells (Versteeg and Malalasekera, 1995). The term b is related to sources and boundary conditions (Ansys Fluent, 2011). The other directions are computed in a similar fashion.

The convergence criteria for the iterative computation of the continuity and velocity equations were set to 10^{-6} (see Equation 2.24). For each time-step a limit of 1000 iterations was imposed. Nevertheless, this limit was never reached, which ensures that convergence criteria were met in every time-step.

The final result for each flow condition is obtained by an iterative method (Figure 2.10). Firstly, inlet and wall velocities are imposed based on literature correlations, and a first simulation runs. After, drop velocity in the moving reference is determined and if it is higher than a given tolerance (less than 0.01), wall and inlet velocities are changed, and a new simulation is performed. This process repeats until drop velocity is less than the criterion established. Then, the correct value of the terminal velocity is found.

Solution initialization

Simulations were initialized with an isolated drop consisting of the merge of two shapes: a quarter of a circle for the drop nose region and a rectangular body, with a width matching the nose radius. Although other initialization strategies can be found in literature, this starting shape has been found to give good

Table 2.2: Comparison between the two dimensional and the three dimensional models.

Simulation algorithms	same (refer to sections 2.3.1)
Domain and mesh	different (section 2.3.1 for 2D and section 2.3.2 for 3D)
Governing equations	same but different component formulation (section 2.3.1 for 2D and section 2.3.2 for 3D)
Simulation parameters and initialization	different (section 2.3.1 for 2D and section 2.3.2 for 3D)

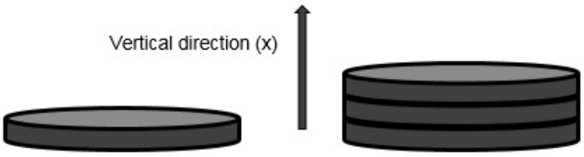

Figure 2.11: Extrusion-like method.

results (Araújo et al., 2012, 2013).

2.3.2 The three dimensional model

The three dimensional model was intended for flow conditions that do not verify the axial symmetry condition. The similarities and differences between the 2D and 3D models are summarized in Table 2.2.

Domain and mesh

The 3D model consists in simulating the tube as a cylinder (Figure 2.6). The mesh itself is three dimensional. In order to create the new grid, a pattern was firstly created in a 2D cross-section with about 3800 cells. Afterwards, in an extrusion-like effect (Figures 2.11 and 2.12), the pattern was replicated 1000 times in a length of $10D$. A denser grid was also tested but the results were identical (more on this in Chapter 4).

In this domain, the inlet and outlet are now circular.

Governing equations

The momentum equation (Equation 2.6) turns into scalar equations 2.9 and 2.10 for the axisymmetric model. In the three dimensional model, with x and y for horizontal directions and z for the vertical direction, the momentum equation becomes:

$$\begin{aligned}\frac{\partial \rho_a v_x}{\partial t} + \frac{\partial \rho_a v_x^2}{\partial x} + \frac{\partial \rho_a v_x v_y}{\partial y} + \frac{\partial \rho_a v_x v_z}{\partial z} = &- \frac{\partial p}{\partial x} + \frac{\partial}{\partial x}\left(2\mu_a \frac{\partial v_x}{\partial x}\right) + \frac{\partial}{\partial y}\left(\mu_a\left(\frac{\partial v_x}{\partial y} + \frac{\partial v_y}{\partial x}\right)\right) \\ &+ \frac{\partial}{\partial z}\left(\mu_a\left(\frac{\partial v_z}{\partial x} + \frac{\partial v_x}{\partial z}\right)\right) + f_{\sigma,x},\end{aligned} \tag{2.25}$$

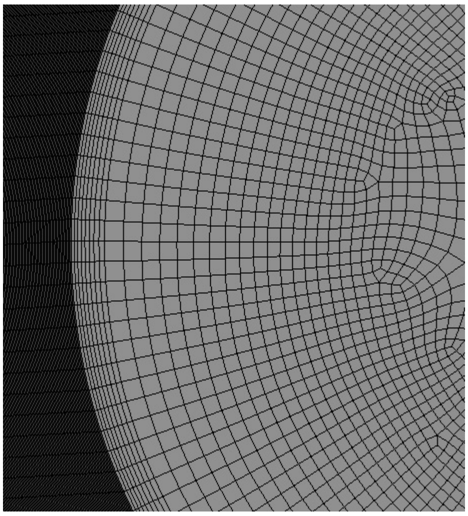

Figure 2.12: 3D mesh.

where $f_{\sigma,x}$ is the surface tension force term in the x direction,

$$\begin{aligned}\frac{\partial \rho_a v_y}{\partial t} + \frac{\partial \rho_a v_y v_x}{\partial x} + v_y \frac{\partial \rho_a v_y^2}{\partial y} + \frac{\partial \rho_a v_y v_z}{\partial z} = &-\frac{\partial p}{\partial y} + \frac{\partial}{\partial x}\left(\mu_a\left(\frac{\partial v_x}{\partial y} + \frac{\partial v_y}{\partial x}\right)\right) + \frac{\partial}{\partial y}\left(2\mu_a \frac{\partial v_y}{\partial y}\right) \\ &+ \frac{\partial}{\partial z}\left(\mu_a\left(\frac{\partial v_y}{\partial z} + \frac{\partial v_z}{\partial y}\right)\right) + f_{\sigma,y},\end{aligned} \tag{2.26}$$

where $f_{\sigma,y}$ is the surface tension force term in the y direction, and for the vertical direction:

$$\begin{aligned}\frac{\partial \rho_a v_z}{\partial t} + \frac{\partial \rho_a v_z v_x}{\partial x} + \frac{\partial \rho_a v_z v_y}{\partial y} + \frac{\partial \rho_a v_z^2}{\partial z} = &-\frac{\partial p}{\partial z} + \frac{\partial}{\partial x}\left(\mu_a\left(\frac{\partial v_z}{\partial x} + \frac{\partial v_x}{\partial z}\right)\right) + \frac{\partial}{\partial y}\left(\mu_a\left(\frac{\partial v_y}{\partial z} + \frac{\partial v_z}{\partial y}\right)\right) \\ &+ \frac{\partial}{\partial z}\left(2\mu_a \frac{\partial v_z}{\partial z}\right) - \rho_a g + f_{\sigma,z},\end{aligned} \tag{2.27}$$

where $f_{\sigma,z}$ is the vertical component of the surface tension force.

Simulation

Phase indicator initialization was performed by merging two bodies: a hemisphere and a cylinder. Note that this is analogous to revolving the initial 2D shape around the axis.

The convergence criteria in 3D simulations was 10^{-4}. All other simulation parameters were the same as for the 2D model. The validation of this numerical model is discussed in Chapter 4.

2.4 Experimental methods and apparatus

Even though the work is numerical, some experiments were required to validate the numerical results beyond the available data in literature. Chapter 4 presents the set-up and the experiments executed in this work. The following sections present also topics concerning the experimental methods employed.

2.4.1 Experimental apparatus

The experimental setup was specially designed for visualizing Taylor drops (Figure 2.13). The main section (or testing column Figure 2.14) consists of a 4 m long vertical acrylic tube. The apparatus allow for the usage of two different diameters: 21 mm and 32 mm. An open reservoir is connected to the top end of the testing column. The column and the reservoir were filled with the continuous phase liquid.

The visualization section in the testing column is located near the top in order to ensure the drop reaches the terminal velocity (post-processing of the visualization data can confirm that). The visualization section consists of an acrylic box that wraps the testing column. This box has rectangular faces and is filled with the continuous phase liquid to reduce optical distortion. In front of one of the rectangular faces, a camera is positioned to film the rising drop. At the opposite side, a light source is positioned. Images are taken at a rate of 25 s^{-1}. Prior to any experiment, the distances in the captured images were calibrated by positioning two stripes of millimetric paper in opposite sides of the visualization box.

The injection of the dispersed phase drop was made in a pre-chamber. An initial design was tested where the drop was fed through an horizontal tube (connected to a pre-chamber filled with continuous phase) which would drive the drop towards the basis of the testing column (configuration I in Figure 2.13 see also Figure 2.15). It was observed (due to the low density differences and the high viscosity of the liquids) that the drop stopped in the horizontal section. Another similar try was performed feeding the column by means of a vertical injector tube. However, this did not work either. A new configuration was then designed (configuration II in Figure 2.13). In this new design, the pre-chamber was filled with the dispersed phase and separated from the testing column by a spring and a level plug. The plug was then actioned to inject the Taylor drop into the testing column.

2.4.2 Images post-processing

The video provided by the camera was firstly subject to deinterlacing yielding the 25 frames per second of film. Secondly, the frames were separated into individual images (Figure 2.16).

The image processing was automated though a computer code. Firstly the images were converted to a grey scale according to a luminosity equation. Secondly, the grey scale was converted to a binary image by means of a threshold (whose value was previously defined for each pair of liquids in order to optimize the interface tracking). At this stage, the code identified a vertical line at the center of the tube and the tracking of the nose position was done. Hence, from the process, it was obtained the nose position as a function of time. A linear regression was done taking such results in order to determine the drop terminal velocity. Any deviation from a linear behavior would mean that the drop was not at its terminal velocity (never observed in this work).

2.4.3 Liquids

An initial research was performed in order to choose pairs of liquids that would be suitable for the numerical model validation.

Due to criteria as: cost, transparency and ease of operation (including safety), water and aqueous solutions of glycerin were chosen for the continuous phase. Another advantage of aqueous solutions of glycerin is their wide range of viscosities (from 1 mPa s to 1410 mPa s, at 20 °C).

Regarding the dispersed phase, the choice was an oil used as a car lubricant (Repsol Elite TDI 15W40). Figure 2.17 shows the results from the measurement of that oil viscosity done in a cone and plate rheometer, from low to high shear rate values. Other options taken in consideration were silicon

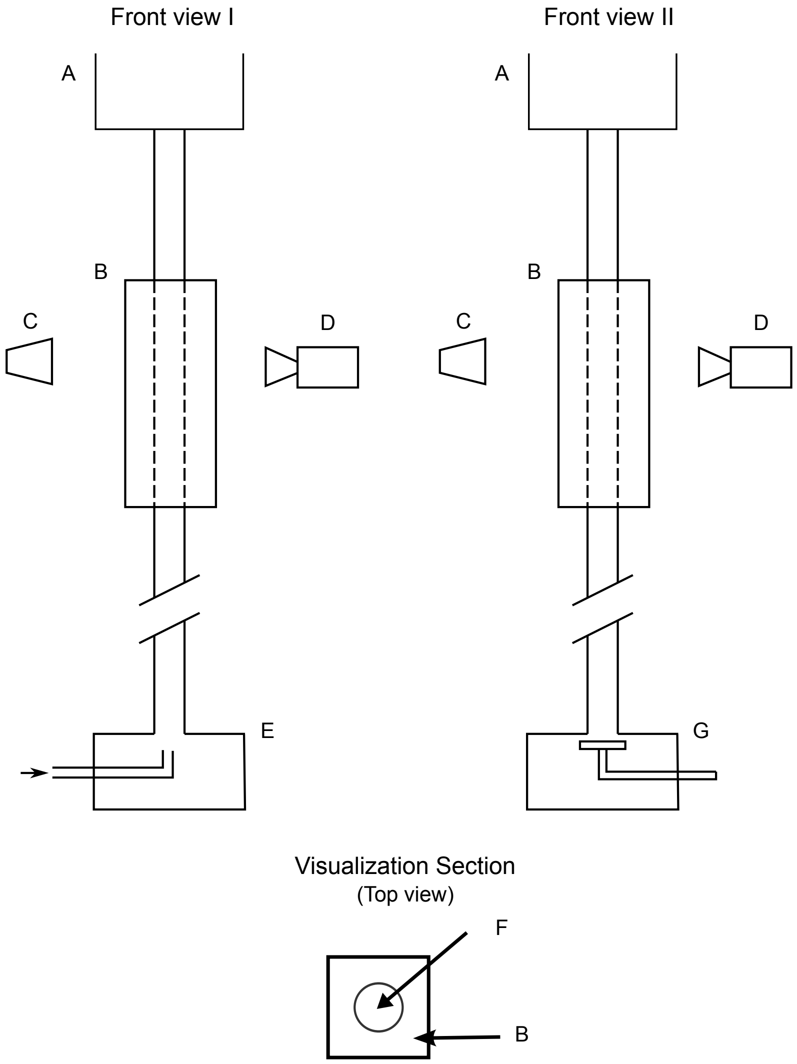

Figure 2.13: Experimental apparatus (A – top open reservoir, B – visualization box, C – light source, D – Camera, E – injection pre-chamber in configuration I, F – tube, G – injection pre-chamber in configuration II).

Figure 2.14: Testing column and visuatization box.

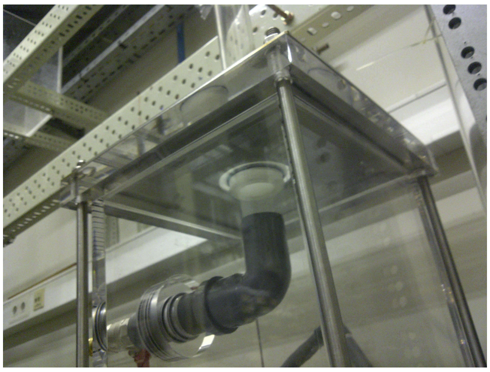

Figure 2.15: Pre-chamber in the first tested configuration.

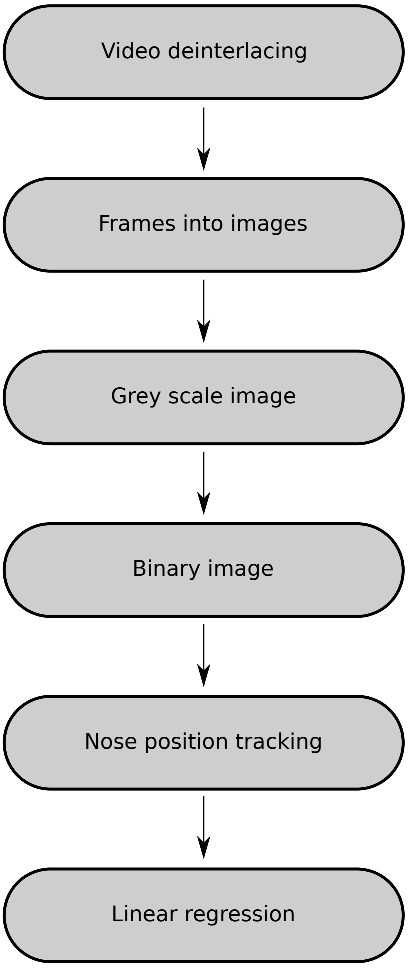

Figure 2.16: Video post-processing procedure.

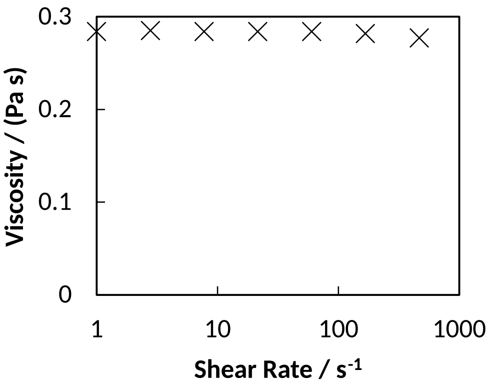

Figure 2.17: Viscosity of the oil used for the liquid-liquid visualizations.

Table 2.3: Experimental conditions for the air in water tests.

	air in water
ρ_C / kg m^{-3}	998
μ_C / Pa s	0.001
σ / N m^{-1}	0.072
ρ^*	0.0012
μ^*	0.018
Eo	60
M	2.66×10^{-11}

oils and olive oil. The low interfacial tension of the olive oil with the continuous phase liquids chosen would lead to elevated Eötvös numbers that were beyond the scope of this work.

2.4.4 Interfacial tension measurement

In the present work, the interfacial tensions were determined by the pendant drop method using a commercial system (Biolin Scientific Attension Theta). The system consists of a needle that slowly (manually) introduces a small drop of one liquid into a small translucent cuvette filled with the other liquid. A camera takes pictures and the computer software analyses the image in order to obtain the value for the interfacial tension. Prior to the test, a calibration is required so that the distances are measured correctly.

2.4.5 Experimental validation

Initial visualizations of air bubbles were conducted and the data compared to literature results in order to validate the experimental procedure (Table 2.3). Figure 2.18 depicts a Taylor air bubble flowing in a water continuous phase. Table 2.4 shows agreement with previously published results, thus validating the procedure.

Table 2.4: Results for the air in water tests.

Fr (this work)	Fr (Araújo et al., 2012; Morgado et al., 2016)
0.33	0.34

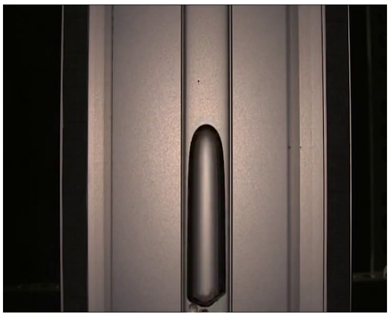

Figure 2.18: Air Taylor bubble in water.

References

Anderson, J. D. (1995), *Computational Fluid Dynamics*, McGraw-Hill.

Ansys Fluent (2011), *Theory Guide, Release 14.0*, Ansys, Inc.

Araújo, J. D. P., Miranda, J. M. and Campos, J. B. L. M. (2015), 'CFD Study of the Hydrodynamics of Slug Flow Systems: Interaction between Consecutive Taylor Bubbles', *International Journal of Chemical Reactor Engineering* **13**(4), 541–549.

Araújo, J., Miranda, J. and Campos, J. (2013), 'Simulation of slug flow systems under laminar regime: Hydrodynamics with individual and a pair of consecutive Taylor bubbles', *Journal of Petroleum Science and Engineering* **111**, 1–14.

Araújo, J., Miranda, J., Pinto, A. and Campos, J. (2012), 'Wide-ranging survey on the laminar flow of individual Taylor bubbles rising through stagnant Newtonian liquids', *International Journal of Multiphase Flow* **43**, 131–148.

Brackbill, J. U., Kothe, D. B. and Zemach, C. (1992), 'A Continuum Method for modeling surface tension', *Journal of Computational Physics* **100**, 335–354.

Campos, J. M. (2013), *Notas para o Estudo da Mecânica dos Fluidos*, 1.a edição edn, FEUP edições, Porto.

Carlson, A., Kudinov, P. and Narayanan, C. (2008), Prediction of two-phase flow in small tubes: a systematic comparison of state-of-the-art CMFD Codes, *in* '5th European Thermal-Sciencies Conference'.

Date, A. W. (2005), *Introduction to Computational Fluid Dynamics*, Cambridge University Press.

Deshpande, S. S., Anumolu, L. and Trujillo, M. F. (2012), 'Evaluating the performance of the two-phase flow solver interFoam', *Computational Science & Discovery* **5**(1), 014016.

Feng, J., Muradoglu, M., Kim, H., Ault, J. T. and Stone, H. A. (2016), 'Dynamics of a bubble bouncing at a liquid/liquid/gas interface', *Journal of Fluid Mechanics* **807**, 324–352.

Gerlach, D., Tomar, G., Biswas, G. and Durst, F. (2006), 'Comparison of volume-of-fluid methods for surface tension-dominant two-phase flows', *International Journal of Heat and Mass Transfer* **49**(3-4), 740–754.

Gunsing, M. (2004), Modelling bubbly flows using Volume of Fluid, Front Tracking and Discrete Bubble Models, PhD thesis, Twente University.

Hayashi, K., Kurimoto, R. and Tomiyama, A. (2011), 'Terminal velocity of a Taylor drop in a vertical pipe', *International Journal of Multiphase Flow* **37**(3), 241–251.

Hirt, C. W. and Nichols, B. D. (1981), 'Volume of Fluid (VOF) Method for the Dynamics of Free Boundaries', *Journal of Computational Physics* **39**, 201–225.

Hoang, D. a., van Steijn, V., Portela, L. M., Kreutzer, M. T. and Kleijn, C. R. (2013), 'Benchmark numerical simulations of segmented two-phase flows in microchannels using the Volume of Fluid method', *Computers & Fluids* **86**, 28–36.

Issa, R. I. (1986), 'Solution of the implicitly discretised fluid flow equations by operator-splitting', *Journal of Computational Physics* **62**(1), 40–65.

Leonard, B. P. (1979), 'A stable and accurate convective modelling procedure based on quadratic upstream interpolation', *Computer Methods in Applied Mechanics and Engineering* **19**(1), 59–98.

Lewis, R. W., Nithiarasu, P. and Seetharamu, K. N. (2004), *Fundamentals of the Finite Element Method for Heat and Fluid Flow*, Wiley.

Magnini, M., Pulvirenti, B. and Thome, J. (2016), 'Characterization of the velocity fields generated by flow initialization in the CFD simulation of multiphase flows', *Applied Mathematical Modelling* **0**, 1–20.

Morgado, A., Miranda, J., Araújo, J. and Campos, J. B. (2016), 'Review on vertical gas-liquid slug flow', *International Journal of Multiphase Flow* **85**, 348–368.

Munson, B. R., Young, D. F. and Okiishi, T. H. (2005), *Fundamentals of Fluid Mechanics*, 5th editio edn, John Wiley and Sons Ltd.

Patankar, S. V. (1980), *Numerical Heat Transfer And Fluid Flow*, Hemisphere.

Quan, S. (2011), 'Co-current flow effects on a rising Taylor bubble', *International Journal of Multiphase Flow* **37**(8), 888–897.

Taha, T. and Cui, Z. (2006), 'CFD modelling of slug flow in vertical tubes', *Chemical Engineering Science* **61**(2), 676–687.

Tuković, Ž. and Jasak, H. (2012), 'A moving mesh finite volume interface tracking method for surface tension dominated interfacial fluid flow', *Computers and Fluids* **55**(February), 70–84.

Ubbink, O. (1997), Numerical prediction of two fluid systems with sharp interfaces, PhD thesis, Imperial College of Science, Technology and Medicine.

Versteeg, H. K. and Malalasekera, W. (1995), *An introduction to Computational Fluid Dynamics*, Longman Scientific & Technical.

Weller, H. G. and Tabor, G. (1998), 'A tensorial approach to computational continuum mechanics using object-oriented techniques', *Computers in Physics* **12**(6), 620–631.

Wesseling, P. (2010), *Principles of Computational Fluid Dynamics*, kindle ed edn, Springer.

Youngs, D. L. (1982), Time-Dependent Multi-Material Flow with large Fluid Distorsion., *in* K. W. Morton and M. J. Baines, eds, 'Numerical Methods in Fluid Dynamics', Academic Press.

3

Rising of a single Taylor drop in a stagnant liquid – 2D laminar flow and axisymmetry limits

Direito, F. J. N., Campos, J. B. L. M. and Miranda, J. M. (2016), ‘Rising of a single Taylor drop in a stagnant liquid – 2D laminar flow and axisymmetry limits’, *Physics of Fluids* **28** (5), 057101.

Abstract

A numerical (CFD) study concerning the rise of individual liquid Taylor drops through vertical columns of stagnant heavier liquids is presented in this paper. CFD simulations were performed in Ansys Fluent, using its implementation of Volume of Fluid (VOF) method, assuming the flow to be axisymmetric and laminar. Different physical conditions were tested, corresponding to different combinations of relevant dimensionless parameters and the numerical method was validated through experimental data available in literature. The viscosity ratio between the lighter and the heavier liquid was within the range 0.01 to 40 and Eötvös number was between 8 and 30. Morton number was within the interval of 2.32×10^{-6} to 100. Froude number results were compared to data from a literature correlation. The accordance is acceptable for the ranges studied. Velocity profiles in significant regions are reported (drop nose, drop bottom and continuous phase liquid film). The influence of changing one dimensionless parameter alone was assessed. For small and large viscosity ratios, axisymmetric behavior is not a valid assumption.

3.1 Introduction

A field of increasing interest is concerning with the behavior of the flow in a tube of two immiscible liquids. Consider a flow in a tube where a continuous phase has dispersed drops of another fluid. If the flow rate of the dispersed phase suffers a significant increase, the drops increase in volume and start to coalesce, eventually forming very large drops occupying almost all the tube cross-section. The formation of intermittent (sometimes periodic) long bullet-shaped drops – Taylor drops – as for the liquid-gas case [1,2] is observed for high disperse phase flow rates.

Slug flow pattern is, sometimes, related to operating problems, drastic pressure oscillations and it can also increase the corrosion rate in long pipe walls [3,4].

Slug flow has also a huge importance due to its effects on heat and mass transfer rates in several industrial processes: nuclear industry, chemical reactors, or geothermal power facilities. Hydrocarbon transportation in pipes is another important example where slug flow happens [5,6], sometimes in a water-oil-gas slug flow, which, for certain conditions, resembles a liquid-liquid flow [7,8]. In particular, due to the increasing demands in oil wells extraction, there is a growing interest in liquid-liquid slug flow occurrence in vertical pipes [9,10].

In spite of such interest, there is still a lack of significant knowledge on liquid-liquid slug flow.

In order to go deeper on the study of continuous slug flow, one must focus the attention in a simplified description of such flow pattern: a Taylor drop rising in a stagnant liquid, i.e. a Taylor drop of the lighter liquid (dispersed phase) rising in the heavier liquid (continuous phase). It is expected that a rising solitary drop reaches, in a very short distance from the injection point, a constant terminal velocity value (V_{T}). By the rising of the Taylor drop, the heavier liquid is forced to flow down in the narrow space between the drop and the wall, creating a thin annular film flow that, eventually at some point, will become fully developed. When this fully developed film flow is reached, it is expected that the terminal velocity becomes independent of the drop length. In liquid-liquid flow, the drop viscosity is not negligible and it creates a non-zero shear stress in the interface between the two phases.

Another interesting behavior is the one found in the wake of Taylor gas bubbles flowing in a liquid. Depending on the flow conditions and liquid properties, the continuous phase is disturbed at the rear of the bubble and sometimes a closed recirculation region traveling attached to the bubble is observed[1]. Further insight is needed in order to reveal if such behavior is also found in liquid-liquid slug flow.

A dimensional analysis to the problem, as performed by Hayashi et al.[11], yields five dimensionless numbers, defined by:

$$\mathrm{Fr} = \frac{V_\mathrm{T}}{\sqrt{\Delta\rho\, gD/\rho_C}}, \tag{3.1}$$

$$\mathrm{Eo} = \frac{\Delta\rho\, gD^2}{\sigma}, \tag{3.2}$$

$$\mathrm{M} = \frac{\Delta\rho\, g\mu_C^4}{\rho_C^2\, \sigma^3}, \tag{3.3}$$

$$\rho^* = \frac{\rho_D}{\rho_C}, \tag{3.4}$$

$$\mu^* = \frac{\mu_D}{\mu_C}, \tag{3.5}$$

where the subscript "$_D$" stands for the dispersed phase and "$_C$" for the continuous phase; ρ is the fluid density and μ the viscosity, D the tube diameter, g the standard gravity and σ the surface tension. Moreover, $\Delta\rho = \rho_C - \rho_D$. The Froude number (Fr) relates inertial and gravity forces and includes the terminal velocity. It is usually used as output of numerical and experimental studies about slug flow. The Eötvös number (Eo) relates buoyancy and interfacial forces. The Morton number (M) compares viscosity and surface tension effects[12]. The density ratio (3.4) and the viscosity ratio (3.5) compare the physical properties of both liquids. For a Taylor drop rising in a stagnant liquid, ρ^* is always less than 1. Although the dimensionless groups presented suffice, another groups cited in the literature are the Reynolds number (Equation 3.6) and the inverse viscosity number (Equation 3.7)[11,13],

$$\mathrm{Re} = \frac{\rho_C V_\mathrm{T} D}{\mu_C} = \mathrm{Fr}\,\mathrm{M}^{-1/4}\,\mathrm{Eo}^{3/4}, \tag{3.6}$$

$$\mathrm{N_f} = \frac{\sqrt{\Delta\rho\,\rho_C g D^3}}{\mu_c} = \left(\frac{\mathrm{Eo}^3}{\mathrm{M}}\right)^{1/4}. \tag{3.7}$$

Also relevant is the ratio between the drop volume-equivalent sphere and the pipe diameter (d_S/D), which gives information on drop size.

Brown and Govier[14] and Govier et al.[15] were the pioneers to study vertical oil-water flow, having reported, amongst other patterns, slug flow.

There are already some attempts to describe the flow of a Taylor drop in a stagnant liquid. Mandal et al.[16] made a theoretical analysis to predict the terminal velocity by adopting a viscous potential flow analysis. They obtained an equation explicit in Froude number (and on terminal velocity, as well), which is dependent on the density of the liquids, surface tension, pipe diameter and continuous phase viscosity. The equation features also a drop shape parameter. Experiments were performed with values of $4 < \mathrm{Eo} < 230$ and $10^{-13} < \mathrm{M} < 10^{-10}$. Density ratios were between 0.65 and 0.88 and viscosity ratios between 0.68 and 1.2. The surface tension in those liquids lies between 0.02 and 0.06 $\mathrm{Nm^{-1}}$. Mandal et al.[17],[18] performed further experimental studies concerning identical systems. A wake region was observed, distinguishable due to the presence of small dispersed drops. They claim that the drop shape for their conditions was axisymmetric, even though the bottom shows oscillations with apparently no periodic pattern. Equations developed in the above works[16,18] are limited to conditions where the effect of drop viscosity is negligible.

Hayashi et al.[11] performed lab experiments and CFD simulations to study the rise velocity of a Taylor drop. The experimental conditions consisted of a density ratio around 0.8, a viscosity ratio between 0.1 and 20, and a surface tension between 0.02 and 0.04 $\mathrm{Nm^{-1}}$. The diameters of the tubes were between 11 and 31 mm, the Eötvös number between 10 and 100, and the Morton number ranged between 0.00002 and 0.35. They focused on drop shapes cataloging and on the development of a correlation to predict Froude number. They claim that the density ratio does not influence the Froude number and they also observed that when the continuous phase viscosity is much higher than the dispersed phase viscosity, the Froude number approaches 0.35. They propose an equation to predict Froude number. This equation features an important difference to the previous ones: it takes into account the influence of the dispersed phase viscosity by including μ^*. That correlation was slightly changed by Kurimoto et al.[19]. Kurimoto et al.[19] also show non-symmetrical Taylor drops on certain conditions. Quan and Lou[13] proposed a power law to predict Froude number, based on a numerical study.

The aim of the present work is to obtain data about the flow of a single Taylor drop in a stagnant heavier liquid in a long vertical pipe. Computational Fluid Dynamics (CFD) tools were applied to simulate flow for a large range of values of the dimensionless groups defined above. This work is also the first step of a broader research on slug flow and on its relevance and applications in oil wells. CFD is an attractive choice because with it, one can easily change the operating conditions, geometry or fluid properties. Moreover, CFD is also an easy tool to obtain relevant information, such as velocity field, streamlines and pressure gradients. The numerical data obtained were validated through experimental data taken from Hayashi et al.[11].

In the present work, conditions considered lie in the ranges: $0.01 < \mu^* < 40$, $8 < \mathrm{Eo} < 30$, $2.32 \times 10^{-6} < \mathrm{M} < 100$ and $\rho^* = 0.792$ for two immiscible liquids. Simulations were performed in Ansys Fluent, in transient and axisymmetric modes, assuming laminar regime and incompressible flow.

Terminal velocity values (or its dimensionless number Fr), obtained from the simulations, were compared to Kurimoto et al.[19] correlation data. The dispersed phase viscosity is one of the parameters taken into account in the present work. The influence of Eötvös number was also assessed. Moreover, axial and radial velocity profiles in relevant regions of the flow were also analyzed. Finally, the limitations of axisymmetric assumption are discussed.

3.2 Theory and empirical background

Algorithm development for CFD is dependent on the differential description of the fluid flow. Momentum equation is given by:

$$\rho_a \left(\frac{\partial \vec{v}}{\partial t} + \vec{v} \cdot \nabla \vec{v} \right) = -\nabla p + \rho_a \vec{g} + \nabla \cdot \mu_a \left(\nabla \vec{v} + (\nabla \vec{v})^T \right) + \vec{f_\sigma}, \tag{3.8}$$

where p is the pressure and $\vec{f_\sigma}$ is the force term that represents the surface tension contribution. Moreover, because the flow is incompressible, continuity equation states[20,21]:

$$\nabla \cdot \vec{v} = 0. \tag{3.9}$$

In order to deal with the two-phase flow through Volume of Fluid method (VOF), a variable α_i is defined to track the position of the interface. The value of α_i is 1 at any point occupied exclusively by the fluid i, 0 if no i exists there, or a number between 0 and 1, if both fluids exist in the same mesh volume. Notice that a number between 0 and 1 does not mean that the two liquids are mixed (we are assuming they are immiscible). In any element of a mesh:

$$\alpha_C + \alpha_D = 1. \tag{3.10}$$

Furthermore, the tracking of the interface between the two phases is solved by the equation:

$$\frac{\partial \alpha_i}{\partial t} + \nabla \cdot (\alpha_i \vec{v_i}) = 0. \tag{3.11}$$

Density and viscosity are computed supposing linear contributions of each phase (Equations 3.12 and 3.13).

$$\rho_a = \alpha_C \rho_C + \alpha_D \rho_D, \tag{3.12}$$

$$\mu_a = \alpha_C \mu_C + \alpha_D \mu_D. \tag{3.13}$$

Finally, the surface tension term $\vec{f_\sigma}$ must be computed[22]:

$$\vec{f_\sigma} = \sigma \kappa \frac{\rho_a \nabla \alpha_D}{0.5\,(\rho_C + \rho_D)}. \tag{3.14}$$

The κ refers to the curvature of the interface and is computed by:

$$\kappa = -\nabla \cdot \frac{\nabla \alpha_D}{|\vec{\nabla} \alpha_D|}. \tag{3.15}$$

Notice that, outside interface, $\kappa = 0$, so $\vec{f_\sigma} = \vec{0}$, which eliminates the surface tension term in Equation 3.8.

3.2.1 Single Taylor drop

In the analysis of a single Taylor drop rising in a stagnant liquid, the important fluid properties are density and viscosity. Moreover, surface and gravity forces should be considered as well. For so large drops, the tube diameter becomes the controlling geometrical parameter[23]. It is expected that a single rising drop reaches, in a very short distance from the injection point, a constant terminal velocity value V_T. When the frontal region of the drop (nose) is perfectly spherical, terminal velocity is not dependent on the surface tension between the two fluids[24,16].

Mandal et al.[16],[18] proposed equations to predict the terminal velocity based on viscous potential flow and also a semi-empirical equation. However, those equations do not take into account the dispersed phase viscosity, which is relevant in liquid-liquid systems.

Hayashi et al.[11] showed that Froude number is not influenced by the density ratio and used numerical and experimental data to estimate the parameters of a Froude number correlation (Equation 3.16), which, the authors claim, is valid in the ranges: $4.8 < \mathrm{Eo} < 228$; $1 < \mathrm{N_f} < 14700$; $10^{-12} < \mathrm{M} < 10^{4}$; $\mu^* < 70$;

$0.002 < \mathrm{Re} < 4960$,

$$\mathrm{Fr} = \sqrt{\frac{0.0089\left(1 + 41/\mathrm{Eo}^{1.96}\right)^{-4.63}}{0.0725 + \frac{1}{\mathrm{Re}}\left(\frac{1+1.9\mu^*}{1+0.31\mu^*}\right)\left(1 - 0.11\mathrm{Re}^{0.33}\right)}}. \tag{3.16}$$

For Equation 3.16, Hayashi et al.[11] assumed that the terminal velocity is independent from drop length when $d_S/D < 1.6$. Furthermore, in gas-liquid conditions (zero viscosity and density ratios), Hayashi et al.[11] force the known limit of 0.35 for Froude number. They adjust their correlation to the relation $\mathrm{Fr} = 0.01\mathrm{N_f}$ (viscous force dominant regime), as well as to experimental results from White and Beardmore[25]. They finally used simulation results to complete their correlation. The effect of the velocity in the interface is included implicitly in the approximations described before.

Equation 3.16 has the important feature of including the drop viscosity (through μ^*). Afterwards, the authors presented a correction to it[19]:

$$\mathrm{Fr} = \sqrt{\frac{A_2 \cdot A_3}{\frac{A_3}{0.35^2} + \frac{1+1.9\mu^*}{1+0.31\mu^*}A_1}}, \tag{3.17}$$

where A_i are defined by the following equations:

$$A_1 = \mathrm{Re}^{-1}\left(1 - 0.05\sqrt{\mathrm{Re}}\right), \tag{3.18}$$

$$A_2 = \left(1 + 3.87\,\mathrm{Eo}^{-1.68}\right)^{-18.4}, \tag{3.19}$$

$$A_3 = 0.0025\left(3 + A_2\right). \tag{3.20}$$

Quan and Lou[13] propose the relation:

$$\mathrm{Fr} = B\,\mu^{-0.27\pm0.05}, \tag{3.21}$$

where B depends on $\mathrm{N_f}$ and Eo. Even though all presented results stay below the 0.35 Froude number limit, some series of simulations show a trend which is likely to pass that limit. Therefore, this correlation will not be used for comparison in the following sections.

A diagram of an axisymmetric Taylor drop is presented in Figure 3.1. Regions of interest include the film formed around (annular) the drop and enclosed between it and the wall and the nose region (top dotted line) because those are related to the drop velocity. Furthermore, because of interaction between two drops, it is also of interest to assess how far on the continuous phase, the drop influence takes effect, which is related to the behavior of the bottom part of the drop. Concerning the influence above the drop, the procedure taken in this work evaluates where, in the axis, the velocity is no longer higher than a certain criteria. A similar procedure is taken to evaluate the influence below the drop. In the present work, two criteria were used: 5 % and 1 % of the drop terminal velocity.

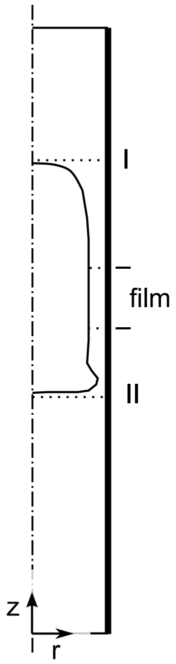

Figure 3.1: Axisymmetric Taylor drop.

3.3 CFD model

The simulations presented in the current work were performed with the commercial software Ansys Fluent (releases 14 and 15), in transient mode. Multiphase laminar incompressible flow model integrated with Volume of Fluid (VOF) method to capture the liquid-liquid interface was used[26] with geometric reconstruction[27] - "Geo-reconstruct" in the software package. Preliminary simulations showed that this method is the best choice concerning two common problems[28,29]: spurious velocities and numerical dispersion. The pressure-velocity scheme used was PISO, which provides a fast convergence. For pressure interpolations, the choice was "PRESTO!". The QUICK scheme was used for solving the momentum equation and the gradients of the scalars were computed by using the Green-Gauss node-based method. For the surface tension effect, the Continuum Surface Force model[22] was used.

The simulations were performed with a variable time-step option and a maximum Courant number of 0.25. A limit of 1000 iterations for each time-step was imposed. Nevertheless, this limit was never reached, which ensures that convergence criteria was met in every time-step.

Axial symmetry (around the cylinder axis) was used to minimize computational effort (3D behavior is simulated in 2D). The domain consisted of a rectangle with a width $D/2$ and $11D$ long. The domain needs to be long enough so that the continuous phase is undisturbed at the entrance and at the exit. The mesh consisted of a 52×1144 grid of quadrilateral and uniformly distributed cells. The continuous phase film flow region thickness was usually between 10 and 15 cells. A finer grid (7.8 times more cells) was also used in preliminary tests, but showed identical results and it was dropped due to computation time.

Simulations were initialized with an isolated drop consisting of the merge of two shapes: a quarter of a circle for the drop nose region and a rectangular body, with a width matching the nose radius. Although other initialization strategies can be found in literature, this starting shape has been found to give good results[30].

Table 3.1: Validation of numerical runs – Froude number results.

Id.	Eo	M	μ^*	This work (numerical)	Literature data: experimental[11]	Literature data: correlation[19]
Run1	76	3.2×10^{-3}	1.1	0.282	0.280	0.261
Run2	29	2.0×10^{-5}	1.1	0.301	0.290	0.266
Run3	7.2	1.3×10^{-5}	3.9	0.0145	0.0160	0.0139
Run4	91	0.39	1.9	0.116	0.120	0.121

A reference frame attached to the drop nose was used. This reference frame attached to the drop (to its nose) implicates that the drop is still and the continuous phase and the tube wall move downwards with a speed that equals the drop terminal velocity. The usage of this strategy avoids the need of a very long domain. No-slip condition was also assumed in the wall. Furthermore, due to the relative motion created by the reference frame, an inlet flow boundary condition, with a uniform velocity (equal to V_{T}) was imposed at the top of the domain. At the exit, pressure is specified (pressure-outlet boundary condition in the software package used).

The final result for each condition is obtained by an iterative method. Firstly, inlet and wall velocities are imposed based on literature correlations, and a first simulation runs. After, drop velocity in the moving reference is determined and if it is higher than a given tolerance, wall and inlet velocities are changed, and a new simulation is performed. This process repeats until drop velocity is less than the criterion established (less than 0.01). Then, the correct value of the terminal velocity is found.

The interface between the liquids is not abrupt. Instead, a small numerical dispersion of the volume fraction occurs. In this work, it is assumed that the interface is represented by $\alpha = 0.5$. Concerning the viscosity in the numerical interface, a linear model is used (Equation 3.13). Some authors suggest, instead, the usage of the harmonic mean[28,31]. Such suggestion was employed in preliminary simulation for the M = 2.32×10^{-6} series, but showed no significant differences.

3.3.1 CFD 2D model validation

The numerical model has already been extensively used in liquid-gas systems[1,30]. In order to validate the liquid-liquid numerical data, four simulations (Table 3.1) were performed according to four experimental results available in literature[11]. Froude number data from numerical runs show good accordance with literature experimental data. A further comparison can be made concerning the drops shapes (Figure 3.2). Run1 shows an elongated and straight body with a small concavity in its bottom part. Run4 show a straight and elongated body, as well, but with a very wide continuous phase film. Run2 is fairly straight but showing a protuberance at the end of the continuous phase liquid. Finally, Run3 is round-shaped in the bottom, with a large body, including in the nose region. These shapes are qualitatively similar to those reported by Hayashi et al.[11].

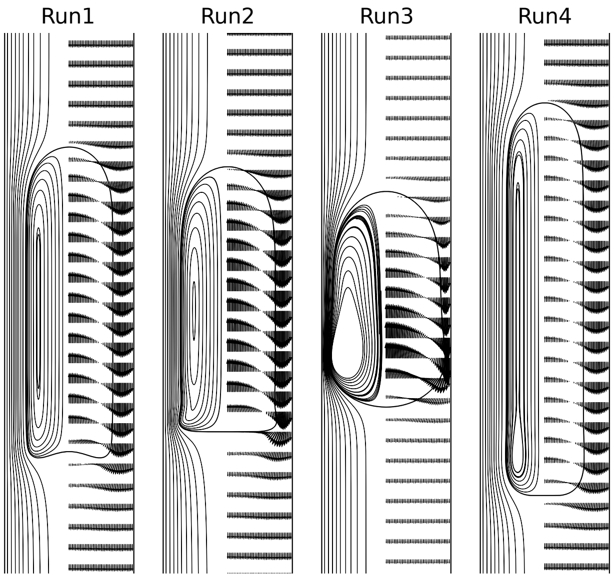

Figure 3.2: Validation of numerical model - drops, streamlines and velocity field (drop reference frame).

3.4 Results

The results section contains, firstly an overview on the Froude number results for the range of dimensionless numbers for which drops can be treated as symmetric. Afterwards, relevant comparisons are done for selected groups of simulations. Finally, limitations of axisymmetry are discussed. Because we assume axisymmetric flow, velocity components are presented as radial, r, and axial (or vertical), z. Axial direction is upwards, i.e. gravity is negative. All simulations share the same drop size ($d_S/D = 1.147$). Note that this value ensures that we obtain the physical phenomena intended without compromising time efficiency with very long domains. Furthermore, density ratio is also the same throughout the present work (0.792), since density ratio does not influence Froude number[11]. Note also that Hayashi et al.[11] use values between 0.74 and 0.81 and Mandal et al.[18] present results with values between 0.65 and 0.87.

Results on relevant regions of the flow are reported, as shown in Figure 3.1. Line I refers to the horizontal profiles just above the drop and Line II to the horizontal profiles just below the drop. Furthermore, it is also important to assess how far does the drop influence takes effect on the continuous phase. Such influence distance above the drop is obtained by evaluating the velocity along the tube axis. A similar procedure is taken for the influence below the drop.

Prior to further developments, though, it is important to refer that the results presented are limited to the ranges of the parameters where Taylor drops can be assumed axisymmetric. Higher values of Eötvös number lead to numerical issues with implausible drop rupture. Viscosity ratio values outside the ranges presented yield flows which are not axisymmetric, even though there is no drop rupture. This is discussed in more detail in section 3.4.3. All simulations have a Froude number value within the maximum deviation interval of 25 % from Equation 3.17.

3.4.1 Drop terminal velocity

Firstly, Froude number (or terminal velocity) is analyzed as a function of the viscosity ratio and results compared to data given by Equation 3.17[19]. In Figure 3.3, three series of data for different Eötvös numbers are presented for a constant $\mathrm{M} = 2.32 \times 10^{-6}$. In this range, simulations are in good agreement

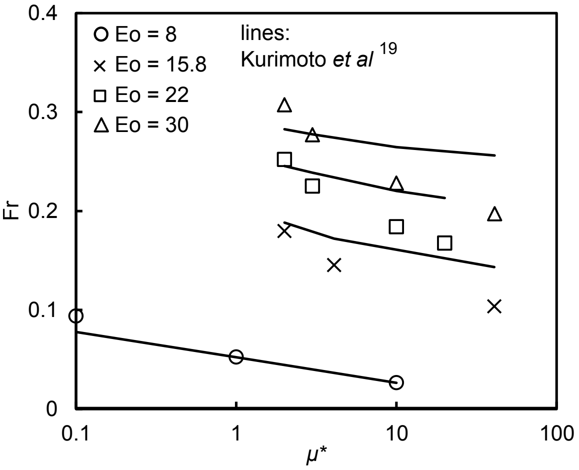

Figure 3.3: Froude number for M = 2.32 × 10^{-6} as a function of viscosity ratio.

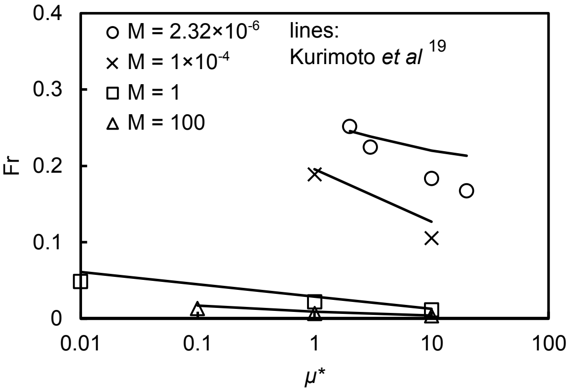

Figure 3.4: Froude number for Eo = 22 as a function of viscosity ratio.

with the correlation near $1 < \mu^* < 3$, showing an acceptable, but sharper variation when progressing apart from that range. Higher values of Eötvös number yield higher values of Froude number, while the increase in the viscosity ratio tends to lower the Froude number. The increase of μ^* causes a retarding in the flow. This result is also important because it confirms the relevance of the drop viscosity in liquid-liquid systems.

For Eo = 22, the value of Froude number increases as Morton number decreases (Figure 3.4). Another important observation is the proximity of the series M = 1 and M = 100. Results agree fairly with Equation 3.17, though showing a sharper variation of Froude number for the smaller Morton number series. Simulations were also performed for Eo = 8 and higher Morton number values (Figure 3.5). Such conditions yield low Froude number values. In this range, a decrease of two in the order of magnitude of the viscosity ratio causes Froude number to double its value.

3.4.2 Detailed flow patterns

A summary of drop shapes, streamlines and velocity field is presented in Figure 3.6 for four different Morton values, and three different Eötvös at $\mu^* = 1$ and $\mu^* = 10$.

The individual influences of Eötvös and Morton numbers and viscosity ratio are detailed in the

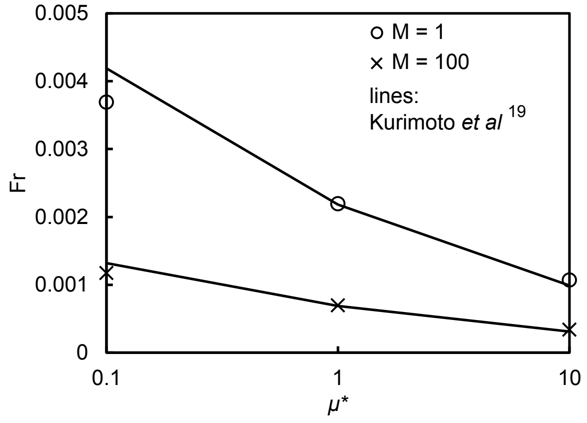

Figure 3.5: Froude number for Eo = 8 as a function of viscosity ratio.

following sections.

Eötvös number effect

Figure 3.7 compares drop shape for three different values of Eötvös number for constant Morton number and viscosity ratio. Streamlines are drawn with respect to the drop reference frame. A clear change in the drop shape is observable. For Eo = 15.8 the drop rear has a round shape. For Eötvös number value of 30, the drop bottom is almost horizontal. It also shows a sharper narrowing at the end of the film. On these conditions, closed vortexes zones below the drops do not exist.

Notice that the ten streamlines are positioned taking into account that the outer the radial coordinate, the higher the flow area (axisymmetry). Therefore, between any two streamlines flows the same continuous phase flow rate. The reference frame attached to the drop nose was used to compute the streamlines.

No substantial differences are observed in the film velocity profile (Figure 3.8). The maximum downward velocity occurs within the film. That is in contrast with liquid-gas, where the maximum lies on the gas-liquid interface[32,33]. A result expected due to the significant drop viscosity. The film thickness is also similar for the presented data. Near the wall, the velocity approaches to zero (no-slip) condition.

Figures 3.9 and 3.10 compare the velocity profiles just below the drop (Line II in Figure 3.1). The higher the Eötvös number, the higher is the maximum downward velocity component. This is consistent with the observed drop bottom shape, as discussed before, where the sharper narrowing yields a greater downward velocity of the continuous phase.

The negative peaks (direction towards the center) observed in the radial component near the end of the film are consistent with the sharper bending in Eötvös number 22 and 30. The radial profile for Eötvös number 22 shows the highest peak. The three profiles reach the null value as they approach the axis, as imposed by the axisymmetric condition.

The profiles at the top of the drop (Line I in Figure 3.1)are identical for the three simulations (Figure 3.11 and Figure 3.12). The axial component has the value of V_{T}near the axis (the nose is "pushing" the fluid above it) and a negative value in the region nearer the wall, consistent with the beginning of the flow around the drop. In the same fashion, the positive values of the radial component are consistent with the fluid being deflected due to the approach of the drop.

That is interesting to observe that, both in the nose and in the film, the three conditions yield almost indistinguishable profiles. It is in the drop rear that the changing of the Eötvös number causes effect.

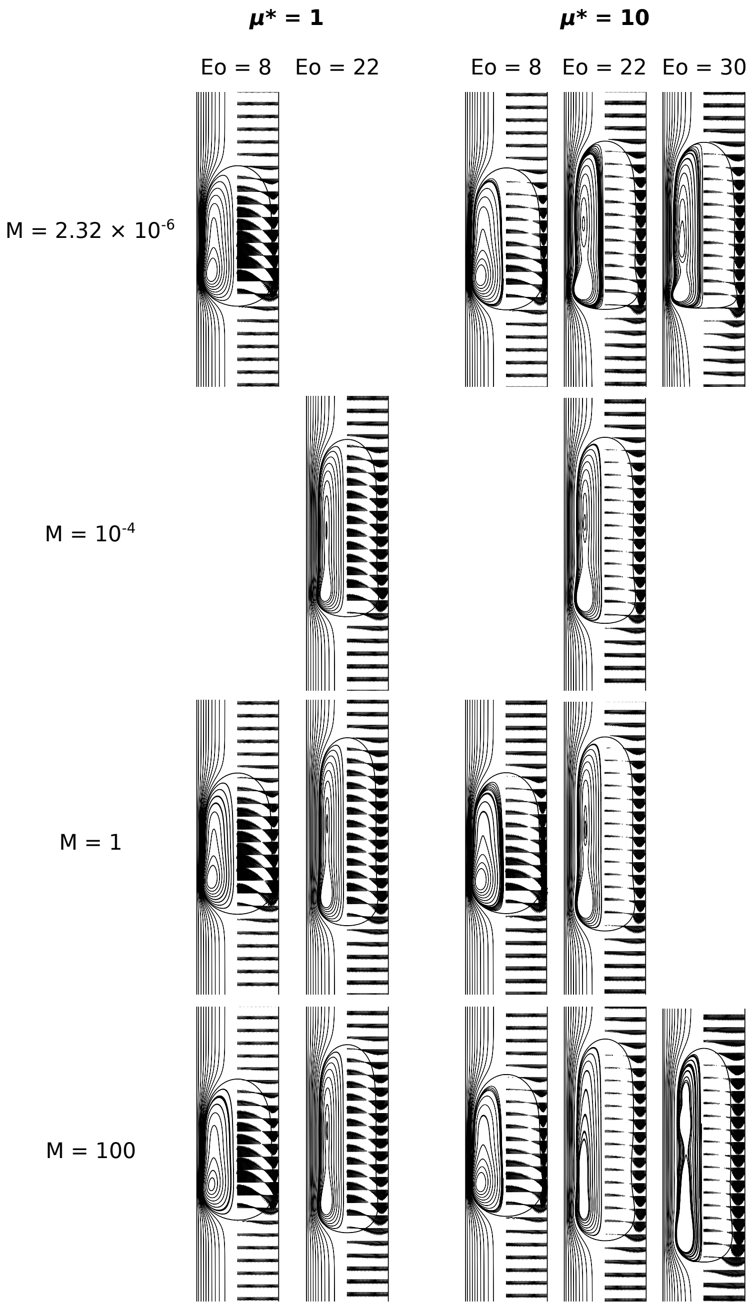

Figure 3.6: Compilations of drop shapes, streamlines and velocity field (drop reference frame).

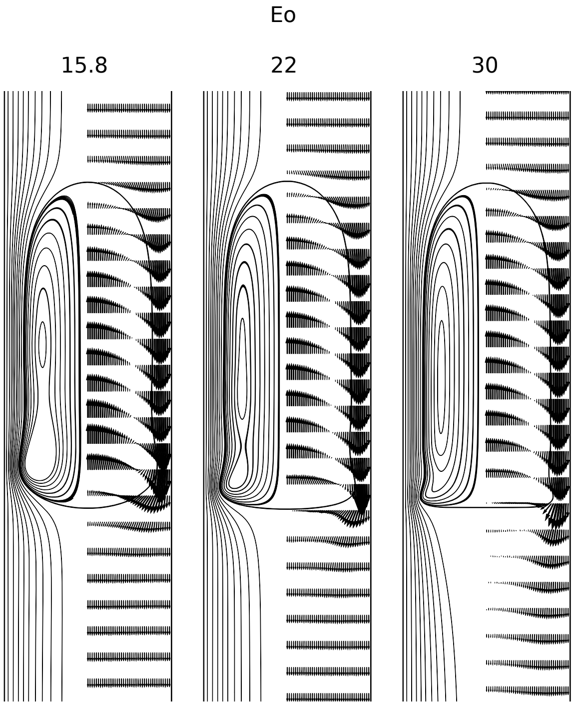

Figure 3.7: Streamlines for M = 2.32×10^{-6} and $\mu^* = 2$.

Table 3.2: Influence distances below the drop for M = 2.32×10^{-6} and $\mu^* = 2$.

Eo	5 % of V_T $(z - z_{rear})/D$	1 % of V_T $(z - z_{rear})/D$
15.8	0.65	1.4
22	0.77	1.6
30	2.8	4.3

Influence distances below the drop are presented in Table 3.2. The procedure taken in this work evaluates where, along the axis, the velocity is no longer higher than a decided criterion (0.05 or 0.01 in relation to the drop terminal velocity).

Viscosity ratio effect

At constant Morton number of 2.32×10^{-6} and Eötvös number of 22, three simulations are compared, changing the viscosity ratio. All three drops show a bottom slightly curved as well as a slight narrowing at the end of the film (Figure 3.13). Between viscosity ratios of 2 and 3, no differences are clear. On the other hand, at viscosity ratio 10 the drop is more elongated and velocity magnitude inside the drop becomes very small in comparison to the velocity in the film (note that an increase in viscosity ratio means an increase in the drop viscosity). On these conditions, recirculation zones below the drops do not exist.

Concerning the velocity profile in the film (Figure 3.14), the peak is displaced from the interface, as it is expected from a considerable viscosity ratio. It is also observable a slight increase of the film thickness for the greater viscosity ratios, which is consistent with the shape in Figure 3.13. The profiles are similar between the wall and the peak of velocity. After that position, the velocities diverge. With the increase of the viscosity ratio, the magnitude of the downward velocity decreases. At $\mu^* = 10$, dispersed phase

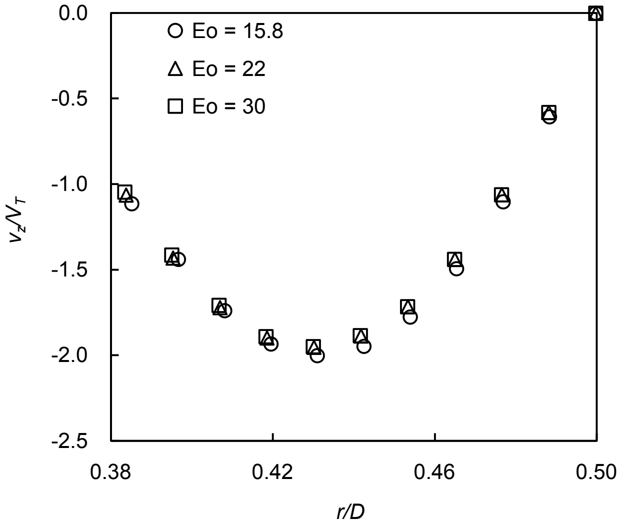

Figure 3.8: Velocity profile in the film for M = 2.32×10^{-6} and $\mu^* = 2$.

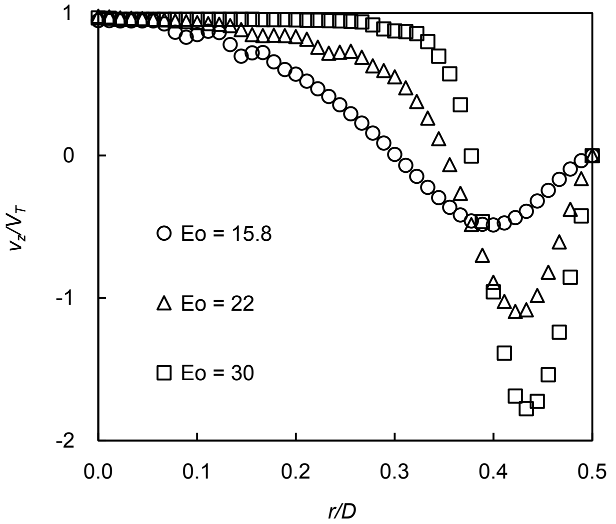

Figure 3.9: Axial velocity below the drop for M = 2.32×10^{-6} and $\mu^* = 2$.

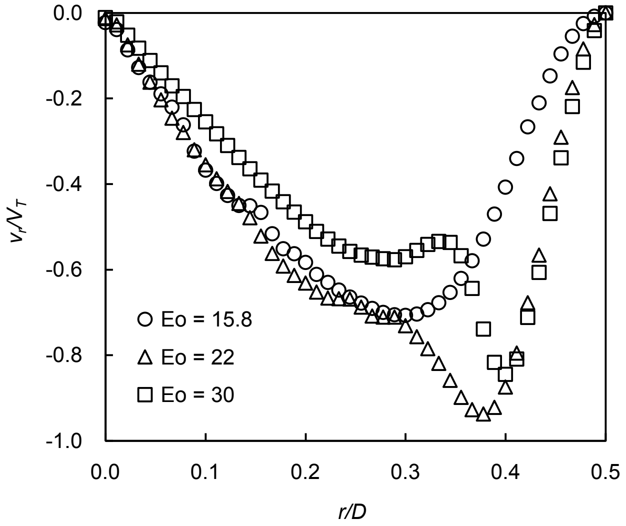

Figure 3.10: Radial velocity below the drop for M = 2.32×10^{-6} and $\mu^* = 2$.

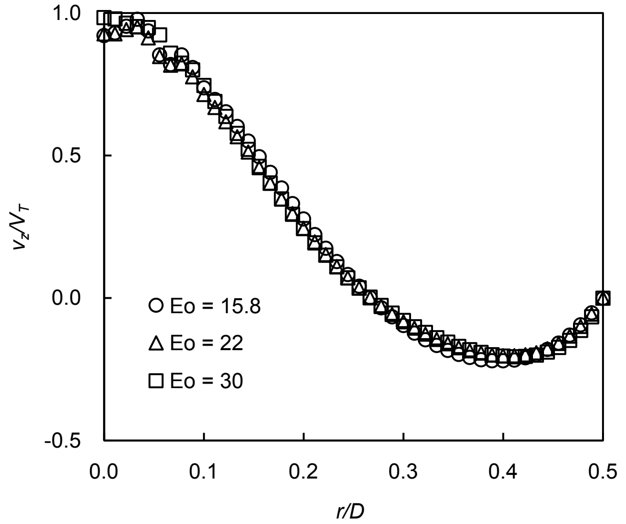

Figure 3.11: Axial velocity above the drop for M = 2.32×10^{-6} and $\mu^* = 2$.

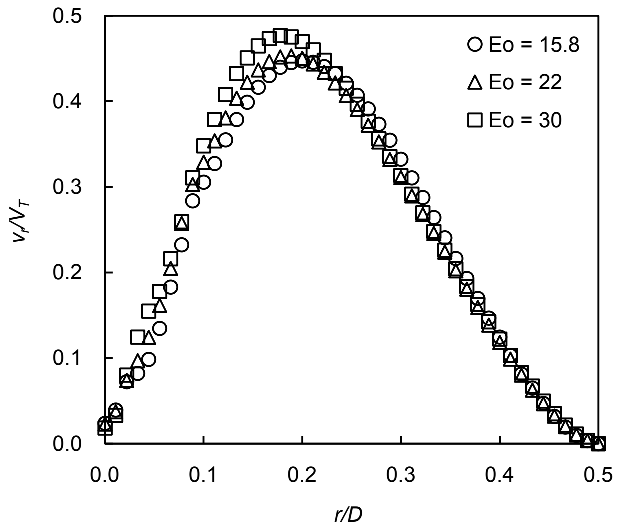

Figure 3.12: Radial velocity above the drop for M = 2.32×10^{-6} and $\mu^* = 2$.

Table 3.3: Influence distances for M = 2.32×10^{-6} and Eo = 22.

μ^*	5 % of V_T $(z - z_{rear})/D$	1 % of V_T $(z - z_{rear})/D$
2	0.77	1.6
3	0.68	1.3
10	1.1	1.8

viscosity is so relevant that, at the interface, the continuous phase is slightly pulled upwards.

Just below the drop, the axial component is almost unchanged between the three viscosity ratios (Figure 3.15). In the radial profiles (Figure 3.16) the behavior is analogous, although the magnitude tends to be lower with the increase of the viscosity ratio.

Profiles at the top of the drop are very similar to those in the previous section and are omitted from this discussion. For the influence distances below the drop (Table 3.3), results show a decrease from viscosity ratio 2 to viscosity ratio 3, and an increase when viscosity ratio is changed to 10. Two effects may be observed here. Firstly, form $\mu^* = 2$ to $\mu^* = 3$, the decrease in drop velocity causes a decrease on the disturbance of the continuous phase. When increasing viscosity ratio to 10, another effect, the significant change in the drop shape (in particular at the bottom – the liquid narrows increasing the film velocity), takes effect, and causes the increase in the influence distances.

Morton number effect

In this third group, Morton number is changed for four conditions at constant Eötvös number and viscosity ratio. In this conditions Morton number takes the values of 2.32×10^{-6}, 10^{-4}, 1 and 100. Eötvös number is 22 and viscosity ratio is 10 (fourth column in Figure 3.6).

Concerning the drop shape (Figure 3.6), there is a noticeable increase in the drop length from Morton number 2.32×10^{-6} to Morton number 1. On the other hand, the increase of Morton number from 1 to 100 seems to cause little difference.

Close attention to the shape allows to disclosure a shape type change between the lower Morton number value and the others. In the first, there is a mild, but clear, narrowing below the film. On the others, though, there is almost no narrowing. Therefore, it is expected that such transition is also

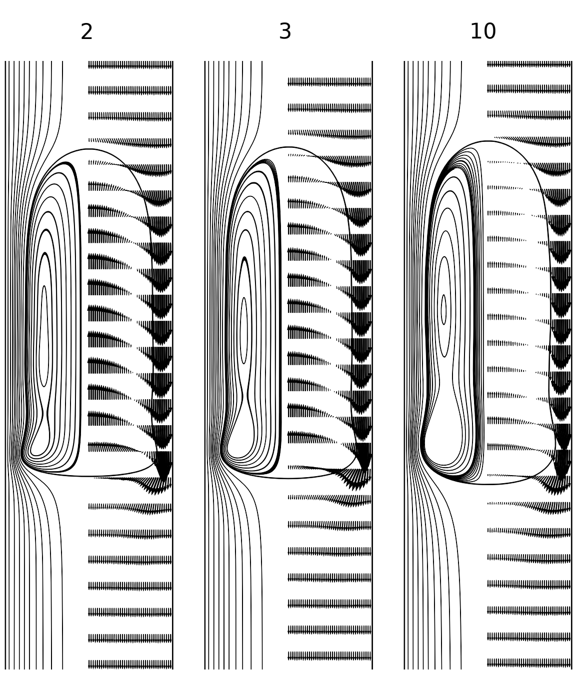

Figure 3.13: Streamlines for $M = 2.32 \times 10^{-6}$ and $Eo = 22$.

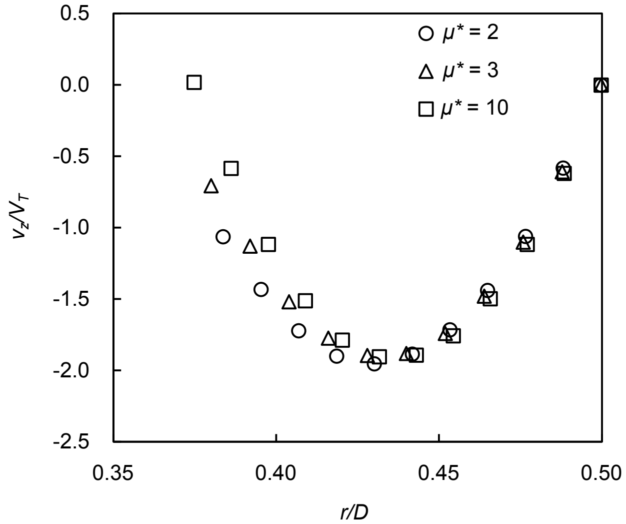

Figure 3.14: Axial velocity profile in the film for $M = 2.32 \times 10^{-6}$ and $Eo = 22$.

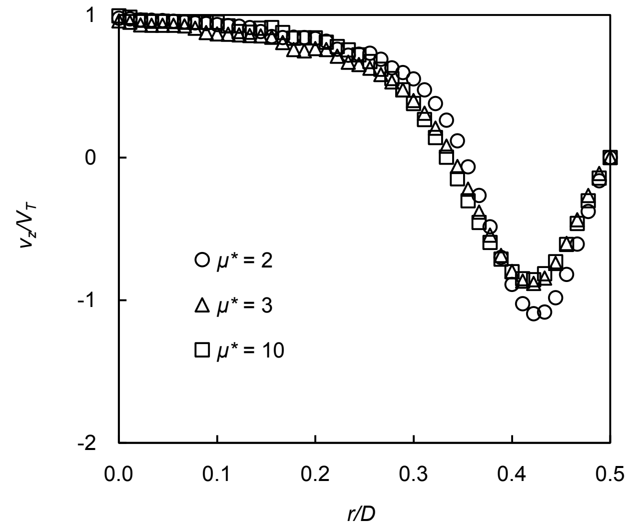

Figure 3.15: Axial velocity below the drop for M = 2.32×10^{-6} and Eo = 22.

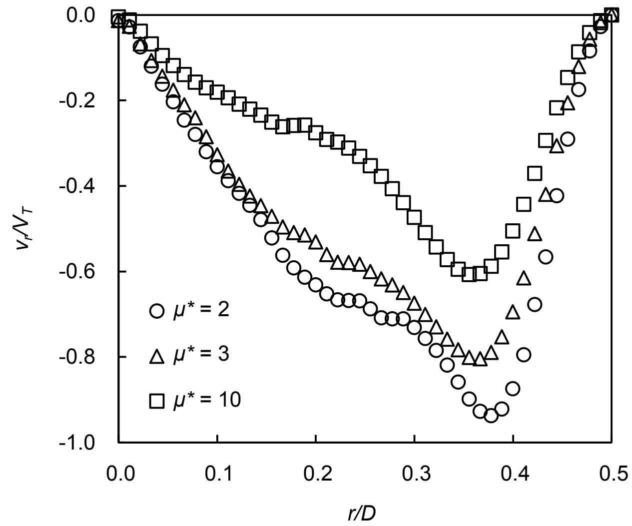

Figure 3.16: Radial velocity below the drop for M = 2.32×10^{-6} and Eo = 22.

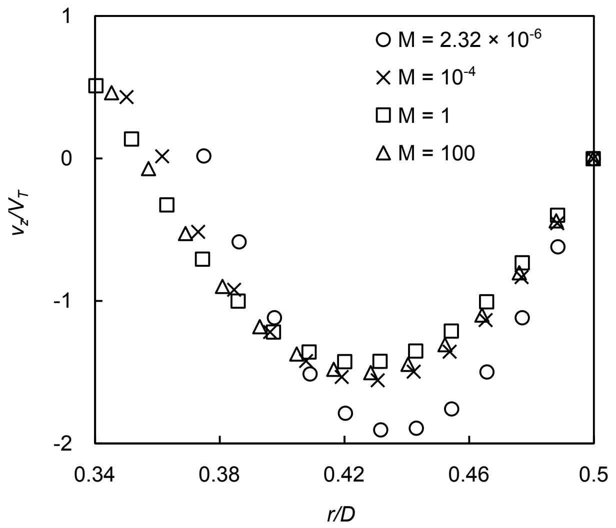

Figure 3.17: Velocity profile in the film for Eo = 22 and $\mu^* = 10$.

Table 3.4: Influence distances for Eo = 22 and $\mu^* = 10$.

M	5 % of V_T $(z - z_{rear})/D$	1 % of V_T $(z - z_{rear})/D$
2.32×10^{-6}	1.1	1.8
10^{-4}	0.50	0.68
1	0.43	0.58
100	0.41	0.57

noticeable on the velocity profiles.

It is also important to point out that the significant increase in drop length is not accompanied by such a drastic change in the film thickness, because in the region near the wall, the flow area is larger than in the axis region, for an identical radius increase (recall that the domain is axisymmetric).

Concerning the continuous phase film velocity profile (Figure 3.17), the data from Morton number 2.32×10^{-6} show an higher vertical velocity maximum in a clear distinction from the other three cases. It is also clear the difference between the film thickness for this Morton number and for the others. Between Morton number 10^{-4}, 1 and 100, there is almost no difference in the film thickness.

In the profiles below the drop (Figures 3.18 and 3.19), once again the lower Morton number simulation shows up differences, and higher velocity magnitudes (recall the sharper narrowing and bend shown before).

At the top of the drop nose, the axial component show no further information and it is omitted. On the other hand, the radial profile (Figure 3.20), shows a noticeable difference between the two lower Morton number values and the two higher, which show no difference between each other.

Finally, the magnitude of the influence lengths below and above the drop (Table 3.4) confirms the previous statements; i.e., no difference between M = 1 and 100. Above the drop, the two higher Morton numbers have slightly higher influence lengths.

3.4.3 Limitations of axisymmetry

Despite the non-existence of drop collapse, for some simulated drops (in the axisymmetric domain), the terminal velocities obtained did not make physical sense. Moreover, some of them even overcome the

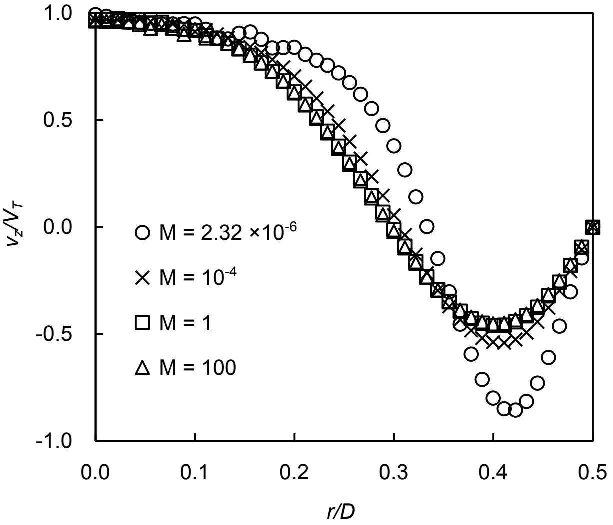

Figure 3.18: Axial velocity below the drop for Eo = 22 and $\mu^* = 10$.

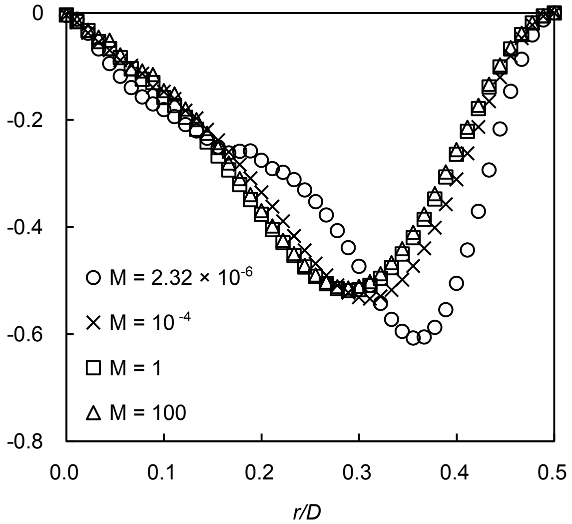

Figure 3.19: Radial velocity below the drop for Eo = 22 and $\mu^* = 10$.

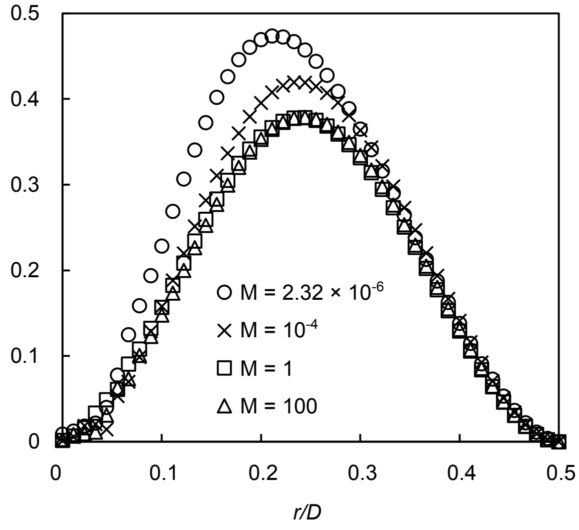

Figure 3.20: Radial velocity above the drop for Eo = 22 and $\mu^* = 10$.

limit Froude number taken in literature to be around 0.35. In order to understand if there is a limitation to axisymmetric two-phase flow, some 3D simulations were performed.

Figure 3.21 shows a comparison between 2D axisymmetric and 3D for three different cases (at $M = 2.32 \times 10^{-6}$). Concerning the first row ($\mu^* = 0.1$ and Eo = 22), drop from 2D simulation is stable but the Froude number is much larger than 0.35 (Figure 3.22). When the same conditions were simulated in 3D, it was found that the drop is not axisymmetric and Froude number improves to a value closer to 0.267, as predicted by Equation 3.17. The second row ($\mu^* = 3$ and Eo = 30) shows similar Froude number results between 2D and 3D. Furthermore, 3D shape is similar to 2D, confirming the flow is axisymmetric. In this case, Froude number is, for 2D and 3D, very close to the value predicted by Equation 3.17, 0.276. For the last case ($\mu^* = 20$ and Eo = 22), the simulation in 2D yielded an apparently good drop, but it did not correspond to the behavior in 3D. For the first and third 3D simulations in Figure 3.21, it was also observed that the drop shape was unstable. Even though we use here simulations with distinct Eötvös numbers, that difference is not large enough to influence the current analysis.

The present results suggest that, for large differences between the viscosities of both fluids, the flow becomes asymmetric.

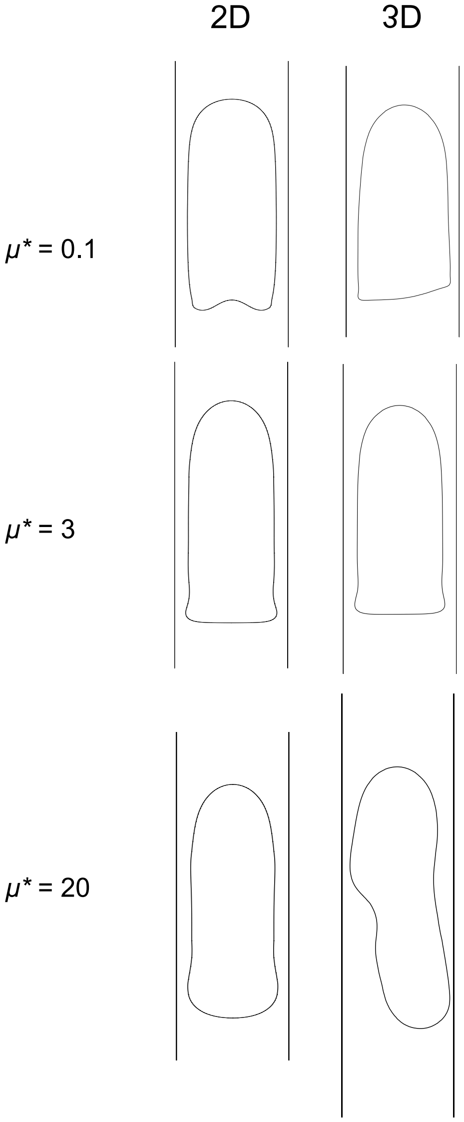

Figure 3.21: Drop shapes of 2D and 3D simulations in vertical slices through the center, at $\mathrm{M} = 2.32\times10^{-6}$ (middle: $\mathrm{Eo} = 30$; others: $\mathrm{Eo} = 22$).

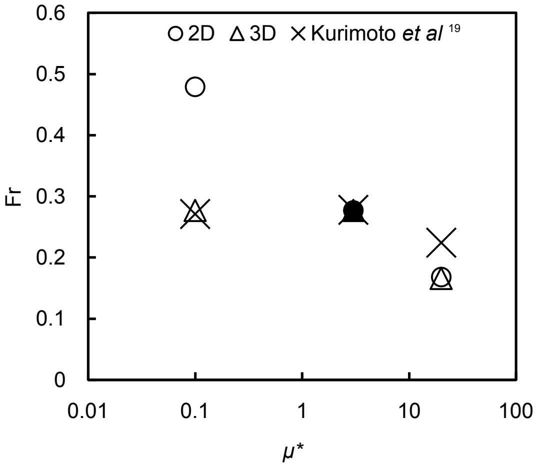

Figure 3.22: Froude number for in 2D and 3D, at M = 2.32×10^{-6} (filled: Eo = 30; unfilled: Eo = 22).

3.5 Conclusions

The importance of slug flow for several industrial processes motivated the present work.

A study concerning single liquid Taylor drops rising at constant velocity in a stagnant heavier liquid is reported. Numerical simulations were performed assuming an axisymmetric flow. From numerical data, it was possible to extract information on drop shape, streamlines and velocity profiles on several regions of the flow system. The parameters studied were found to be in accordance. Four preliminary simulations were compared to available experimental data providing validation of the numerical model.

Results were reported for ranges of Eötvös number, Morton number and viscosity ratio. Furthermore, information on drop terminal velocity was collected and, with that, it was possible to relate Froude number with the other dimensionless quantities.

Froude number results were compared to data of a correlation (Equation 3.17) available in literature[19], being within a limit difference of 25 %. Viscosity effects cause a decrease in the drop terminal velocity. An increase of viscosity ratio causes a decrease in Froude number. In a similar fashion, it happened for an increase in Morton number.

Eötvös number was shown to affect mainly the drop bottom. On the other hand, Morton number and viscosity ratio produce changes in the continuous phase flow near the drop nose, as well as in the film around the drop. Moreover, an increase in the viscosity ratio causes a significant decrease in the velocity magnitude (relative to the continuous phase velocity) inside the drop.

Concerning the conditions presented in this work, there are no recirculation regions in the wake of the drops.

The developed film of the continuous phase showed a maximum of downward velocity located somewhere in the film, according to the viscosity ratio. Moreover, when viscous effect is high enough, velocity in the interface can point upwards. These results point out a clear difference between gas-liquid and liquid-liquid Taylor drops.

For several conditions, it was observed a significant narrowing in the continuous phase below the developed film, which influences the flow of the continuous phase after the passage of the drop. This behavior is important when two drops flow consecutively interacting.

Overall, the axisymmetric methodology developed is an efficient way of simulating Taylor drops within specific ranges. It was shown that for large and small viscosity ratios, the flow is not axisymmetric.

Nevertheless, the results reported in this work reveal a promising methodology for more complex systems, such as coalescence of two consecutive drops rising in laminar regime.

Acknowledgments

This work was funded by FEDER funds through the Operational Programme for Competitiveness Factors COMPETE and National Funds through FCT (Fundação para a Ciência e a Tecnologia) under the project PEst-OE/EME/UI0532. Filipe Direito gratefully acknowledge the financial support from the FCT through Ph.D. Grant SFRH/BD/79264/2011.

References

[1] J.D.P. Araújo, J.M. Miranda, A.M.F.R. Pinto, and J.B.L.M. Campos. Wide-ranging survey on the laminar flow of individual Taylor bubbles rising through stagnant Newtonian liquids. *International Journal of Multiphase Flow*, 43:131–148, jul 2012. ISSN 03019322. doi: 10.1016/j.ijmultiphaseflow.2012.03.007.

[2] R. M. Davies and G. Taylor. The Mechanics of Large Bubbles Rising through Extended Liquids and through Liquids in Tubes. *Proceedings of the Royal Society A: Mathematical, Physical and Engineering Sciences*, 200(1062):375–390, feb 1950. ISSN 1364-5021. doi: 10.1098/rspa.1950.0023.

[3] W C Lyons and G J Plisga. *Standard handbook of petroleum and natural gas engineering.* Elsevier, 1999.

[4] J. Villarreal, D. Laverde, and C. Fuentes. Carbon-steel corrosion in multiphase slug flow and CO2. *Corrosion Science*, 48(9):2363–2379, sep 2006. ISSN 0010938X. doi: 10.1016/j.corsci.2005.09.003.

[5] A.C. Bannwart, O.M.H. Rodriguez, F.E. Trevisan, F.F. Vieira, and C.H.M. de Carvalho. Experimental investigation on liquidliquidgas flow: Flow patterns and pressure-gradient. *Journal of Petroleum Science and Engineering*, 65(1-2):1–13, mar 2009. ISSN 09204105. doi: 10.1016/j.petrol.2008.12.014.

[6] Norman J Clark. *Elements of Petroleum Reservoirs (Henry L. Doherty series).* Society of Petroleum Engineers of AIME, revised ed edition, 1969.

[7] Adriane B S Serapião and Antonio C Bannwart. Knowledge Discovery for Classification of Three-Phase Vertical Flow Patterns of Heavy Oil from Pressure Drop and Flow Rate Data. *Journal of Petroleum Engineering*, 2013, 2013.

[8] PL Spedding, GS Woods, RS Raghunathan, and JK Watterson. Flow Pattern, Holdup and Pressure Drop in Vertical and Near Vertical Two-and Three-Phase Upflow. *Chemical Engineering Research and Design*, 78(3):404–418, 2000.

[9] Antonio C. Bannwart, Oscar M. H. Rodriguez, Carlos H. M. de Carvalho, Isabela S. Wang, and Rosa M. O. Vara. Flow Patterns in Heavy Crude Oil-Water Flow. *Journal of Energy Resources Technology*, 126(3):184, 2004. ISSN 01950738. doi: 10.1115/1.1789520.

[10] T.K. Mandal, G. Das, and P.K. Das. An appraisal of liquidliquid slug flow in different pipe orientations. *International Journal of Multiphase Flow*, 36(8):661–671, aug 2010. ISSN 03019322. doi: 10.1016/j.ijmultiphaseflow.2010.04.002.

[11] K. Hayashi, R. Kurimoto, and A. Tomiyama. Terminal velocity of a Taylor drop in a vertical pipe. *International Journal of Multiphase Flow*, 37(3):241–251, apr 2011. ISSN 03019322. doi: 10.1016/j.ijmultiphaseflow.2010.10.008.

[12] Tiago Sotto Mayor M. Santos. *Hydrodynamics of gas-liquid flows in Slug Flow regime.* PhD thesis, Universidade do Porto, 2007.

[13] Shaoping Quan and Jing Lou. Viscosity-ratio-based scaling for the rise velocity of a Taylor drop in a vertical tube. *Physical Review E*, 84(3):1–6, 2011. ISSN 1539-3755. doi: 10.1103/PhysRevE.84.036320.

[14] RAS Brown and GW Govier. High-Speed Photography in the Study of Two-Phase Flow. *The Canadian Journal of Chemical Engineering*, 39:159–164, 1961.

[15] GW Govier, GA Sullivan, and RK Wood. The Upward Vertical Flow of Oil-Water Mixtures. *The Canadian Journal of Chemical Engineering*, 39:67–75, 1961.

[16] T. K. Mandal, G. Das, and P. K. Das. Prediction of rise velocity of a liquid Taylor bubble in a vertical tube. *Physics of Fluids*, 19(12):128109, 2007. ISSN 10706631. doi: 10.1063/1.2824414.

[17] T.K. Mandal, G. Das, and P.K. Das. Motion of Taylor Bubbles and Taylor Drops in Liquid-Liquid Systems. *Industrial & Engineering Chemistry Research*, 47(18):7048–7057, 2008.

[18] T. K. Mandal, G. Das, and P. K. Das. Liquid Taylor Bubbles Rising in a Vertical Column of a Heavier Liquid: An Approximate Analysis. *Journal of Fluids Engineering*, 131(1):011303, 2009. ISSN 00982202. doi: 10.1115/1.3026730.

[19] Ryo Kurimoto, Kosuke Hayashi, and Akio Tomiyama. Terminal velocities of clean and fully-contaminated drops in vertical pipes. *International Journal of Multiphase Flow*, 49:8–23, mar 2013. ISSN 03019322. doi: 10.1016/j.ijmultiphaseflow.2012.08.001.

[20] B R Munson, D F Young, and T H Okiishi. *Fundamentals of Fluid Mechanics.* John Wiley and Sons Ltd, 5th editio edition, 2005.

[21] João Moreira Campos. *Notas para o Estudo da Mecânica dos Fluidos.* FEUP edições, Porto, 1.a edição edition, 2013. ISBN 9789727521579.

[22] J U Brackbill, D B Kothe, and C Zemach. A Continuum Method for modeling surface tension. *Journal of Computational Physics*, 100:335–354, 1992.

[23] R Clift, J R Grace, and M E Weber. *Bubbles, Drops and Particles.* Dover Publications Inc., New York, 2005.

[24] Daniel D. Joseph. Rise velocity of a spherical cap bubble. *Journal of Fluid Mechanics*, 488:213–223, jul 2003. ISSN 00221120. doi: 10.1017/S0022112003004968.

[25] E.T. White and R.H. Beardmore. The velocity of rise of single cylindrical air bubbles through liquids contained in vertical tubes. *Chemical Engineering Science*, 17(5):351–361, 1962. ISSN 00092509. doi: 10.1016/0009-2509(62)80036-0.

[26] C W Hirt and B D Nichols. Volume of Fluid (VOF) Method for the Dynamics of Free Boundaries. *Journal of Computational Physics*, 39:201–225, 1981.

[27] D L Youngs. Time-Dependent Multi-Material Flow with large Fluid Distorsion. In K. W. Morton and M. J. Baines, editors, *Numerical Methods in Fluid Dynamics.* Academic Press, 1982. ISBN 9780125083607.

[28] A Carlson, P Kudinov, and C Narayanan. Prediction of two-phase flow in small tubes: a systematic comparison of state-of-the-art CMFD Codes. In *5th European Thermal-Sciencies Conference*, 2008.

[29] Ruben Scardovelli and Stéphane Zaleski. Direct Numerical Simulation of Free-Surface and Interfacial Flow. *Annual Review of Fluid Mechanics*, 31(1):567–603, jan 1999. ISSN 0066-4189. doi: 10.1146/annurev.fluid.31.1.567.

[30] J.D.P. Araújo, J.M. Miranda, and J.B.L.M. Campos. Simulation of slug flow systems under laminar regime: Hydrodynamics with individual and a pair of consecutive Taylor bubbles. *Journal of Petroleum Science and Engineering*, 111:1–14, nov 2013. ISSN 09204105. doi: 10.1016/j.petrol.2013.10.007.

[31] Shaoping Quan. Co-current flow effects on a rising Taylor bubble. *International Journal of Multiphase Flow*, 37(8):888–897, 2011. ISSN 03019322. doi: 10.1016/j.ijmultiphaseflow.2011.04.004.

[32] H. L. Goldsmith and S. G. Mason. The movement of single large bubbles in closed vertical tubes. *Journal of Fluid Mechanics*, 14(01):42, 1962. ISSN 0022-1120. doi: 10.1017/S0022112062001068.

[33] Ryo Kurimoto, Kosuke Hayashi, and Akio Tomiyama. Terminal velocity of a single drop in a vertical pipe in clean and fully-contaminated systems. In *7th International Conference on Multiphase Flow, ICMF 2010, Tampa, FL, May 30 - June 4, 2010*, number 7, pages 1–11, 2010.

4

Experimental and numerical 3D study of a Taylor drop rising in a stagnant heavier liquid

Direito, F. J. N., Morgado, A. O., Rocha, L. A. M., Miranda, J. M. and Campos, J. B. L. M. (2017), ‘Experimental and numerical 3D study of a Taylor drop rising in a stagnant heavier liquid’, *Physics of Fluids* **29** (3), 037109.

Abstract

The present work concerns 3D numerical simulations and experiments on the rise of individual liquid Taylor drops through vertical columns of stagnant heavier liquids. Asymmetric effects are assessed for different conditions, following the observations in a previous work. Furthermore, the disturbances in the continuous phase due to the Taylor drop are studied. Experiments were performed with pairs of liquids in ranges not studied in the literature. Simulations targeted a broad range of dimensionless numbers and were done in a commercial code, using its implementation of the Volume of Fluid (VOF) method in a three-dimensional domain. Results were processed according to relevant dimensionless numbers. Different behaviors are found concerning the existence or not of flow and drop shape asymmetries. Depending on the viscosity ratio, three ranges with different characteristics were identified. Relevant results are also reported concerning drop velocity when compared to literature two-dimensional model. Drop influence in the surrounding continuous phase is also reported.

4.1 Introduction

Multiphase flows occur in several industries, such as chemical, nuclear, or hydrocarbon transportation[1,2]. Consider a particular example where two immiscible liquids flow in a vertical tube. One of those liquids, the heavier, constitutes a continuous phase where dispersed drops of another liquid are present. If the flow rate of the dispersed phase undergoes a significant increase, drops start to coalesce, forming very large drops occupying almost all the tube cross-section – Taylor drops[3]. Such flow pattern is called slug flow[4]. Depending on the geometric and flow parameters, slug flow may occur in co-current or in counter-current and most of the times coalescence of Taylor drops is observed. Because of its intermittence, slug flow is often related to operational problems in industry[5,6]. On the other hand, slug flow can be explored for the benefit of some operations, for instance, for the ability of lubricating the flow of a very viscous and wall-adherent dispersed phase.

Liquid-liquid slug flow has recently sparked interest for its importance in oil wells[7,8]. Furthermore, some gas-water-oil flows resemble two-phase liquid-liquid slug flow[9,10]. Nevertheless, and as opposed to gas-liquid slug flow, there is still a lack of knowledge on liquid-liquid slug flow. In order to gain a deeper understanding of such phenomena, one must firstly focus attention in a simplified description: a single Taylor drop rising in a stagnant liquid contained in a vertical column (a Taylor drop of the lighter liquid – dispersed phase – rising in the heavier liquid – continuous phase). It is expected that a rising solitary drop reaches, in a very short distance and from the injection point, a constant terminal velocity value (V_T). The heavier liquid is forced, by the drop upward flow, to flow down in the narrow space between the drop and the pipe wall, creating a thin annular film.

A dimensional analysis to the problem[11,12] yields five dimensionless numbers. Froude number,

$$\mathrm{Fr} = \frac{V_\mathrm{T}}{\sqrt{\Delta\rho\, gD/\rho_\mathrm{C}}}, \tag{4.1}$$

relates inertial and gravity forces. It is the dimensionless number usually used to quantify the constant terminal velocity, thus it serves as the main output from Taylor drop studies. On that equation, ρ is the density, D stands for the tube diameter, g for the standard acceleration of gravity. Finally, $\Delta\rho = \rho_\mathrm{C} - \rho_\mathrm{D}$, where the subscripts "$_\mathrm{D}$" and "$_\mathrm{C}$" stand for dispersed and continuous phase. In gas-liquid flows, Froude number is usually defined without $\Delta\rho/\rho$, as the gas density is much smaller than the liquid one[13,14].

Furthermore:

$$\mathrm{Eo} = \frac{\Delta\rho\, g D^2}{\sigma}, \tag{4.2}$$

$$\mathrm{M} = \frac{\Delta\rho\, g \mu_\mathrm{C}^4}{\rho_\mathrm{C}^2\, \sigma^3}, \tag{4.3}$$

where Eo is for Eötvös number (involving ratio between buoyancy and interfacial forces) and M the Morton number (gravity, viscosity and surface tension forces). μ stands for viscosity and σ for the interfacial tension between the two liquids.

The ratios between the liquids properties are the remaining dimensionless numbers:

$$\rho^* = \frac{\rho_\mathrm{D}}{\rho_\mathrm{C}}, \tag{4.4}$$

$$\mu^* = \frac{\mu_\mathrm{D}}{\mu_\mathrm{C}}. \tag{4.5}$$

The density ratio is always less than 1 as the present work deals with rising drops.

The combination of Eötvös number, Morton number and viscosity ratio allow for a characterization of the phenomena.

When Eötvös number is high and the viscosity ratio is low enough, the liquid-liquid isolated drop case approaches the behavior of a gas Taylor bubble rising in a liquid contained in a macro tube. That happens because the density difference is high and/or the interfacial tension is low (gravity effects are predominant).

When Eötvös number is low, Morton is required to quantify the importance of the viscous forces. Low Eötvös and high Morton numbers implicate a high viscosity of the continuous phase. If the viscosity ratio is high, such combination implies that, at the macro-scale, both fluids have close densities (viscous effects are predominant). For low Eötvös and Morton numbers and low viscosity ratio, the flow should be similar to that of a gas Taylor bubble flowing in a liquid contained in a micro tube (surface tension effects are predominant).

Apart from the physical dimensionless numbers, the ratio between the diameter of the drop volume-equivalent sphere and the pipe diameter (d_S/D) gives information on drop size.

Brown and Govier[15] and Govier et al.[16] studied vertical oil-water flow, having reported several flow patterns including slug flow. Zukoski[17] studied the influence of viscosity, surface tension and inclination angle on the rise of single drops (as well as bubbles). Later, Mandal et al.[18],[19],[20] performed experimental studies concerning several combinations of two liquids. A wake region was observed, distinguishable due to the presence of small dispersed drops. They claimed that the drop shape for their conditions was ax-isymmetric, even though the bottom showed asymmetric oscillations with apparently no periodic pattern. Hayashi et al.[11] performed lab experiments and Computational Fluid Dynamics (CFD) simulations to study the rise velocity of a Taylor drop. From CFD studies, they concluded that the density ratio does not influence the Froude number. Hayashi et al.[11] observed the known upper limit of 0.35[21] for that dimensionless number.

Concerning Froude number prediction in liquid-liquid, Mandal et al.[18],[20] obtained an estimation of the terminal velocity based on viscous potential flow and also a semi-empirical equation, not taking into account the dispersed phase viscosity, which is relevant mostly in liquid-liquid systems. Joseph[22], Mandal et al.[18] claimed that when the frontal region of the drop ("nose") is perfectly spherical, terminal velocity is not dependent on the surface tension between the two fluids. Kurimoto et al.[23] presented a correlation (a correction similar to the one in Hayashi et al.[11]) which takes into account the drop viscosity. Quan and Lou[24] proposed a power law to predict Froude number, based on a numerical study.

A relevant discussion concerns the symmetry effects on the rise of single Taylor drops in a stagnant liquid. If the flow is axisymmetric, theoretical and numerical models can be simplified to two-dimensions. However, in some conditions, two-dimensional models fail to describe the physical phenomena.

Mandal et al.[18],[19] presented figures where asymmetries in the bottom part of the drop are observable, though it is not clear how this influences the overall behavior of the drop. Mandal et al.[19] also observed asymmetric drops for a high viscous oil drop rising in water. In this work, differences are observable in the drop body shape. Kurimoto et al.[23] presented a snake-like behavior for Taylor drops in a region of high Eötvös number and low Morton number, but do not perform a deeper analysis. Preliminary CFD simulations[25] also showed asymmetric behavior in a three-dimensional model, for high Eötvös number and low Morton number. Axisymmetric behavior is still observed for intermediate viscosity ratios. Comparison between two-dimensional and three-dimensional simulation also shows that forcing axisymmetry (two-dimensional model) leads to wrong Froude number results[25].

When asymmetric behavior happens, drop shape oscillations are observed.

The aim of the present work is to obtain data about the flow of a single Taylor drop in a stagnant heavier liquid in a long vertical tube and analyze the occurrence of deviations to the axisymmetric behavior. This work follows a previous one[25], where asymmetries were detected. Computational Fluid Dynamics (CFD) tools were applied to a long enough vertical tube in a three-dimensional model. CFD is an attractive choice because with it one can easily change the operating conditions, geometry or fluid properties. Moreover, CFD is also an easy tool to obtain relevant information, such as velocity field, streamlines and pressure gradients. The numerical data obtained were validated through experimental data.

In the present work, the conditions considered lie in the ranges: $0.01 < \mu^* < 100$, $8 < \mathrm{Eo} < 30$, $2.32 \times 10^{-6} < \mathrm{M} < 100$ and $\rho^* = 0.792$ (unless otherwise stated) for two immiscible liquids. Concerning drop size, simulations were done using $d_\mathrm{S}/D = 1.12$ and 1.40. Simulations were performed in Ansys Fluent (releases 15 and 16) in transient mode and assuming laminar regime and incompressible flow.

The present work contains firstly an overview on the theory and numerical models used, as well as the numerical model validation with experimental data. Afterwards, simulation results are presented concerning the influence of relevant dimensionless numbers.

4.2 Methods

4.2.1 Experimental setup and procedure

Experimental setup for determining drop terminal velocity and observing drop shape is shown in Figure 4.1. It consists of a 4 m long vertical acrylic column with an internal diameter of 21 mm. An open reservoir is connected to the top end of the testing column. The column and the reservoir are filled with the continuous phase.

The dispersed phase drop is injected in the column using a pre-chamber. The connection between the pre-chamber and the column is possible through a spring and level plug.

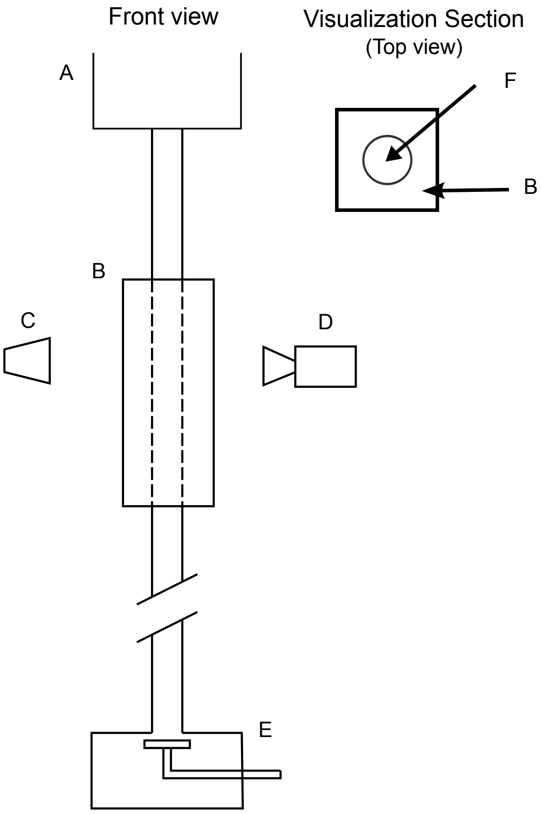

Figure 4.1: Experimental apparatus (A – top reservoir, B – visualization box, C – light source, D – Camera, E – injection pre-chamber, F – tube).

The visualization section is located near the top of the column. Its location, far enough from the injection point, ensures the drop reaches the terminal velocity (such condition is confirmed by analyzing the captured images). This section consists of an acrylic box with rectangular faces wrapping the tube and filled with continuous phase liquid to reduce optical distortion. A camera is positioned in front of the box. At the other side a strong source provides light to the scene.

Drops are injected one at a time, and rise in the continuous (more dense) phase until reaching the surface at the collection reservoir. Images are taken at a rate of 25 s^{-1}. They are then processed by a computer code. Prior to any experiment, the distances in the captured image are calibrated.

Three different systems were tested (Table 4.1): air bubble in water continuous phase, lubricant oil drop in water and lubricant oil in glycerin aqueous solution (refer to the Results section for the Froude number results). Air in water is outside the scope of the present work, but such experiment serves as validation of the experimental procedure (Table 4.2 for comparison with literature[13,26]).

4.2.2 Numerical model

The numerical domain is represented in Figure 4.2. Three main regions are distinguishable in a Taylor drop : the nose (I), the drop body (II) and the rear (III). The nose shape is closely related to the drop velocity. Around the body of an axisymmetric drop, a thin fully developed continuous phase film is observed. The third main region is the bottom of the drop. The drop shape and possible oscillations have a significant influence in the continuous phase below.

In Figure 4.2, L_1, L_2, L_3, L_4 and L_5 represent planes perpendicular to the tube axis, where flow data

Table 4.1: Experimental conditions.

	air in water	oil in water	oil in aq. glycerin solution
ρ_C / kg m^{-3}	998	998	1170
μ_C / Pa s	0.001	0.001	0.0162
σ / N m^{-1}	0.072	0.0192	0.0194
ρ^*	0.0012	0.882	0.752
μ^*	0.018	283	17.5
Eo	60	26.6	64.6
M	2.66×10^{-11}	1.66×10^{-10}	1.96×10^{-5}

Table 4.2: Air-water experimental result.

Fr (this work)	Fr (literature[13,26])
0.33	0.34

were collected for analysis.

The numerical model was described in a previous work[25] and is based in Navier-Stokes equations[27,28], containing four force terms: hydrostatic pressure, gravity, viscosity and surface tension. The liquids are incompressible and immiscible. In order to deal with the two-phase flow through Volume of Fluid method (VOF)[29], a variable α_i – volume fraction – is defined. The value of α_i is 1 at any point occupied exclusively by the fluid i, 0 if no i exists there, or a number between 0 and 1, if both fluids exist in the same mesh element:

$$\alpha_C + \alpha_D = 1. \tag{4.6}$$

In CFD computations, cells filled with both liquids ($0 < \alpha_i < 1$) do not represent fluid mixture (they are immiscible). In the present work, they represent the interface between the liquids. Density and viscosity are computed supposing linear contributions of each phase.

Transient simulations were performed with the commercial software Ansys Fluent (releases 15 and 16). A multiphase laminar incompressible flow model integrated with Volume of Fluid (VOF) method was used[29], simultaneously with geometric reconstruction method[30] – "Geo-reconstruct" in the software package – which determines the interface on a cell. Regarding pressure-velocity coupling, PISO[31] was used, a non-iterative algorithm which splits the solution into predictor and corrector steps. For pressure interpolations, a pressure staggering scheme was chosen[32] – "Presto!" in the software package. The QUICK[33] scheme was used for solving the momentum equation and the gradients of the scalars were computed by the Green-Gauss node-based method. The Continuum Surface Force model[34] was also employed. The interface between the two liquids was represented as a transition region of finite thickness where the surface tension force term is proportional to the curvature in each location. Outside the interface, this force term is zero.

The simulations were performed with a maximum Courant number of 0.25 and 10^{-4} as convergence criteria for the solution of continuity and velocity equations.

The domain consisted of a cylinder with a diameter D and height $10\,D$. The walls are solid and verify the no-slip condition. The two cylinder bases are inlet and outlet of continuous phase. The mesh was created in two steps. Firstly, a pattern with about 3800 elements was created in a 2D cross-section of the cylinder. Then, that pattern was replicated 1000 times by extrusion. A denser grid (increased element density in the base cross-section) was also tested, but the results were the same (Table 4.3).

Simulations were initialized with an isolated drop consisting of the merge of two shapes: a hemisphere

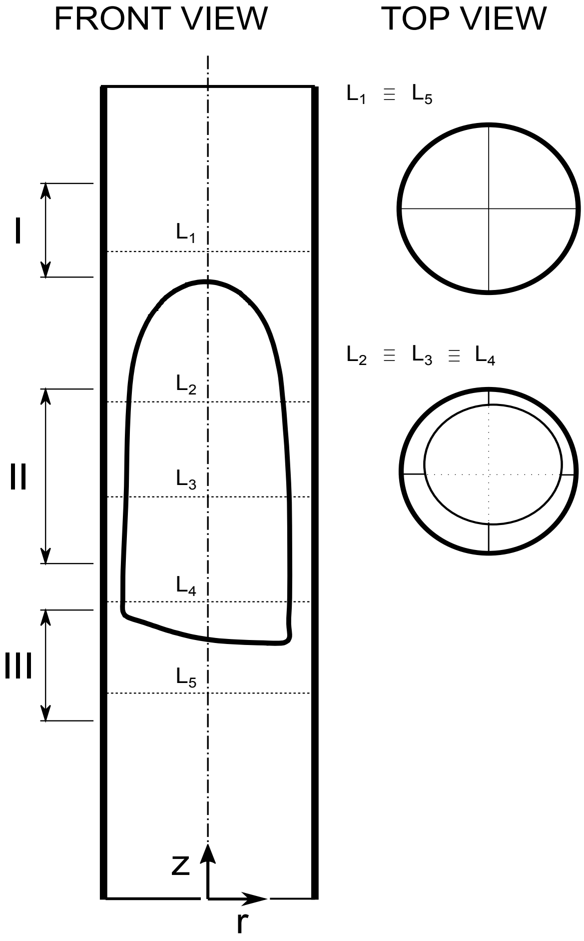

Figure 4.2: Representation of the numerical domain.

Table 4.3: Grid independence tests (base: 3.8 million elements, denser: 5.3 million elements).

Eo	log M	μ^*	Grid	Fr
15.8	-5.6	0.041	base	0.225
			denser	0.220
22	-5.6	20	base	0.164
			denser	0.162

for the drop nose region and a cylinder (with a diameter matching the one of the hemisphere). This initialization method is the three-dimensional analogous to the one described by Araújo et al.[35]. Note that during the simulation, the velocity field was analyzed to ensure the distance between the inlet and the drop was big enough to have undisturbed flow near the tube inlet.

A reference frame attached to the drop nose was used, following the procedure reported in a previous work[25]. In this reference frame, the drop is still and the continuous phase and the tube wall move downwards with a speed that equals the drop terminal velocity. Moreover, due to the relative motion created by the reference frame, an inlet flow boundary condition, with a downward uniform velocity (equal to $|V_\mathrm{T}|$) was imposed at the top of the domain. At the tube exit, pressure is set to zero gauge.

The final result for each condition is obtained by an iterative procedure. Firstly, a proper guess for inlet and wall velocities is imposed, and a first simulation is run. Afterwards, the drop velocity is determined, and imposed velocities in wall and inlet regions are adjusted. This process repeats until the drop stands still. Simulation is, then, run again in order to obtain the relevant flow data. At the end of the simulation, drop volume is checked to ensure it was not affected by any numerical error.

4.2.3 Symmetry parameter

In the present work, asymmetry assessment is one of the main goals. Quantification of asymmetries is not straightforward though. An intuitive choice is to investigate how the film thickness changes when analyzing a plane cut perpendicular to the tube axis. However, this choice does not provide coherence because when studying the region above the drop, it makes no sense to talk about “film”. Thus another procedure was chosen. Consider an hypothetical horizontal slice of the domain. On that slice, one can draw two perpendicular lines (refer to Figure 4.2) corresponding to two diameters (or four radii). Velocity profile can then be analyzed along each one of the four segments. On each one, the maximum vertical velocity component ($v_{\mathrm{p}i}$) is registered and the mean maximum velocity ($\overline{v_\mathrm{p}}$) is computed. The parameter of symmetry that arises from this procedure is then defined as:

$$S_{v_\mathrm{p}} = \sum_{i=1}^{4} \left(\frac{v_{\mathrm{p}i} - \overline{v_\mathrm{p}}}{\overline{v_\mathrm{p}}} \right)^2 . \tag{4.7}$$

A case where $S_{v_\mathrm{p}} = 0$ is perfectly symmetrical.

4.3 Results

An example of a simulated drop is presented in Figure 4.3, showing shape and flow asymmetry. Closer to the drop nose, the flow velocity is increased in the downwards near the wall and upwards near the center. Around an axisymmetric drop a stabilized film of continuous phase is observed. Unlike gas-liquid, in liquid-liquid the maximum velocity is located in the film, not in the interface. If drop viscosity is high enough, upward velocities can be observed near the interface[25]. With asymmetric effects (such as Figure 4.3), such stable film cannot be observed and oscillations in continuous phase thickness appear. An oscillation along the drop body also causes a change in the velocity profile of the continuous phase. The flow close to the drop rear will also be disturbed by the drop. At locations far below the drop, the continuous phase flow is uniform.

The following subsections discuss the behavior above and below the drop, and the drop region itself. Relevant comparisons are done for selected groups of simulations ($0.01 < \mu^* < 100$, $8 < \mathrm{Eo} < 30$, $2.32 \times 10^{-6} < \mathrm{M} < 100$), concerning drop shapes and behavior in the continuous phase. The need for

Figure 4.3: Drop and velocity field (drop nose reference frame) for Eo = 22, M = 100 and $\mu^* = 10$.

three-dimensional simulations as opposed to axisymmetric 2D is discussed. Thus, the first subsection discusses the terminal velocity. It is followed by the analysis on the region above the drop, then the region around the drop and, finally, the region bellow the drop.

Unless otherwise stated, density ratio should be considered as 0.792. Note that Hayashi et al.[11] showed that the density ratio does not influence Froude number (as discussed earlier). Nevertheless, Hayashi et al.[11] used values between 0.74 and 0.81 in their experiments and Mandal et al.[20] values between 0.65 and 0.87. A density ratio of 0.792 is thus inside the typical values for this kind of studies.

Concerning $d_S/D = 1.12$, a summary of drop shapes is presented in Figure 4.4. Contours on the image correspond to a vertical plane containing the tube axis. Two images at different instants are provided for the cases where shape asymmetries are observed. For the ranges presented, low Eötvös number has a stabilization effect. Drops are symmetrical showing similar shapes, and are distinguishable for their rounded bulky rear region – high surface tension forces. At Eötvös number equal to 22, drops are more elongated. Furthermore, at Eötvös number equal to 22 asymmetry starts to appear. Notice however

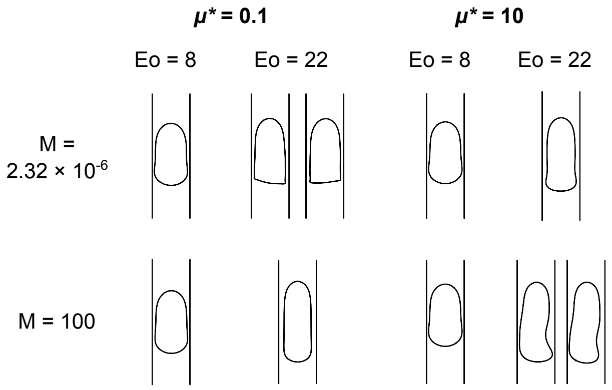

Figure 4.4: Summary of drop shapes.

that two different kinds of effects are observable. For Morton number equal to 2.32×10^{-6}, in the range presented, asymmetric effects appear for low viscosity ratios and consist mainly of oscillations in the lower part of the drop. This oscillation is associated with slow transport of momentum by diffusion both in the dispersed and continuous phases, which is a characteristic of low Monton numbers, low viscosity ratios and high Eötvös numbers. On the other hand, for Morton number equal to 100, asymmetry happens for high viscosity ratios. Here, a serpentine movement along the whole drop body is observed. The serpentine movement is associated with fast transport of momentum by diffusion inside the drop and slow transport of momentum by diffusion outside the drop characteristic of high viscosity ratios.

Figure 4.5 presents the vertical velocity (normalized) for three simulations. Locations L_1, L_2, L_4 and L_5 correspond to slices perpendicular to the tube axis (refer to Figure 4.2). Two columns at different instants are provided for the cases where shape asymmetries are observed (low and high viscosity ratio). For the simulation with $\mu^* = 3$, the slices show perfect symmetry in the velocity. Above the drop (L_1), velocity is smaller than in the other locations. Continuous phase velocity is higher in the drop region (L_2 and L_4) as the area is smaller. Below the drop (L_5), a disturbance in the flow is observed as well. A different representation of the same simulations in L_2 location is presented in Figure 4.6. Velocity vectors are projected into the tube cross section ($v_{\text{horizontal}}$) and are represented as vector arrows. The color refers to the ratio between the magnitude of this projection and the velocity. These examples are, once more, representative of the three main behaviors observed. On the left, the drop for low viscosity (a drop with a small asymmetric behavior) shows relevant fluid circulations inside the drop. In the middle, the symmetric case has irrelevant horizontal velocities. For the higher viscosity ratio (right column), the drop has relevant shape oscillations. Because of that, two different instants can have large differences. In the first, there is some observable horizontal flow, while in the other, preceding the oscillation, a strong horizontal flow, in the direction of the fluids interface, is observable.

Low interfacial forces is the main driving for the appearance of asymmetries.

In conditions of high viscosity of both liquids (large viscosity ratio and large Morton number), and hence high shear stresses at the interface, and low surface tension (higher Eötvös number), small perturbations cause an imbalance of forces at the interface (particularly in the cylindrical body where the interface has a high radius of curvature). This imbalance can only be restored at the expense of an increase in the pressure difference between both sides of the interface. This increase must be done at the expense of a decrease in the radius of curvature. This decrease causes distortion and the undulating shape of the drop in the region of the cylindrical body. Since the surface tension is small, the time to restore the perturbations is too high and the interface undulates permanently.

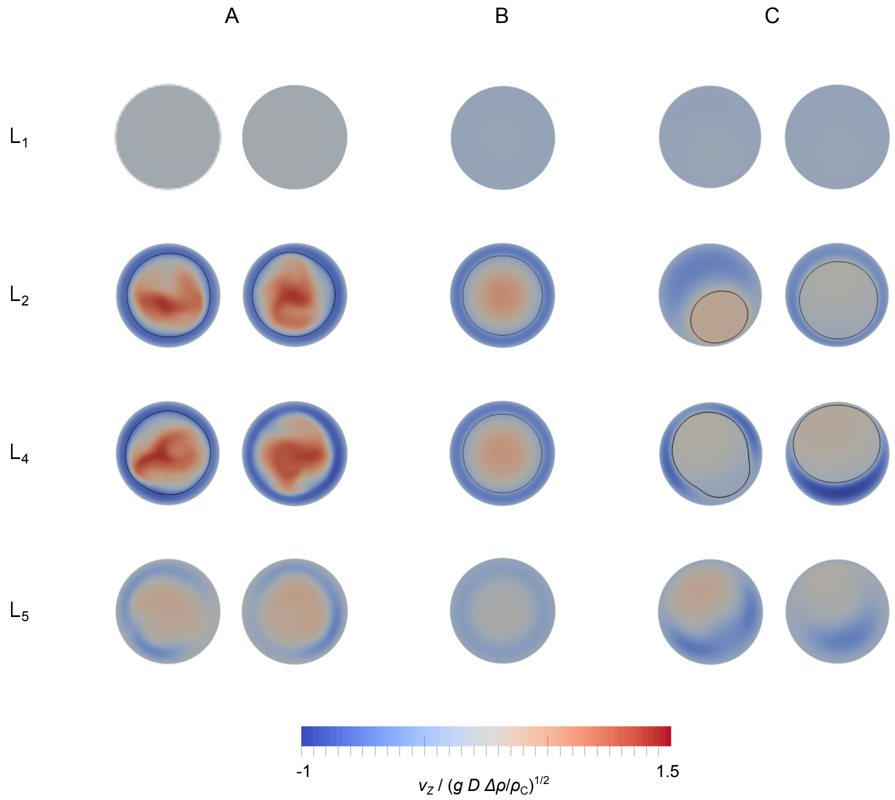

Figure 4.5: Velocity magnitude (normalized) for three simulations with M = 2.32×10^{-6} and Eo = 30 (A – $\mu^* = 0.3$, B – $\mu^* = 3$, C – $\mu^* = 41$).

In conditions of low viscosity of both liquids (low viscosity ratio and low Morton number implies low viscosity of both fluids and high Froude number), the drop has an elongated shape and a flat bottom with a large radius of curvature. A low surface tension combined with a flat surface leads to a small pressure difference between both sides of the interface. This situation is unstable since small perturbations lead to a significant increase of the pressure difference. Under low viscosity conditions (slow momentum diffusion and large velocities in both phases) equilibrium can only be restored through changes in the shape of the drop bottom. Periodic oscillations of the drop bottom imply a periodic change in the direction of the forces at the interface inclusive of the shear stress forces.

Figure 4.7 shows snapshots of two experiments conducted in the present work (refer to Table 4.1 for experimental conditions). Images of the corresponding simulations are provided as well. In the examples provided, drop size in experiments and simulations is different. This does not influence the terminal velocity nor the oscillating phenomena.

Concerning the oil in water experiment, an elongated drop with an oscillating nose and a wave-like effect was observed. A similar pattern was obtained in the simulation. Note also a slightly bulkier bottom region observable in the simulation image as well as in the 0.4 s and 0.8 s images obtained experimentally. In the first image, such shape is not clear due to a large oscillation at that instant.

A serpentine effect is clearly obtained with the oil in glycerin solution (see Table 4.1 for details on the glycerin solution). Note the detail of shadow in the middle of the drop which appears in both simulation and experiment (0.16 s).

Highly asymmetric behavior in such experiments (high viscosity ratios) supports the trends observable in Figures 4.4 and 4.5.

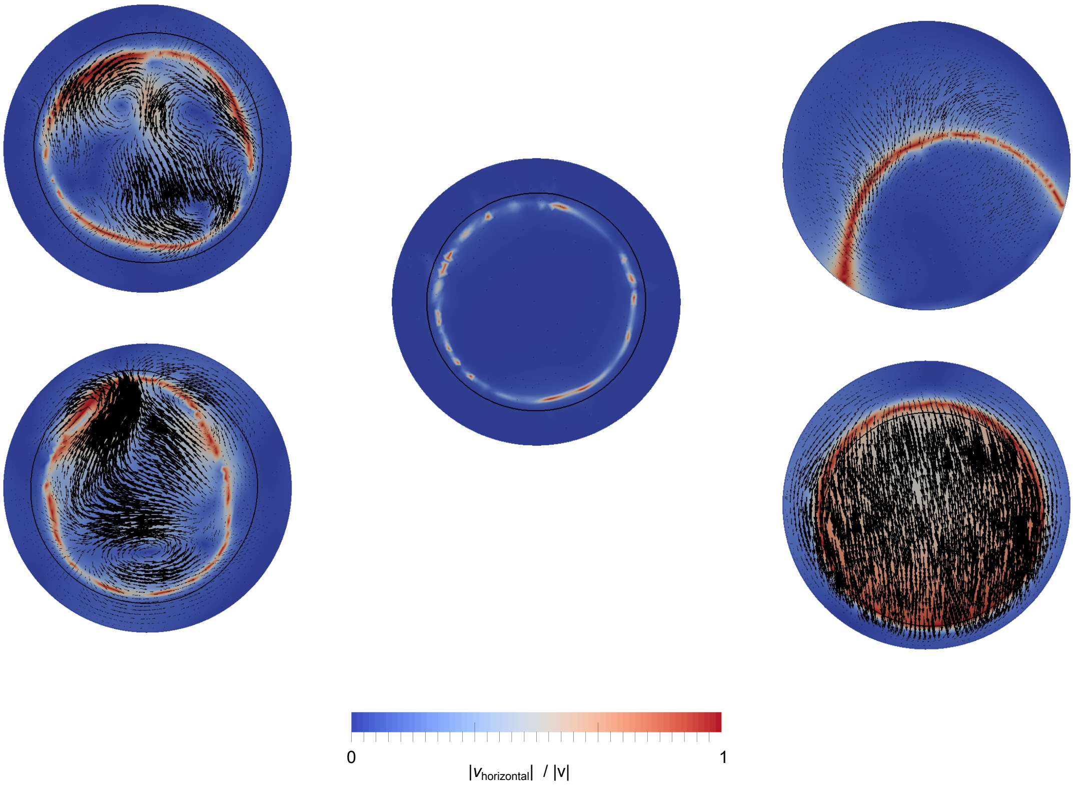

Figure 4.6: Cross-cut $1D$ below the drop nose for three simulations with $\mathrm{M} = 2.32 \times 10^{-6}$ and $\mathrm{Eo} = 30$ (left – $\mu^* = 0.3$, middle – $\mu^* = 3$, right – $\mu^* = 41$) – vectors for velocity horizontal component and color contours for the ratio of magnitudes between horizontal component and velocity vector.

Table 4.4: Numerical and experimental Froude number (D – this work, H – Hayashi et al.[11]).

Eo	M	μ^*	source	Fr exp.	Fr num.
30	2.0×10^{-5}	1.1	H	0.29	0.30
13.3	4.0×10^{-1}	0.017	H	0.027	0.024
92.6	3.5×10^{-1}	0.11	H	0.24	0.25
9.4	1.3×10^{-5}	0.37	H	0.075	0.082
26.6	1.7×10^{-10}	283	D	0.25	0.25
64.4	2.0×10^{-5}	17.5	D	0.24	0.21

Table 4.5: Influence of drop size in Froude number.

Eo	log M	μ^*	d_S/D	Fr	Deviation
8	-5.6	10	1.12	0.0254	6.7 %
			1.40	0.0238	
15.8	-5.6	0.041	1.12	0.225	2.3 %
			1.40	0.220	
22	-5.6	0.01	1.12	0.262	0 %
			1.40	0.262	
22	-5.6	0.1	1.12	0.277	2.6 %
			1.40	0.270	
22	-5.6	20	1.12	0.164	1.2 %
			1.40	0.162	
22	2	10	1.12	0.00350	-4.1 %
			1.40	0.00365	
30	2	0.3	1.12	0.321	-1.8 %
			1.40	0.327	

These experiments as well as literature data[20,11] were used as validation of the numerical method by comparing Froude number results. Table 4.4 presents conditions and Froude number values for simulations and experiments – in the "source" column, "D" stands for this work and "H" for Hayashi et al.[11]. The present numerical model shows good agreement in a wide range of dimensionless numbers.

4.3.1 Terminal velocity

The present study starts by evaluating the drop size influence on the terminal velocity (Table 4.5). Under the studied conditions, drop size does not appear to be an important parameter. Density ratio was also studied. Table 4.6 presents no significant differences, as already reported in literature[11].

Figure 4.8 presents the terminal velocity results, through the corresponding dimensionless entity, the Froude number (equation 4.1). These results follow the trends already published in the literature[25,11]. Froude number increases with increasing Eötvös number, corresponding to a decreased influence of surface tension forces and/or an increase of the gravity effects (large difference between the density of both liquids). If the increase of the Eötvös number is accomplished by a decrease of the Morton number, i.e. a decrease of the viscosity of the continuous phase, and by a decrease of the viscosity ratio, i.e. a very low

Table 4.6: Influence of density ratio in Froude number.

Eo	log M	μ^*	ρ^*	Fr	Deviation
8	-5.6	10	0.792	0.0254	-15 %
			0.0792	0.0301	
15.8	-5.6	0.041	0.792	0.225	2.2 %
			0.001	0.230	

oil in water

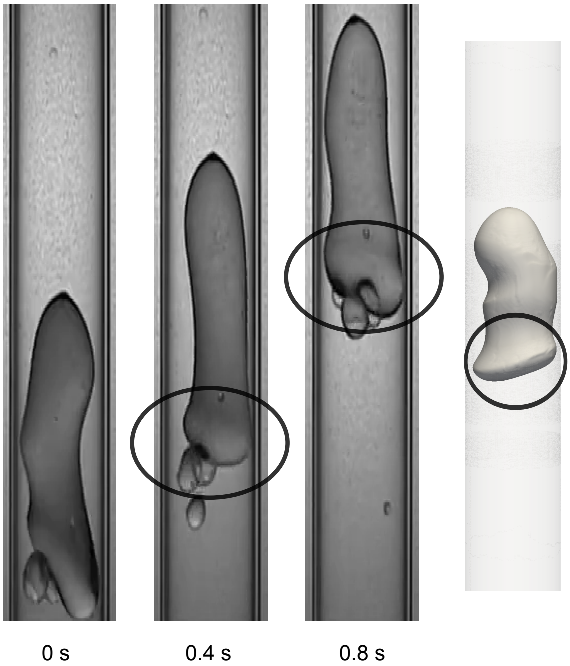

oil in glycerin sol.

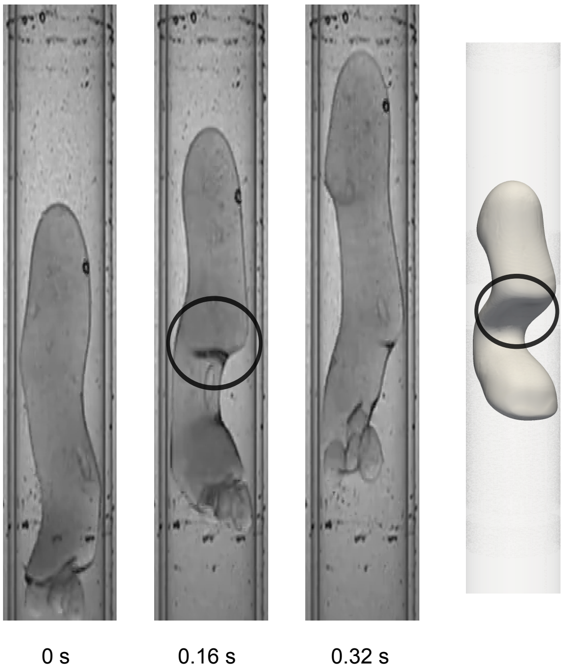

Figure 4.7: Experimental snapshots and corresponding simulations (oil in water – $\mu^* = 283$, Eo = 26.6, M = 1.66×10^{-10}; oil in glycerin – $\mu^* = 17.5$, Eo = 64.6, M = 1.96×10^{-5}).

viscosity of the dispersed phase, the Froude number reaches the highest values. These results are close to the known Froude number limit of 0.35 for a gas Taylor bubble rising in a low viscous fluid.

On the other hand, Froude number decreases with decreasing Eötvös number. This decrease can be attained by decreasing the difference between the density of both fluids (liquid drop rising in another liquid) or by increasing the capillary effects (gas-liquid flow in a capillary). So, in the limit, and for defined values of Morton number and viscosity ratio, the flow characteristics of a drop in a continuous liquid, here in study, should be comparable to those of the flow of a Taylor gas bubble in a liquid in a capillary.

Figure 4.9 presents the relative deviation between Froude number from a 2D axisymmetric model ($\mathrm{Fr}_{2\mathrm{D}}$) and that obtained with the 3D model ($\mathrm{Fr}_{3\mathrm{D}}$) developed in the present work. For the comparison, 2D results were obtained by the numerical model explained by Direito et al.[25]. Simulations were also performed for lower viscosity ratios in the Eötvös 22 and Eötvös 30 series, but the 2D model was not able to reproduce stable drops and the results are not shown. Significant differences in Froude number between 2D and 3D occur for lower viscosity ratios, except for Eötvös number of 8, whose deviations are always less than 10 %. For Eötvös number of 22, Figure 4.9, results show again higher deviations for lower viscosity ratios. Taking into account these observations and the results presented in Figure 4.8, axisymmetric model fails to predict drop terminal velocity when Froude number value goes above about 0.25.

Interestingly, the drops in the 10-100 viscosity ratio range tend to show asymmetric behavior (both in shape and in the continuous phase velocity), while still being able to yield a correct drop velocity (Froude similar to the corresponding simulations in 3D).

4.3.2 Region above the drop

At the drop nose, the continuous phase assumes a velocity that equals V_T: it is being pushed by the drop. Going farther from the nose, velocity will decrease until the continuous phase is stagnant, without any influence from the drop presence. One strategy to evaluate such influence is to measure the distance needed for the vertical velocity component in the tube axis to be below a defined criterion. Figure 4.10 shows the influence distance divided by the diameter ("Z_I", where "I" refers to the label in Figure 4.2) in the axis above the drop, measured when the vertical component in continuous phase has dropped below 5 % of V_T. The time average value is presented. Interestingly, even though a wide range of conditions is presented, the influence distance stays bounded between $0.4D$ and $0.6D$. Influence distance shows little sensitivity to Eötvös and Morton numbers. Viscosity ratio appears to have the most relevant effect on this parameter.

Following these results and in order to analyze how the different conditions cause asymmetries in the flow above the drop, a distance of $0.25\,D$ was set to apply the analysis based on equation 4.7, as explained before (L_1 in Figure 4.2). Figure 4.11 presents such results with time-averaged values (lines are taken at constant angular location). Figure 4.11 also presents the drop shapes from some simulations. Two images are provided for the conditions where shape is time dependent. Low Eötvös number simulations show no significant asymmetric effects. In other ranges of Eötvös number, simulations seem to have three distinct behaviors. For low viscosity ratios, they show mild asymmetric behavior. For medium viscosity ratios, the drops are axisymmetric. Finally, for higher viscosity ratios, significant asymmetric effects occur. In coherence with Figure 4.4, it is possible to distinguish an axisymmetric behavior for medium viscosity ratios, rear asymmetric behavior for low viscosity ratios and a serpentine movement for high viscosity ratios. The asymmetry magnitude and the shape behavior are closely related. Almost null asymmetry

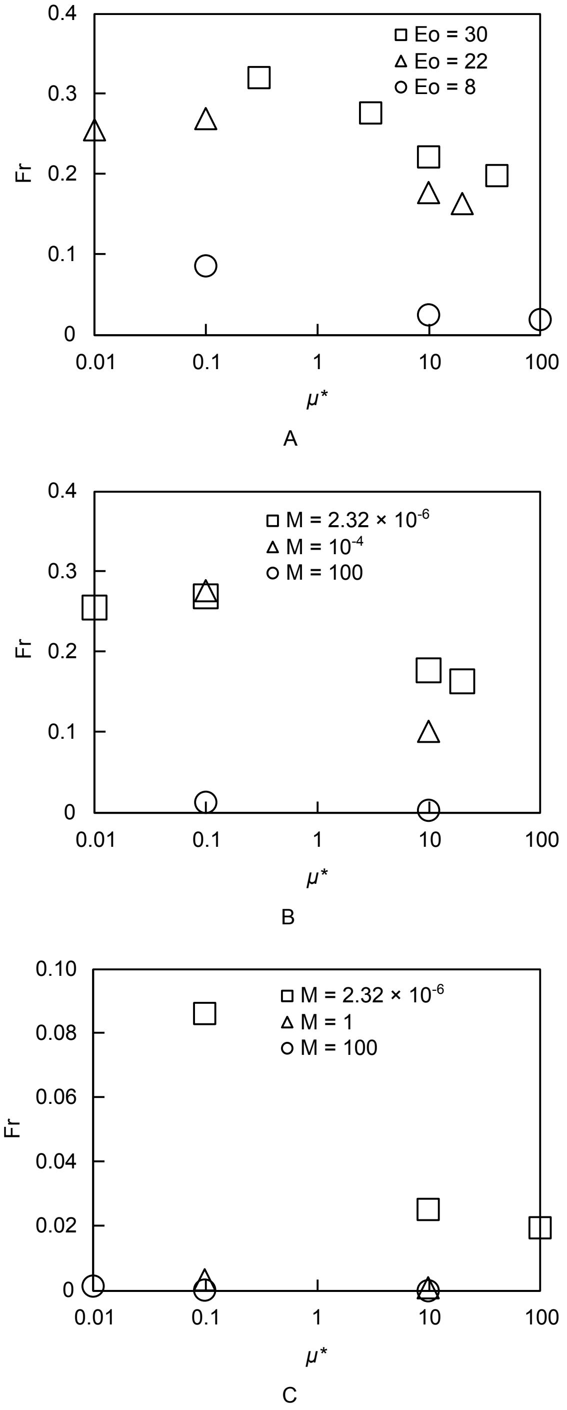

Figure 4.8: Froude number as function of viscosity ratio (A – M = 2.32×10^{-6}, B – Eo = 22, C – Eo = 8).

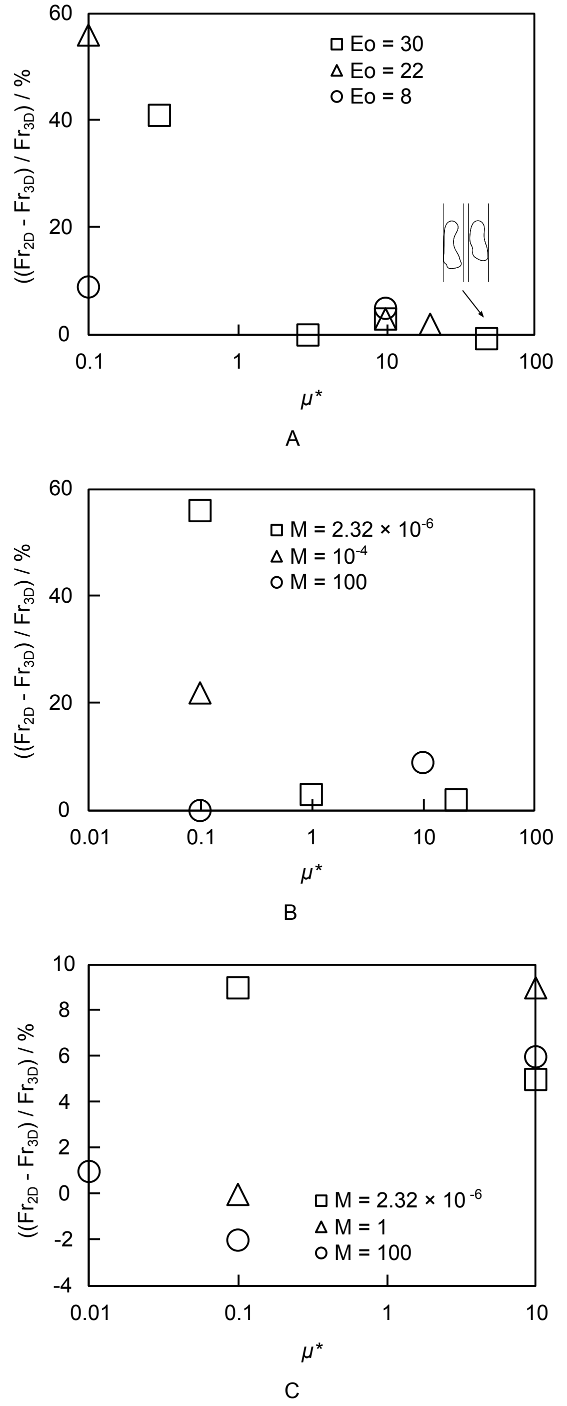

Figure 4.9: Deviation of 2D Froude results as function of viscosity ratio (A – M $= 2.32 \times 10^{-6}$, B – Eo = 22, C – Eo = 8).

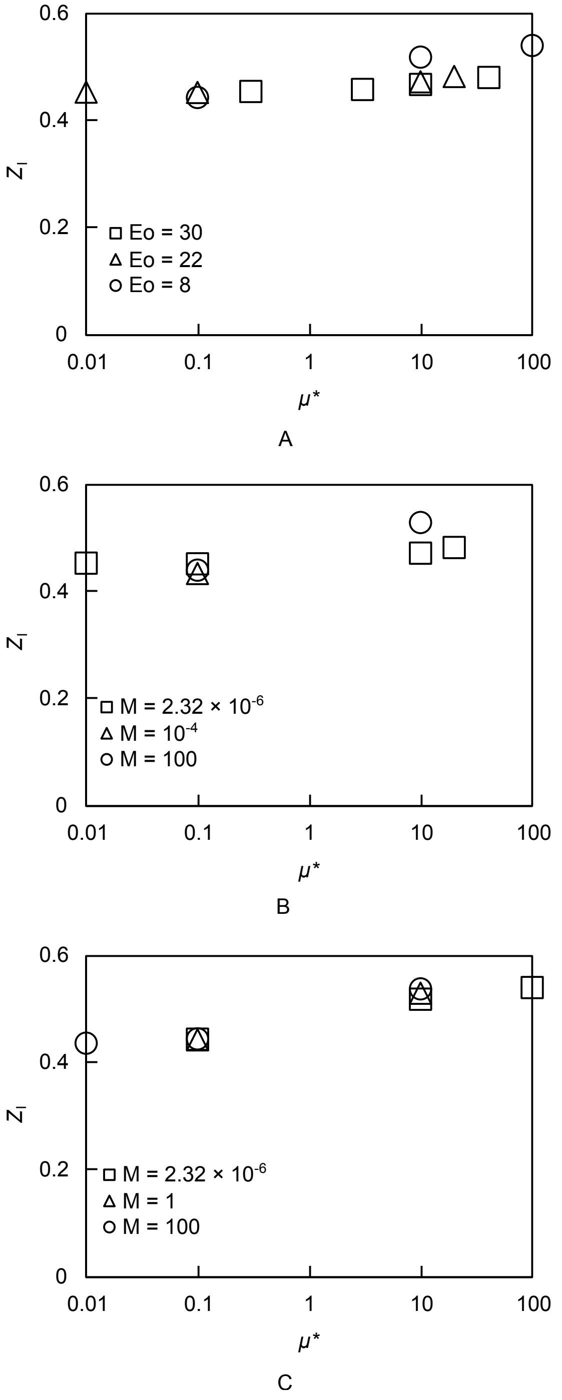

Figure 4.10: Influence distance above nose for 5 % criterion (A – M = 2.32 × 10^{-6}, B – Eo = 22, C – Eo = 8).

Table 4.7: Drop size and the symmetry parameter above the drop.

Eo	$\log \mathrm{M}$	μ^*	d_S/D	S_{v_p}
15.8	-5.6	0.041	1.12	0.71
			1.40	0.26
22	-5.6	0.1	1.12	1.1
			1.40	0.26
22	-5.6	20	1.12	1.7
			1.40	0.22
22	2	10	1.12	3.4
			1.40	0.36
30	-5.6	0.3	1.12	1.1
			1.40	0.40

magnitude corresponds to axisymmetric behavior. Strong asymmetric effects are observed, both in shape and in the flow above the drop, for high viscosity ratios. In fact, taking continuity into account, it is no surprise that the serpentine effect causes high asymmetries in the continuous phase velocity profiles. For the low viscosity ratio region, a mild value for the symmetry parameter corresponds to milder shape effects, mainly in the drop rear, when compared to the high viscosity ratio region.

Increasing the drop size (Table 4.7), the symmetry parameter tends to a lower value (less asymmetric effects). Interestingly, the influence distance does not have significant changes (and the results are omitted).

4.3.3 Region around the drop

Consider the plane cut perpendicular to the tube axis at a distance of $1\,D$ below the drop nose (L_2 in Figure 4.2). The analysis based on equation 4.7 was applied here as well (Figure 4.12). For low Eötvös number, almost no asymmetry is found. Concerning low Morton and high Eötvös, asymmetric effects related to the serpentine movement of the drops are observed. The mild asymmetries found in the flow above the drop for low viscosity ratios do not show up here.

At a distance of $1.5\,D$ below the drop nose (L_3 in Figure 4.2), similar trends are found, though with higher values of the symmetry parameter (Figure 4.13).

4.3.4 Region below the drop

Following the same strategy, Figure 4.14 shows the influence distances below the drops ("Z_III"). Higher Eötvös show in general influence distances of at least $0.5\,D$ and up to $4\,D$. Interestingly, it is not possible to perceive a trend of increase or decrease in such results. For lower Eötvös, the distance seems bounded between 0.3 and $0.5\,D$. Following these results, at lower Eötvös number, coalescence of two drop is unlikely to happen unless they are close to each other. Conversely, at Eötvös numbers as high as 30, influence distances show that the drops are more prone to coalescence.

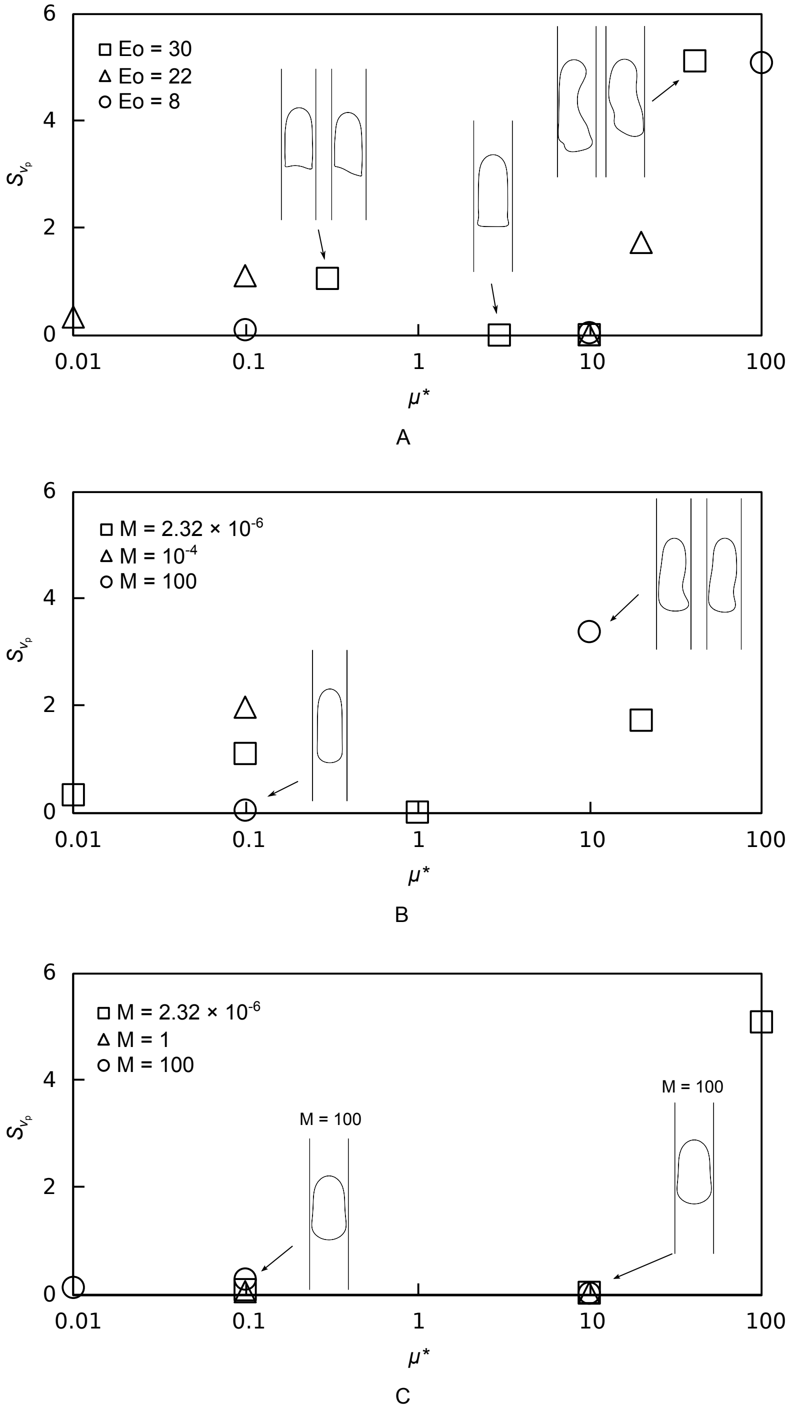

Figure 4.11: Symmetry parameter in 0.25 D above drop (A – $M = 2.32\times10^{-6}$, B – $Eo = 22$, C – $Eo = 8$).

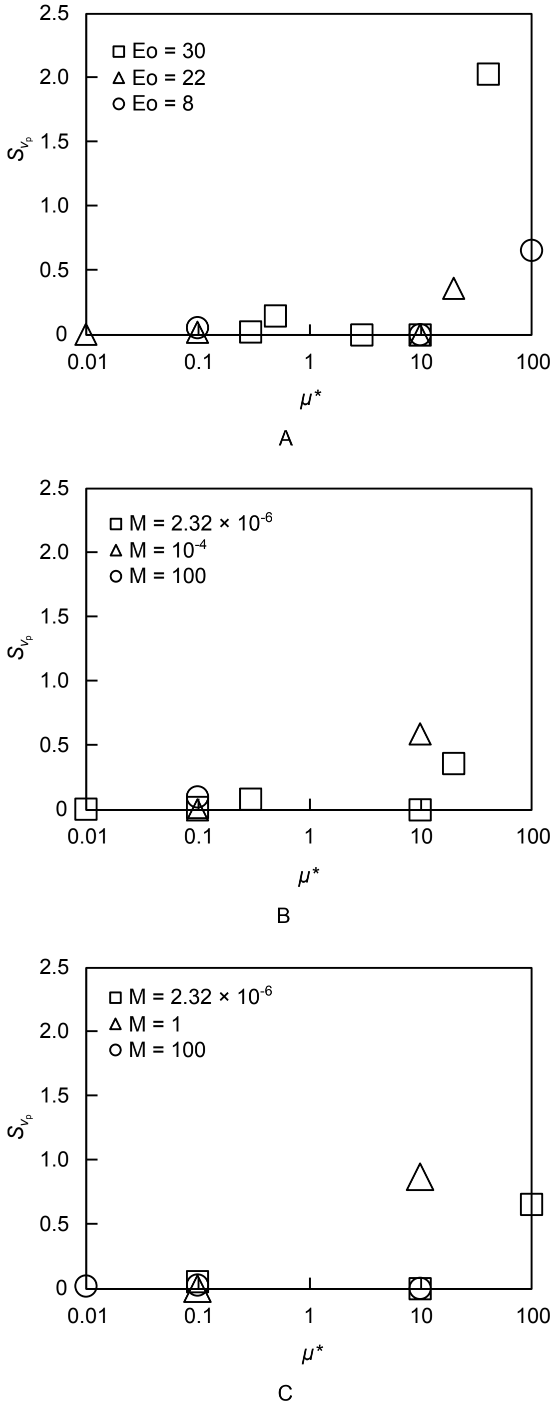

Figure 4.12: Symmetry parameter in 1 D below the drop nose (A – M = 2.32×10^{-6}, B – Eo = 22, C – Eo = 8).

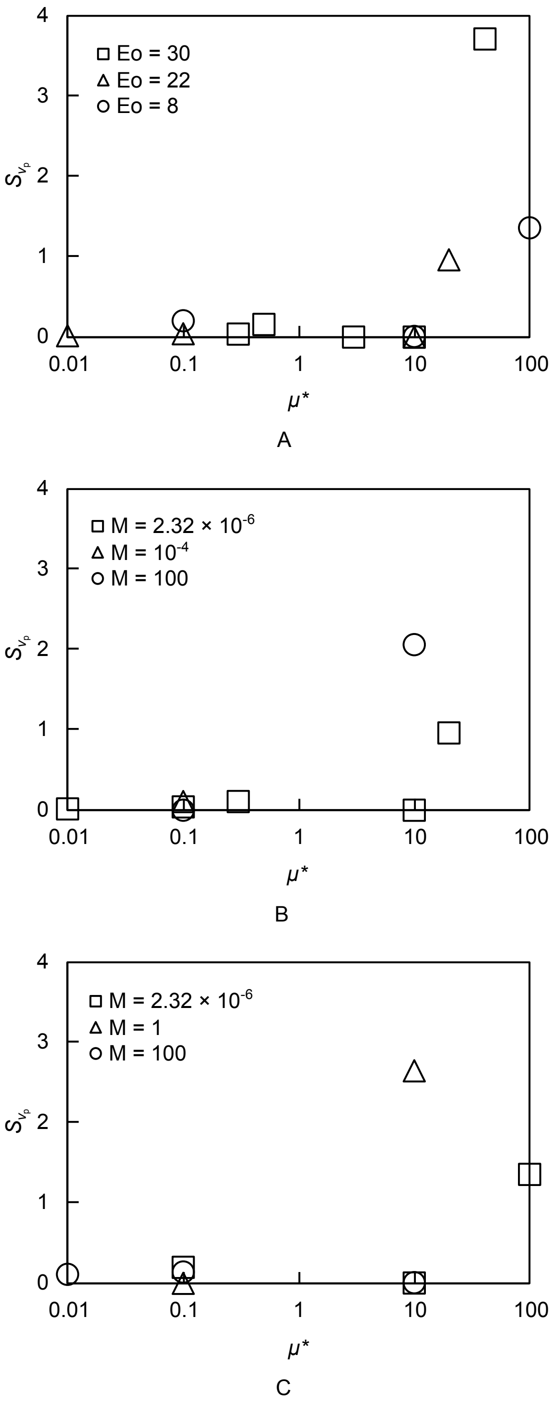

Figure 4.13: Symmetry parameter in 1.5 D below the drop nose (A – M = 2.32×10^{-6}, B – Eo = 22, C – Eo = 8).

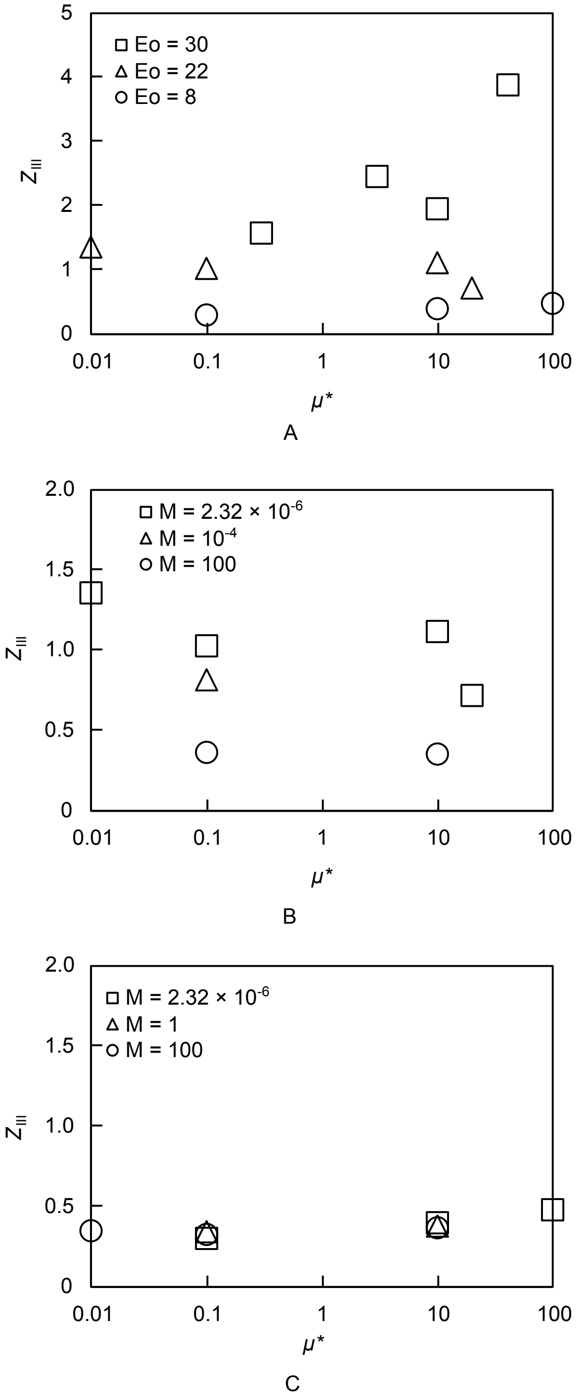

Figure 4.14: Influence distance below for 5 % criterion (A – M = 2.32×10^{-6}, B – Eo = 22, C – Eo = 8).

4.4 Conclusions

The importance of individual Taylor drops rising in a stagnant heavier liquid and the 3D effects on some drops motivated the present work.

A numerical study concerning single liquid Taylor drops rising at constant velocity in a stagnant heavier liquid is reported. CFD simulations were performed in a three-dimensional domain using Ansys Fluent (releases 15 and 16). From simulation data, it was possible to extract information on drop shape and velocity. The numerical model was validated by lab experiments for an extensive range.

Information on drop terminal velocity was collected and, therefore, it was possible to relate the Froude number with other dimensionless parameters. The general trends concerning the influence of Eötvös number, Morton number and viscosity ratio in the Froude number are consistent with previous works published in the literature. Furthermore, for the range studied, no violation of the 0.35 Froude limit was observed.

The influence distance for the continuous phase above the drop (concerning the 5 % of V_T criteria) is only slightly sensible to dimensionless number changes, staying bounded between 0.4 and 0.6 diameters. For the distance below the drop, an analogous behavior is found, though with more dispersed results.

High influence of interfacial tension forces (low Eötvös number) causes low Froude numbers. In such conditions, drops are symmetric and consistent in shape (rounded in the rear region). Higher Eötvös numbers tend to elongate the drops, as well as increase the Froude number. Asymmetries also start to be observed.

Concerning shape asymmetries (occuring when interfacial tension forces are not determinant), three ranges of viscosity ratio are distinguishable. Lower viscosity ratios lead to oscillating drop rears and low asymmetries in the flow above the drop, while showing significant horizontal flow inside the drop. For an intermediate range, drops show axisymmetric behavior. Finally, for the higher viscosity ratio region, drops show a significant asymmetric serpentine like movement.

The combination of low interfacial force and high viscosity of both liquids leads to oscillations in the drop body. These are related to the imbalance caused by small perturbations at the interface. An analogous behavior happens in the drop bottom due to the decreased interfacial tension forces combined, this time, with low viscosity of the liquids.

Froude number results are compared to data of a 2D axisymmetric model showing that this model cannot predict well higher Froude number cases (corresponding to low viscosity ratio and Morton number and high Eötvös number). The aforementioned horizontal flow inside the drop further supports these results. For drops with high viscosity ratio, the 2D model is able to output a correct Froude number, even though the drops, in 3D, are not axisymmetric.

The present work provides important data for a deeper understanding of Taylor drops and its asymmetries. It is, thus, an important step for a more general knowledge on liquid-liquid slug flow.

Acknowledgments

This work was funded by FEDER funds through the Operational Programme for Competitiveness Factors – COMPETE – and National Funds through FCT (Fundação para a Ciência e a Tecnologia) under the project PEst-OE/EME/UI0532. Filipe Direito gratefully acknowledge the financial support from the FCT through Ph.D. Grant SFRH/BD/79264/2011. The authors thank Professor Maria do Carmo Pereira and Dr. Joana Loureiro for the interfacial tension measurements.

References

[1] A.C. Bannwart, O.M.H. Rodriguez, F.E. Trevisan, F.F. Vieira, and C.H.M. de Carvalho. Experimental investigation on liquidliquidgas flow: Flow patterns and pressure-gradient. *Journal of Petroleum Science and Engineering*, 65(1-2):1–13, mar 2009. ISSN 09204105. doi: 10.1016/j.petrol.2008.12.014.

[2] Norman J Clark. *Elements of Petroleum Reservoirs (Henry L. Doherty series)*. Society of Petroleum Engineers of AIME, revised ed edition, 1969.

[3] R. M. Davies and G. Taylor. The Mechanics of Large Bubbles Rising through Extended Liquids and through Liquids in Tubes. *Proceedings of the Royal Society A: Mathematical, Physical and Engineering Sciences*, 200(1062):375–390, feb 1950. ISSN 1364-5021. doi: 10.1098/rspa.1950.0023.

[4] J Fabre and A Line. Modeling of 2-Phase Slug Flow. *Annual Review of Fluid Mechanics*, 24:21–46, 1992.

[5] W C Lyons and G J Plisga. *Standard handbook of petroleum and natural gas engineering*. Elsevier, 1999.

[6] J. Villarreal, D. Laverde, and C. Fuentes. Carbon-steel corrosion in multiphase slug flow and CO2. *Corrosion Science*, 48(9):2363–2379, sep 2006. ISSN 0010938X. doi: 10.1016/j.corsci.2005.09.003.

[7] Antonio C. Bannwart, Oscar M. H. Rodriguez, Carlos H. M. de Carvalho, Isabela S. Wang, and Rosa M. O. Vara. Flow Patterns in Heavy Crude Oil-Water Flow. *Journal of Energy Resources Technology*, 126(3):184, 2004. ISSN 01950738. doi: 10.1115/1.1789520.

[8] T.K. Mandal, G. Das, and P.K. Das. An appraisal of liquidliquid slug flow in different pipe orientations. *International Journal of Multiphase Flow*, 36(8):661–671, aug 2010. ISSN 03019322. doi: 10.1016/j.ijmultiphaseflow.2010.04.002.

[9] Adriane B S Serapião and Antonio C Bannwart. Knowledge Discovery for Classification of Three-Phase Vertical Flow Patterns of Heavy Oil from Pressure Drop and Flow Rate Data. *Journal of Petroleum Engineering*, 2013, 2013.

[10] PL Spedding, GS Woods, RS Raghunathan, and JK Watterson. Flow Pattern, Holdup and Pressure Drop in Vertical and Near Vertical Two-and Three-Phase Upflow. *Chemical Engineering Research and Design*, 78(3):404–418, 2000.

[11] K. Hayashi, R. Kurimoto, and A. Tomiyama. Terminal velocity of a Taylor drop in a vertical pipe. *International Journal of Multiphase Flow*, 37(3):241–251, apr 2011. ISSN 03019322. doi: 10.1016/j.ijmultiphaseflow.2010.10.008.

[12] E.T. White and R.H. Beardmore. The velocity of rise of single cylindrical air bubbles through liquids contained in vertical tubes. *Chemical Engineering Science*, 17(5):351–361, 1962. ISSN 00092509. doi: 10.1016/0009-2509(62)80036-0.

[13] J.D.P. Araújo, J.M. Miranda, A.M.F.R. Pinto, and J.B.L.M. Campos. Wide-ranging survey on the laminar flow of individual Taylor bubbles rising through stagnant Newtonian liquids. *International Journal of Multiphase Flow*, 43:131–148, jul 2012. ISSN 03019322. doi: 10.1016/j.ijmultiphaseflow.2012.03.007.

[14] Flavia Viana, Raimundo Pardo, Rodolfo Yánez, José L. Trallero, and Daniel D. Joseph. Universal correlation for the rise velocity of long gas bubbles in round pipes. *Journal of Fluid Mechanics*, 494: 379–398, nov 2003. ISSN 00221120. doi: 10.1017/S0022112003006165.

[15] RAS Brown and GW Govier. High-Speed Photography in the Study of Two-Phase Flow. *The Canadian Journal of Chemical Engineering*, 39:159–164, 1961.

[16] GW Govier, GA Sullivan, and RK Wood. The Upward Vertical Flow of Oil-Water Mixtures. *The Canadian Journal of Chemical Engineering*, 39:67–75, 1961.

[17] E. E. Zukoski. Influence of viscosity, surface tension, and inclination angle on motion of long bubbles in closed tubes. *Journal of Fluid Mechanics*, 25(04):821, 1966. ISSN 0022-1120. doi: 10.1017/S0022112066000442.

[18] T. K. Mandal, G. Das, and P. K. Das. Prediction of rise velocity of a liquid Taylor bubble in a vertical tube. *Physics of Fluids*, 19(12):128109, 2007. ISSN 10706631. doi: 10.1063/1.2824414.

[19] T.K. Mandal, G. Das, and P.K. Das. Motion of Taylor Bubbles and Taylor Drops in Liquid-Liquid Systems. *Industrial & Engineering Chemistry Research*, 47(18):7048–7057, 2008.

[20] T. K. Mandal, G. Das, and P. K. Das. Liquid Taylor Bubbles Rising in a Vertical Column of a Heavier Liquid: An Approximate Analysis. *Journal of Fluids Engineering*, 131(1):011303, 2009. ISSN 00982202. doi: 10.1115/1.3026730.

[21] R Clift, J R Grace, and M E Weber. *Bubbles, Drops and Particles.* Dover Publications Inc., New York, 2005.

[22] Daniel D. Joseph. Rise velocity of a spherical cap bubble. *Journal of Fluid Mechanics*, 488:213–223, jul 2003. ISSN 00221120. doi: 10.1017/S0022112003004968.

[23] Ryo Kurimoto, Kosuke Hayashi, and Akio Tomiyama. Terminal velocities of clean and fully-contaminated drops in vertical pipes. *International Journal of Multiphase Flow*, 49:8–23, mar 2013. ISSN 03019322. doi: 10.1016/j.ijmultiphaseflow.2012.08.001.

[24] Shaoping Quan and Jing Lou. Viscosity-ratio-based scaling for the rise velocity of a Taylor drop in a vertical tube. *Physical Review E*, 84(3):1–6, 2011. ISSN 1539-3755. doi: 10.1103/PhysRevE.84.036320.

[25] F. J. N. Direito, J. B. L. M. Campos, and J. M. Miranda. Rising of a single Taylor drop in a stagnant liquid – 2D laminar flow and axisymmetry limits. *Physics of Fluids*, 28(5):057101, 2016. ISSN 1070-6631. doi: 10.1063/1.4947426.

[26] A.O. Morgado, J.M. Miranda, J.D.P. Araújo, and J. B.L.M. Campos. Review on vertical gas-liquid slug flow. *International Journal of Multiphase Flow*, 85:348–368, 2016. ISSN 03019322. doi: 10.1016/j.ijmultiphaseflow.2016.07.002.

[27] João Moreira Campos. *Notas para o Estudo da Mecânica dos Fluidos.* FEUP edições, Porto, 1.a edição edition, 2013. ISBN 9789727521579.

[28] B R Munson, D F Young, and T H Okiishi. *Fundamentals of Fluid Mechanics.* John Wiley and Sons Ltd, 5th editio edition, 2005.

[29] C W Hirt and B D Nichols. Volume of Fluid (VOF) Method for the Dynamics of Free Boundaries. *Journal of Computational Physics*, 39:201–225, 1981.

[30] D L Youngs. Time-Dependent Multi-Material Flow with large Fluid Distorsion. In K. W. Morton and M. J. Baines, editors, *Numerical Methods in Fluid Dynamics*. Academic Press, 1982. ISBN 9780125083607.

[31] R. I. Issa. Solution of the implicitly discretised fluid flow equations by operator-splitting. *Journal of Computational Physics*, 62(1):40–65, 1986. ISSN 10902716. doi: 10.1016/0021-9991(86)90099-9.

[32] S V Patankar. *Numerical Heat Transfer And Fluid Flow*. Hemisphere, 1980. ISBN 0891165223.

[33] B. P. Leonard. A stable and accurate convective modelling procedure based on quadratic upstream interpolation. *Computer Methods in Applied Mechanics and Engineering*, 19(1):59–98, 1979. ISSN 00457825. doi: 10.1016/0045-7825(79)90034-3.

[34] J U Brackbill, D B Kothe, and C Zemach. A Continuum Method for modeling surface tension. *Journal of Computational Physics*, 100:335–354, 1992.

[35] J.D.P. Araújo, J.M. Miranda, and J.B.L.M. Campos. Simulation of slug flow systems under laminar regime: Hydrodynamics with individual and a pair of consecutive Taylor bubbles. *Journal of Petroleum Science and Engineering*, 111:1–14, nov 2013. ISSN 09204105. doi: 10.1016/j.petrol.2013.10.007.

5

A Taylor drop rising in a liquid co-current flow

Direito, F. J. N., Campos, J. B. L. M. and Miranda, J. M. (2017), 'A Taylor drop rising in a liquid co-current flow', *International Journal of Multiphase Flow* **96**, 134-143.

Abstract

The present work presents a numerical study on the behavior of isolated liquid Taylor drops rising in vertical tubes with co-current heavier continuous phase. Numerical simulations were performed with a previously validated model, implementing Volume of Fluid method in an axisymmetric geometry. Detailed flow patterns and drop shapes are provided and discussed for several conditions. The balance between gravity effect and velocity of the continuous phase flow was found to have a great influence in the flow patterns observed. The increase of inertial effects, due to the increase of Eo number and the co-current velocity, leads to the occurrence of closed recirculations below the drops. Furthermore, the continuous phase stabilization distance below the drop is a function of the drop Reynolds number. Drop and continuous phase velocities relationship was studied. A viscosity ratio related term was appended to a pre-existing correlation. The flow in the absence of gravity was also studied. Results demonstrate that micro-scale flow is a lower limit to the cases studied in the present work and suggest that the viscosity ratio affects mainly the inertial part of the drop velocity.

5.1 Introduction

The study of different kinds of multiphase flows is of high value due to their occurrence in chemical, nuclear or hydrocarbon industries, among others (Aziz et al., 2015, Bannwart et al., 2009, Babadagli, 2007, Omebereiyari et al., 2008, Seyfried and Freundt, 2000). One of the foremost multiphase patterns is slug flow. An example of this pattern can be observed when two immiscible liquids flow in a vertical tube, with the lighter one forming long bullet shaped drops (dispersed phase) surrounded by the heavier liquid that constitutes the continuous phase.

Earlier studies on slug flow concern gas-liquid systems Davies and Taylor (1950), Moissis and Griffith (1962), Nicklin et al. (1962), White and Beardmore (1962), Morgado et al. (2016). This can occur, for example, when the dispersed phase flow rate is increased at a point when small bubbles start to coalesce into those long bullet shaped (Araújo et al., 2012). Such bubbles are known as Taylor bubbles Davies and Taylor (1950). Because of the intermittent behavior of this flow pattern, operational problems can occur (Lyons and Plisga, 1999, Villarreal et al., 2006).

By analogy, drops in liquid-liquid slug flow are known as Taylor drops (Mandal et al., 2008). Liquid-liquid slug flow can be used, for instance, for the ability of lubricating the flow of a very viscous and wall-adherent dispersed phase. Liquid-liquid slug flow has recently sparked interest for its importance in oil wells (Bannwart et al., 2004, Mandal et al., 2010). Moreover, even three phase flow (gas-water-oil) can sometimes resemble two phase slug flow (Serapião and Bannwart, 2013, Spedding et al., 2000).

The aim of the present work is to obtain data about the flow of a single Taylor drop in a long vertical tube where a heavier liquid is flowing upwards. The data is obtained by conducting a series of Computational Fluid Dynamics (CFD) simulations, based on a validated two-dimensional axisymmetric model (Direito et al., 2016), using Ansys Fluent. Furthermore, the present study intends to find a relationship between the drop velocity and other flow parameters.

5.2 Theory and methods

Despite its importance, liquid-liquid slug flow is not well studied yet. In order to gain a deeper understanding, one must study all phenomena step by step. The simpler approach is to consider a single Taylor drop rising in a stagnant heavier liquid in a vertical tube. It is expected that a rising single Taylor drop reaches a constant terminal velocity (V_{T}). Some of the earlier studies include those of Brown and Govier (1961), Govier et al. (1961) and Zukoski (1966). Mandal et al. (2007, 2008, 2009) studied the shape and velocity of a drop rising in a quiescent liquid. Hayashi et al. (2011) presented experimental shapes and performed numerical simulations, evaluating the influence of several dimensionless numbers. A correlation to guess the terminal velocity was presented by Hayashi et al. (2011), Kurimoto et al. (2013). Direito et al. (2016) performed a numerical study to analyze velocity, shape and velocity profiles in the continuous phase and discussed, as well, the applicability of axisymmetry to such phenomena.

In real applications though, slug flow is more complex. The next step is, so, to study a single Taylor drop rising in a tube with a flowing upward continuous phase (co-current).

In order to design experiments to study the co-current case, one must consider relevant dimensionless groups influencing the flow (Hayashi et al., 2011, Direito et al., 2016). The Eötvös number relates buoyancy and interfacial forces and is defined as:

$$\mathrm{Eo} = \frac{\Delta\rho\, g D^2}{\sigma}, \tag{5.1}$$

where ρ is the density, D stands for the tube diameter, g for the standard acceleration of gravity and σ is the surface tension. $\Delta\rho = \rho_{\mathrm{C}} - \rho_{\mathrm{D}}$, where the subscripts "$_{\mathrm{D}}$" and "$_{\mathrm{C}}$" stand for dispersed and continuous phase. Furthermore, the Morton number relates viscosity and surface tension forces:

$$\mathrm{M} = \frac{\Delta\rho\, g \mu_{\mathrm{C}}^4}{\rho_{\mathrm{C}}^2\, \sigma^3}, \tag{5.2}$$

where μ stands for viscosity.

Additionally, it is necessary to consider the ratios of density and viscosity:

$$\rho^* = \frac{\rho_{\mathrm{D}}}{\rho_{\mathrm{C}}}, \tag{5.3}$$

$$\mu^* = \frac{\mu_{\mathrm{D}}}{\mu_{\mathrm{C}}}. \tag{5.4}$$

Notice that, for drops rising in a heavier liquid, the density ratio is always less than 1.

When Eötvös number is high and the viscosity ratio is low enough, the liquid-liquid isolated drop case should approach the behavior of a gas Taylor bubble rising in a liquid flowing in a macro tube. That happens because the density difference is high and/or the interfacial tension is low (gravity effects are predominant). On the other hand, for low Eötvös, Morton is required to quantify the importance of the viscous forces. Low Eötvös and high Morton numbers implicate a high viscosity of the continuous phase. If the viscosity ratio is high, such combination should be observed when, at the macro-scale, both fluids have close densities (viscous effects are predominant). For low Eötvös and Morton numbers and low viscosity ratio, the flow should be similar to that of a gas Taylor bubble flowing in a liquid contained in a micro tube (surface tension effects are predominant).

In the present work, though, one must also account for the motion of the continuous phase. The ratio between the continuous phase average velocity and the drop terminal velocity in stagnant liquid was chosen to design the simulations:

$$u^* = \frac{U_\mathrm{C}}{V_\mathrm{T}}. \tag{5.5}$$

The Reynolds number of the continuous phase gives information on the continuous phase flow regime:

$$\mathrm{Re}_\mathrm{C} = \frac{\rho_\mathrm{C}\, U_\mathrm{C}\, D}{\mu_\mathrm{C}}. \tag{5.6}$$

The Reynold number based on the dispersed phase velocity is defined as:

$$\mathrm{Re}_\mathrm{D} = \frac{\rho_\mathrm{C}\, V_\mathrm{TC}\, D}{\mu_\mathrm{C}}, \tag{5.7}$$

where $V_\mathrm{TC}$is the drop velocity in co-current.

In gas-liquid, the relationship between the bubble velocity and the continuous phase velocity has been the scope of several studies (Morgado et al., 2016). Nicklin et al. (1962) proposed the following law:

$$V_\mathrm{TC} = V_\mathrm{T} + C U_\mathrm{C}, \tag{5.8}$$

or, dividing by V_T:

$$V_\mathrm{TC}/V_\mathrm{T} = 1 + C u^*, \tag{5.9}$$

where C is a constant, which depends on the system dimensionless groups (Fabre and Line, 1992). Nicklin et al. (1962) also found that bubbles are faster in laminar flow than in turbulent regime. Collins et al. (1978) proposed $C = 2.27$ for laminar regime. In a later work (Bendiksen, 1985, Fabre and Line, 1992) a function of Eötvös number was proposed for laminar regime:

$$C = 2.29 \left(1 - \frac{20}{\mathrm{Eo}} \left(1 - e^{-0.0125\,\mathrm{Eo}} \right) \right). \tag{5.10}$$

Pinto et al. (1998) obtained similar values and reported results for the transition region, as well. They also related the liquid Reynolds number to the wake region behavior. Nogueira et al. (2006) reported an experimental study where three types of wakes were observed at the rear of Taylor bubbles. Moreover, they also observed that longer bubbles are required for the liquid film flowing around the bubble to become fully developed, in co-current operation. Lu and Prosperetti (2009) studied numerically the effect of Eötvös and Morton numbers. They reported a relationship between the distance below the bubble disturbed by the bubble flow and the velocity of the continuous phase, observing very long circulations in some conditions. Quan (2011) studied numerically systems with a density ratio of 0.01, reporting bubble shapes and detailed velocity profiles. They observed that an increase in continuous phase velocity elongates the bubble and tends to create flow separation below the bubble. The existence of thin protuberances on the bottom edges of the drops (“skirts” – (Viana et al., 2003, Ray and Prosperetti, 2014)) were reported on both numerical studies (Lu and Prosperetti, 2009, Quan, 2011).

Gas-liquid co-current flow is also important at the micro-scale (Liu et al., 2005, Abiev and Lavretsov, 2012). In order to evaluate when the present study approaches the conditions of the micro-scale, the capillary number is defined:

$$\mathrm{Ca}_\mathrm{C} = \frac{U_\mathrm{C}\, \mu_\mathrm{C}}{\sigma} = \mathrm{Re}_\mathrm{C} \sqrt{\mathrm{M}\, \mathrm{Eo}^{-1}} \tag{5.11}$$

In such conditions, the ratio between the velocity acquired by a Taylor bubble/drop and the continuous phase co-current velocity can be described by just one dimensionless number (Liu et al., 2005):

$$\frac{V_{\mathrm{TC}}}{U_{\mathrm{C}}} = \frac{1}{1 - 0.61{\mathrm{Ca}_{\mathrm{C}}}^{0.33}}. \tag{5.12}$$

To account for the terminal velocity (which is null in micro tubes), the equation can be re-written as:

$$\frac{V_{\mathrm{TC}} - V_{\mathrm{T}}}{U_{\mathrm{C}}} = \frac{1}{1 - 0.61{\mathrm{Ca}_{\mathrm{C}}}^{0.33}}. \tag{5.13}$$

This equation represents the limit of $\left(V_{\mathrm{TC}} - V_{\mathrm{T}}\right)/U_{\mathrm{C}}$ when effects of gravity vanish.

In slug flow, two drops might coalesce because the flow in the wake of the leading drop causes an increase in the trailing drop velocity (Araújo et al., 2013). Hence, the interaction between two drops is of foremost importance. It is highly dependent on the disturbance that the leading drop causes in the continuous phase flow below it. To evaluate that disturbance, consider, in the tube axis, the distance from the drop bottom needed for the vertical velocity component to fulfill a defined criterion – a of deviation of less than 5 % from the undisturbed value (Direito et al., 2016). The normalized stabilization distance is given by:

$$Z_{\mathrm{III}} = \frac{\text{stabilization distance}}{D}. \tag{5.14}$$

The present work concerns numerical simulations designed to assess the influence of the relevant forces in the flow, namely the Taylor drop rising velocity, by studying the dimensionless numbers in the ranges $0.01 \leq \mu^* \leq 10$, $8 \leq \mathrm{Eo} \leq 30$ and $2.32 \times 10^{-6} \leq \mathrm{M} \leq 100$.

5.2.1 Numerical model

The present work was develped using the commercial package Ansys Fluent. A multiphase laminar incompressible flow model integrated with Volume of Fluid (VOF) method was used (Hirt and Nichols, 1981) with geometric reconstruction (Youngs, 1982). The scalar gradients were computed by the Green-Gauss node-based method. Regarding pressure-velocity coupling, PISO (Issa, 1986) was used, a non-iterative algorithm which splits the solution into predictor and corrector steps. For pressure interpolations, a pressure staggering option scheme was chosen (Patankar, 1980) – “Presto!” in the software package. The QUICK (Leonard, 1979) scheme was used for solving the momentum equation. To account for the interfacial forces, the Continuum Surface Force model (Brackbill et al., 1992) was used. It creates the interface between the two liquids as a transition region of finite thickness where the surface tension force term is proportional to the curvature in each location. Outside the interface, this force term is zero.

In order to deal with the two-phase flow, a variable α_i was defined. The value of α_i is 1 at any point occupied exclusively by the fluid i, 0 if no i exists there, or a number between 0 and 1, if both fluids exist in the same mesh element:

$$\alpha_{\mathrm{C}} + \alpha_{\mathrm{D}} = 1. \tag{5.15}$$

Note that cells with $\alpha_{\mathrm{D}} \neq 0 \wedge \alpha_{\mathrm{D}} \neq 1$ represent the interface between the two liquids. On such cells, density and viscosity are computed supposing linear contributions of each phase.

All simulations were transient and performed with a maximum Courant number of 0.25.

The domain is represented in Figure 5.1. Axial symmetry (around the cylinder axis) – axisymmetry – was used to minimize computational effort. When concerning Taylor bubbles and drops, this approach has been widely used and observed, both in theoretical (Collins et al., 1978, Mandal et al., 2007), experimental (Davies and Taylor, 1950, White and Beardmore, 1962, Mandal et al., 2008, Araújo et al., 2012) or numerical studies (Hayashi et al., 2011, Kurimoto et al., 2013). The domain consisted of a rectangle

Table 5.1: Mesh test conditions and difference in drop velocity between the two meshes.

Eo	M	μ^*	ρ^*	d_S/D	u^*	dif. in V_b
8	2.32×10^{-6}	10	0.792	1.12	2	3 %
22	10^{-4}	10	0.792	1.12	2	< 1 %
22	100	10	0.792	1.12	2	< 1 %
22	100	0.1	0.792	1.12	2	< 1 %

with a width $D/2$ and $11D$ long. The mesh consisted of a 52×1144 grid of quadrilateral and uniformly distributed cells. This mesh allows for a correct flow description. For example, in the narrowest part of the continuous phase film in the stagnant Eo $= 8$, M $= 100$ and $\mu^* = 10$ simulation, there are six cells in the radial direction.

Simulations were initialized using the drop shape and velocity field from the corresponding stagnant case(Direito et al., 2016).

A reference frame attached to the drop nose was used (Direito et al., 2016). In this reference frame, the drop is still and the continuous phase and the tube wall move downwards. The wall velocity boundary condition is set to the value of the drop velocity. Moreover, an inlet flow boundary condition (at the top of the domain) was imposed. The velocity profile in this boundary consists of the parabolic profile subtracted by the drop velocity:

$$u(r) = -V_\mathrm{TC} + 2\,U_\mathrm{C}\left(1 - (2r/D)^2\right), \tag{5.16}$$

where r is the radial coordinate. It was implemented through an "User defined function" in Ansys Fluent. At the tube exit, pressure is set to zero gauge.

The final result for each condition is obtained by an iterative method. A first simulation is run for a drop velocity estimated by Eq. 5.9 with C calculated by Eq. 5.10. The new drop velocity obtained in this simulation is used as input in the next simulation by adjusting boundary conditions in the wall and at the inlet. This process repeats until the drop velocity converges (corresponding to a < 1 % variation in velocity). Simulation is, then, run again (at least 2000 time-steps) in order to obtain the relevant flow data.

A finer grid (about 8 times more cells, without any change in the domain geometry and dimensions) was also tested, but showed identical results (same drop velocity and shape and same velocity field for the conditions in Table 5.1 – see also example in Figure 5.2) and it was dropped due to its high computation time.

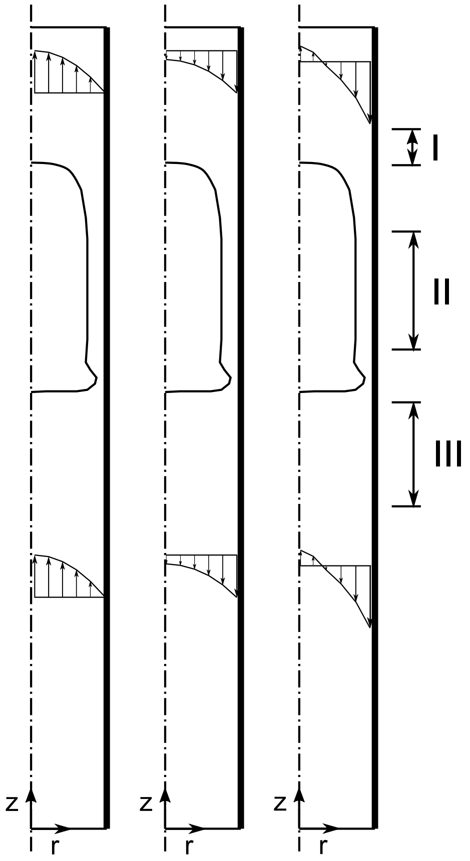

Figure 5.1: Axisymmetric domain with drop. Velocity profiles: earth reference frame (left), drop nose reference frame for drops faster than undisturbed continuous phase (middle) and drop nose reference frame for drops slower than portions of undisturbed continuous phase (right). Marked region above the drop (I), continuous phase film (II) and wake (III).

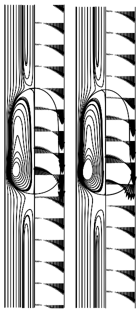

Figure 5.2: Flow fields with the chosen mesh (left) and finer mesh (right) for Eo = 8, M = 2.32×10^{-6}, $\mu^* = 10$ and $u^* = 2$.

5.3 Results

A numerical study was designed using the dimensionless groups relevant in the stagnant case as the starting point. As shown previously (Direito et al., 2016), a study like this should take into account the Eötvös number, the Morton number and the viscosity ratio. In order to ensure the validity of the axisymmetric model, the dimensionless numbers were ranged this way: $0.01 \leq \mu^* \leq 10$, $8 \leq \mathrm{Eo} \leq 30$ and $2.32 \times 10^{-6} \leq \mathrm{M} \leq 100$. Concerning the density ratio, the value 0.792 was used. In the stagnant case, Hayashi et al. (2011) showed that the density ratio does not influence the flow. Nevertheless, test with a lower density ratio was performed, but no significant changes were found. Furthermore, $d_{\mathrm{S}}/D = 1.12$ is the drop size (the ratio between the diameter of the drop volume-equivalent sphere and the pipe diameter). In a similar fashion, a test was run for 1.4, also with no significant differences. Details on these runs are provided in Table 5.2, showing no influence of these parameters on the velocity drop results. These results hint that any possible difference between gas-liquid and liquid-liquid should be driven by the viscosity ratio.

For each set of stagnant dimensionless numbers, co-current simulations were performed at $u^* = 0.5$, 2 and 5.

5.3.1 Flow patterns

Figure 5.3 presents simulation results where Eötvös and u^* are changed. Firstly it is important to make a distinction between observable flow patterns.

Generally, for low values of Eötvös number (strong influence of interfacial forces), drops tend to be bulkier and show a rounded lower part. As Eötvös increases, drops tend to be more elongated and their bottom flattens. These observations agree with the behavior already described in literature for drops rising in stagnant liquid (Direito et al., 2016).

When u^* is low, the effect of gravity dominates. Notice that very few differences in drop shape exist between $u^* = 0$ and $u^* = 0.5$. Furthermore, and according to the streamlines, the drop velocity is faster than the velocity of all the continuous phase and so all the liquid is overtaken by the drop.

With the increase in u^*, the influence of the convective effect of the continuous phase flow grows. Concerning the case for Eo = 8 at $u^* = 5$, semi-infinite circulation lines appear in the drop reference frame representation (ahead and below the drop). Inside these regions, the continuous phase moves at an average velocity that is equal to the drop velocity. The liquid flowing ahead, inside the circulation region, is never overtaken by the drop. Similar flow behavior can be found, for example, in the work of Lu and Prosperetti (2009).

Closed recirculations at the bottom of the drop start to appear for the higher Eötvös values, when the continuous phase velocity is high enough. Furthermore, in cases such as Eo = 22 and $u^* = 5$, closed recirculations and semi-infinite circulations occur simultaneously. Hence, an overlap of both is observable below the drop. An interesting behavior concerns the location of the closed recirculations. In gas-liquid

Table 5.2: Influence of density ratio and drop size.

Eo	$\log \mathrm{M}$	μ^*	ρ^*	d_{S}/D	C
8	-5.6	10	0.792	1.12	1.36
			0.0792	1.12	1.35
22	2	0.041	0.792	1.12	1.65
			0.792	1.40	1.64

co-current flow, one can find closed recirculations attached to the bubble bottom (Nogueira et al., 2006). On the other hand, the current results show a gap between the closed recirculation region and the drop (Eo = 30 and $u^* = 0.5$ in Figure 5.3).

5.3.2 Drop shape

An important characteristic in some Taylor drops is the bottom oscillation. Concerning stagnant continuous phase in the range studied, one will only find an oscillating drop at high Morton and Eötvös numbers (Figure 5.4). An interesting effect of the co-current flow is the appearance of those effects at lower Morton number values. At Eo = 22, $\mu^* = 10$ and $M = 10^{-4}$, high enough continuous phase velocity causes oscillations to occur (Figure 5.4).

At $M = 100$, $Eo = 22$ and $\mu^* = 0.1$ (Figure 5.5, first row), the film velocity profile tends to stagnation with the increase of u^*. Despite the continuous phase velocity being high, there are not semi-infinite circulations. This happens because of the bypass flow in non-gravity conditions (Thulasidas et al., 1997, Abiev, 2009).

Regarding variations in continuous phase velocity at $M = 100$, $Eo = 8$ and $\mu^* = 10$ (Figure 5.5, second row), it is still possible to detect a small drop elongation with the increase of the continuous phase velocity. The increase in u^* promotes the existence of semi-infinite circulation lines. At $u^* = 2$, the radial velocity in the region exiting the drop bottom is still relevant, causing an almost quiescent gap region (MRF) between the drop bottom and the portion of continuous phase that moves at the drop velocity.

For changes in viscosity ratio (Figure 5.6), drop shape and continuous phase flow show little differences in the flow patterns. However, a mild effect of drop dimensions is observable. The film at higher viscosities is less thick. Furthermore, an increase in viscosity ratio causes the arising of the aforementioned semi-infinite circulation lines ($\mu^* = 10$). Below this drop, the semi-infinite circulation is not attached to the drop bottom. Instead, there is some fluid flowing at the drop velocity (stagnant relatively to the drop) between the drop and the semi-infinite region.

5.3.3 Further effects on continuous phase

After a qualitatively overview, more information on the continuous phase flow can be obtained by analyzing relevant parameters on the film region and in the wake of the drop.

The velocity profile in the film (Figure 5.7) is greatly affected by the continuous phase velocity. With the increase in the importance of the continuous phase flow, v_{P}, the maximum downward velocity (in earth reference frame, normalized by the drop velocity), reduces significantly (Figure 5.8). Furthermore, on such conditions, the inner portion of the film moves upwards.

For high viscosity ratios (Figure 5.7, A and B), the maximum velocity appears far from the interface (analogous result in stagnant continuous phase can be seen in Direito et al. (2016)).

Regarding Figure 5.7 – D, the velocity profile presented for u*=5 corresponds to the previously mentioned conditions where the film is almost stagnant (Figure 5.5).

The interaction between two drops is highly dependent on the disturbance that the leading drop causes in the continuous phase flow below it (region III in Figure 5.1) – Eq. 5.14. In Figure 5.9, the results are separated in three series: the stagnant cases (which do not have closed recirculations), the co-current cases without closed recirculations and the ones with closed recirculations below. The stabilization distance was found to be a fairly good function of the dispersed phase Reynolds number. For low Reynolds, viscous forces are dominant and the continuous phase flow is not greatly affected. Moreover, coalescence of two drops in these conditions is unlikely to happen due to the such short disturbed flow. With the increase

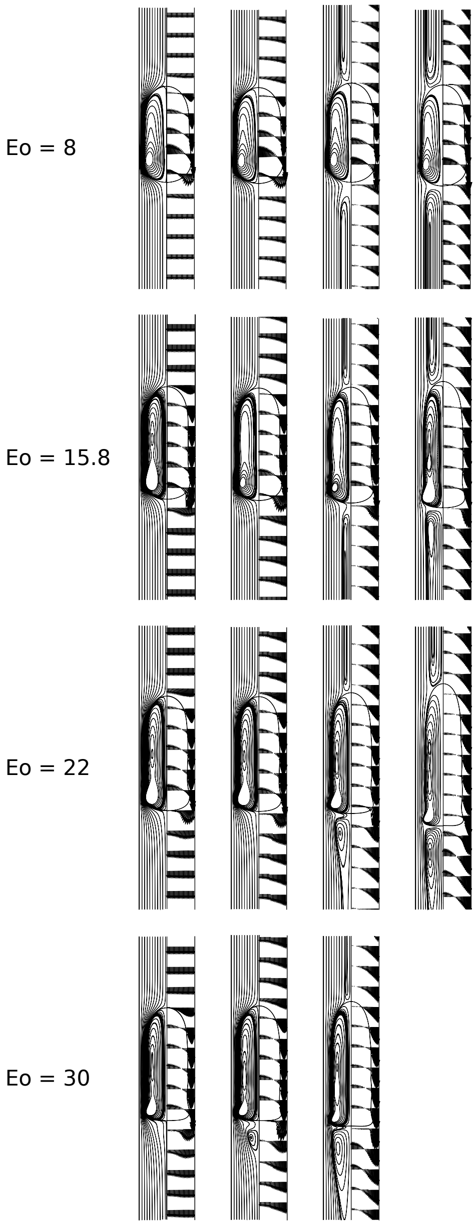

Figure 5.3: Drops for constant M $= 2.32 \times 10^{-6}$ and $\mu^* = 10$ in drop nose reference frame – from left to right: $u^* = 0$ (Direito et al., 2016), $u^* = 0.5$, $u^* = 2$, $u^* = 5$.

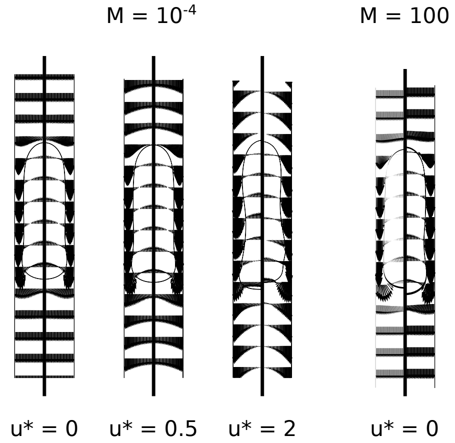

Figure 5.4: Drop shape and velocity field (drop reference frame) at Eo = 22 and $\mu^* = 10$ (two instants are shown – left and right).

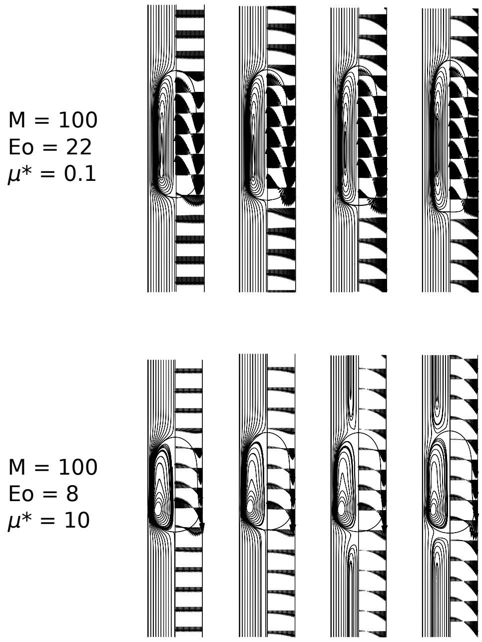

Figure 5.5: Two different drops in drop nose reference frame, with two snapshots when shape oscillation occurs – from left to right: $u^* = 0$ (Direito et al., 2016), $u^* = 0.5$, $u^* = 2$, $u^* = 5$.

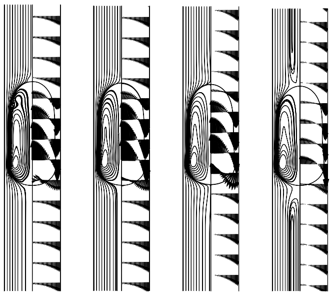

Figure 5.6: Drops for constant M = 100, Eo = 8 and $u^* = 2$ in drop nose reference frame – from left to right: $\mu^* = 0.01$, 0.1, 1 and 10.

in Reynolds, the stabilization distance increases and closed recirculations start to appear ($\mathrm{Re_D} > 100$).

5.3.4 Drop velocity

As mentioned previously, for each set of stagnant dimensionless numbers, co-current simulations were performed at $u^* = 0.5$, 2 and 5. In order to obtain the slope C in Eq. 5.8), terminal velocity of stagnant simulations (Direito et al., 2016) are also used.

Applying the Eq. 5.8, it is possible to obtain the parameter C. Figure 5.11 shows that parameter as a function of the relevant dimensionless numbers. In order to obtain the line parameters, the sum of the squares of the relative deviations was minimized (three examples are presented in Figure 5.10).

The parameter C shows a small sensitivity to Eötvös. Regarding the influence of Morton number (Figure 5.11 – middle), a small change in C is observed, being something higher for higher Morton numbers.

Simulations were performed for different viscosity ratios at constant Eötvös number and Morton number (Eo = 8 and M = 100 – Figure 5.11). For the higher viscosity ratio, C takes approximately the value of 1.4. However, with the decrease of μ^*, and thus the approximation to gas-liquid, the parameter increases. At $\mu^* = 0.01$, it is already very close to the value 1.75 predicted by Eq. 5.10(Bendiksen, 1985).

In order to cope with the effect of viscosity ratio (Figure 5.11, bottom), an additional factor was introduced to Eq. 5.10, and adjusted to the results of the present work:

$$\begin{aligned} C = 2.29 &\left(1 - \frac{20}{\mathrm{Eo}}\left(1 - e^{-0.0125\,\mathrm{Eo}}\right)\right) \\ \times &\left(1 - \frac{0.128}{1/\mu^*}\left(1 - e^{-1.42\,(1/\mu^*)}\right)\right), \end{aligned} \tag{5.17}$$

for a range $8 \le \mathrm{Eo} \le 30$, $2.32 \times 10^{-6} \le \mathrm{M} \le 100$ and $0.01 \le \mu^* \le 10$, constrained by the validity of axisymmetry (Direito et al., 2016, 2017) – roughly for $\mu^* \le 1$ when $\mathrm{Eo} \ge 15.8$ and $\mathrm{M} < 1$ the drops are not symmetric.

Figure 5.12 shows a good match between the correlation and the numerical results (a total of 14 points with standard deviation $\sigma^2 = 0.0228$). Note that, for gas-liquid, the viscosity ratio tend to zero and Eq. 5.17 becomes Eq. 5.10.

5.3.5 Drop velocity limits

Lower limit

The drop velocity has two important contributions: the terminal velocity rendering the gravity effect and the continuous phase co-current flow. In order to understand how the two effects influence the drop velocity, consider Figure 5.13, where $\frac{V_{\mathrm{TC}} - V_{\mathrm{T}}}{U_{\mathrm{C}}}$ is presented as a function of the capillary number (Ca_C) for all the simulations in the present work. Futhermore, Eq. 5.13 is also presented as a line, corresponding to the region of no gravity. As Eq. 5.13 is an adaptation of a correlation developed for capillaries (Liu et al., 2005), a set of six new simulations were run without gravity (Table 5.3), in order to confirm the validity of such adaptation. The correlation stands as a lower limit for the results of the present work.

The values obtained with gravity that are closest to the lower limit are those obtained with high viscosity ratios (already seen in Figure 5.11), in particular those corresponding to high continuous phase velocities (capillary number higher than 0.1). These results are consistent, since the terminal velocity of the drop decreases by increasing the ratio between the viscosities of the phases (Direito et al., 2016).

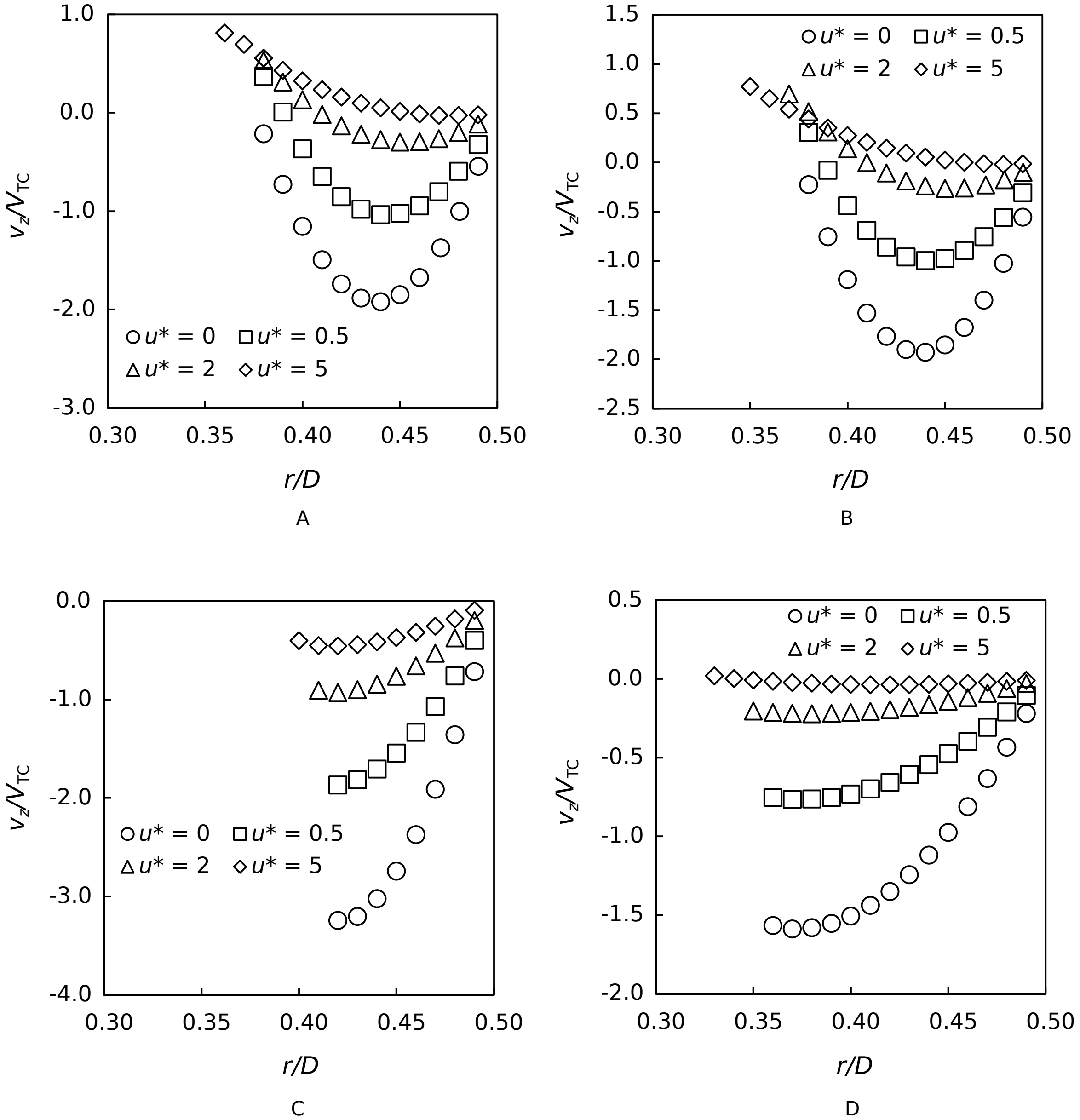

Figure 5.7: Axial velocity profile in the film – earth reference frame (A: M $= 2.32 \times 10^{-6}$, Eo $= 15.8$ and $\mu^* = 10$; B: M $= 2.32 \times 10^{-6}$, Eo $= 22$ and $\mu^* = 10$, C: M $= 2.32 \times 10^{-6}$, Eo $= 8$ and $\mu^* = 0.1$; D: M $= 100$, Eo $= 22$ and $\mu^* = 10$).

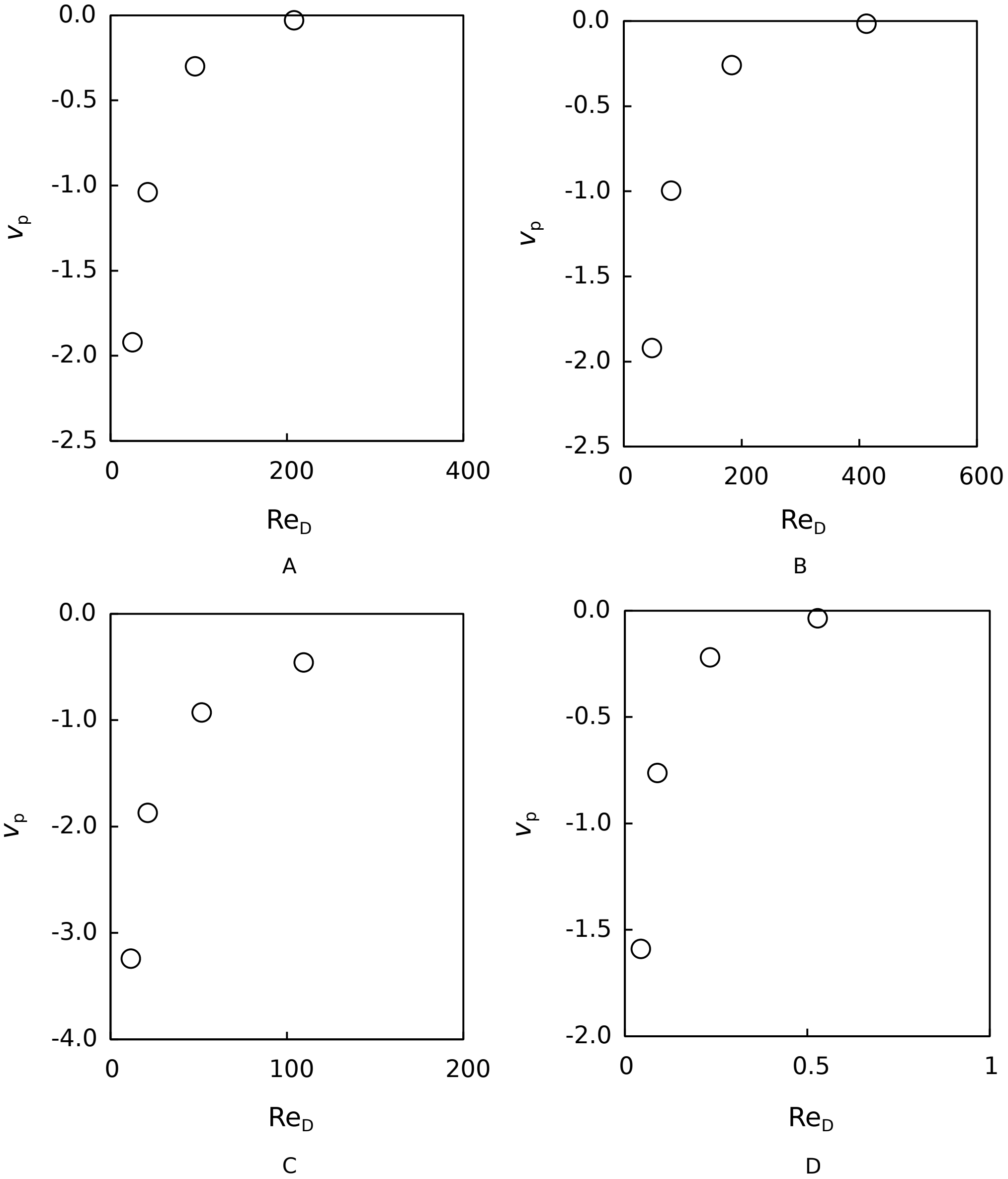

Figure 5.8: Velocity maximum in the film – earth reference frame (A: M = 2.32×10^{-6}, Eo = 15.8 and $\mu^* = 10$; B: M = 2.32×10^{-6}, Eo = 22 and $\mu^* = 10$, C: M = 2.32×10^{-6}, Eo = 8 and $\mu^* = 0.1$; D: M = 100, Eo = 22 and $\mu^* = 10$).

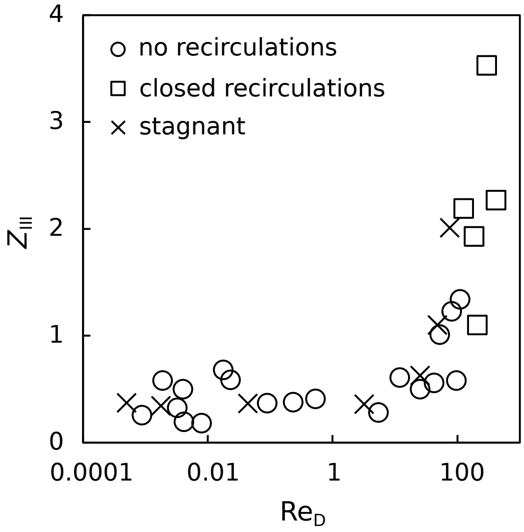

Figure 5.9: Stabilization distance below the drop (stagnant simulations, co-current simulations without closed recirculation and co-current with closed recirculations).

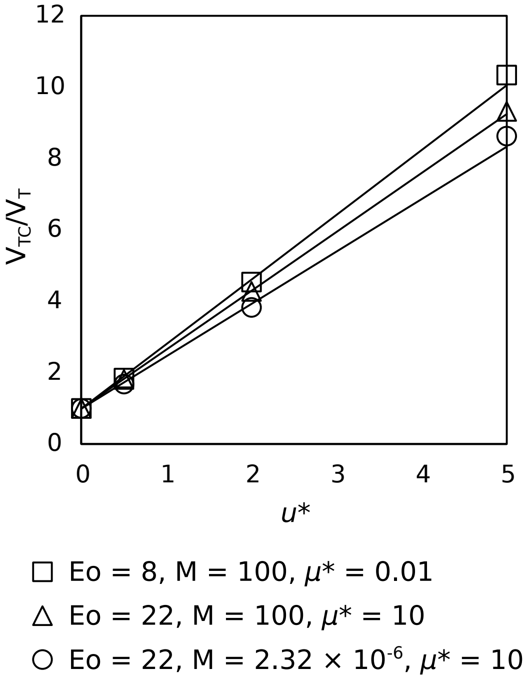

Figure 5.10: Examples of determination of slope C.

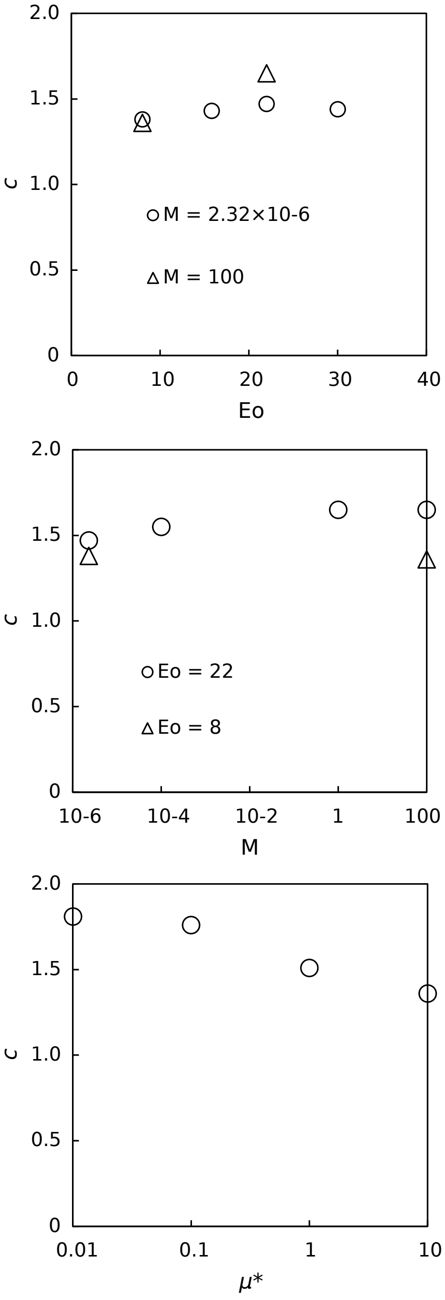

Figure 5.11: C for constant Morton number at $\mu^* = 10$ (top), for Eo $= 22$ and $\mu^* = 10$ (middle) and for Eo $= 8$ and M $= 100$ (bottom).

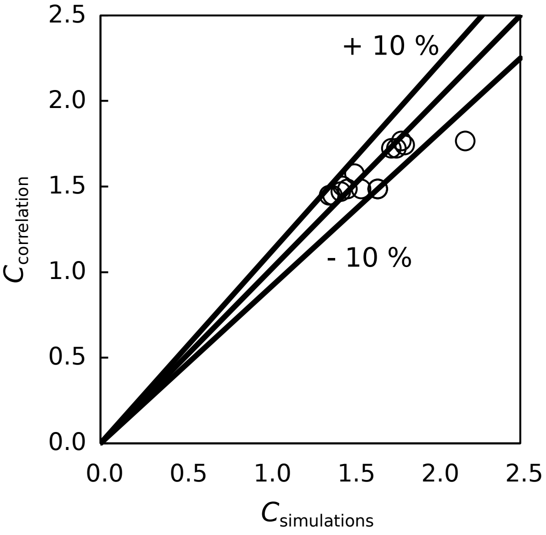

Figure 5.12: Correlation for C.

Table 5.3: Simulations without gravity.

Eo	log M	μ^*	u^*
8	-5.6	0.1	2
8	100	0.01	5
22	0	10	5
22	2	0.1	0.5
22	2	0.1	5
30	-5.6	10	2

These results also suggest that the viscosity ratio influences mainly the gravitational component of the drop velocity.

As expected, for low values of capillary number the drop velocity in non-gravity flow tends to the velocity of the continuous phase. In the opposite direction, $\frac{V_{\mathrm{TC}}-V_{\mathrm{T}}}{U_{\mathrm{C}}}$ increases with the increase of Ca_C (more influence of continuous phase viscous effects in relation to the interfacial tension forces).

The results that past the value of 2 for $\frac{V_{\mathrm{TC}}-V_{\mathrm{T}}}{U_{\mathrm{C}}}$ correspond to the existence of bypass flow (in non-gravity conditions), as discussed earlier (Figure 5.5).

Upper limit

According to Eq. 5.17 the drop velocity increases with the increase of the Eötvös number. The upper limit of $\frac{V_{\mathrm{TC}}-V_{\mathrm{T}}}{U_{\mathrm{C}}}$ is, according to Eq. 5.17, 2.29, a typical value of a gas Taylor bubble rising, in a macro tube, in the viscous regime in a liquid with no interfacial tension. According to Figure 5.13 this upper limit is achieved for low values of the ratio of viscosities, high velocities of the continuous phase. Moreover, observe that this upper limit appears when viscosity forces are more important than interfacial tension forces.

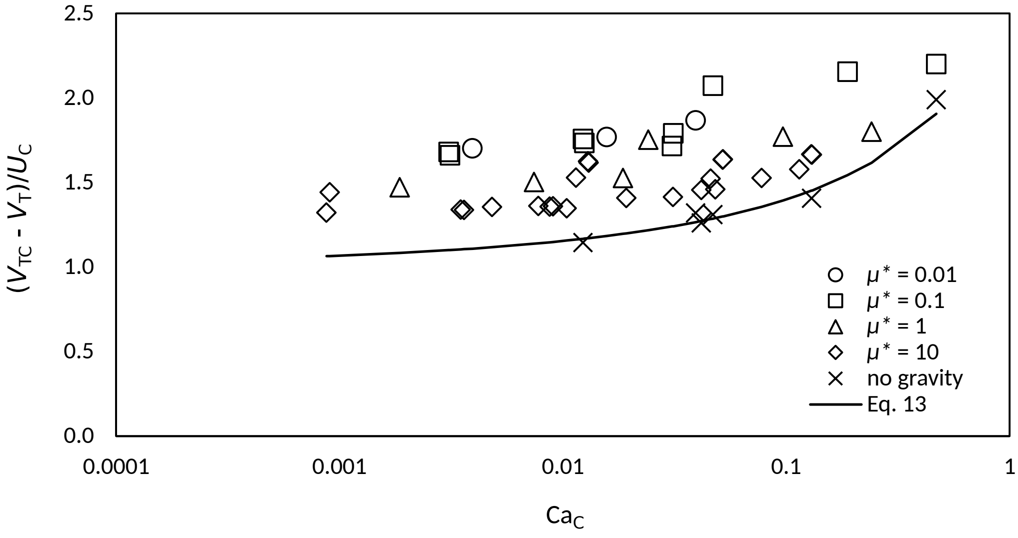

Figure 5.13: Drop velocity and capillarity.

5.4 Conclusions

Taking into consideration the importance of multiphase flow patterns, the present work studied Taylor drops rising in co-current fully developed laminar flow in a vertical tube. A series of Computational Fluid Dynamic results were generated consisting of drop velocities, velocity field, drop shapes, employing a two-dimensional axisymmetric model validated in previous works.

The results reported were obtained for $0.01 \leq \mu^* \leq 10$, $8 \leq \mathrm{Eo} \leq 30$ and $2.32 \times 10^{-6} \leq \mathrm{M} \leq 100$. Information on drop velocity was collected obtaining the slope value for the linear relationship between drop terminal velocity and continuous phase velocity. Furthermore, the influence of dimensionless numbers on drop shapes and velocity profiles was assessed.

The balance between gravity effects and convective co-current effects was found to be crucial to understand the phenomena.

The increase in the continuous phase velocity makes the co-current effects more important in relation to gravity. It promotes inertial effects, causing closed recirculations to appear at lower Eötvös numbers. Some closed recirculations are separated from the drop bottom by a small portion of non-circulatory fluid flowing at the drop velocity. At high Eötvös number, continuous phase velocity may also anticipate the occurrence of shape oscillations to lower Morton number values. High enough continuous phase velocity also causes the inner portion of the flow to move, in average, at the drop velocity, above and below the drop. These regions are seen through semi-infinite recirculation streamlines when analyzing the flow in a drop reference frame.

At high values of Eötvös number and low values of Morton number, similarities between the liquid-liquid system and the gas-liquid system arise. At low values of Eötvös number and low gravity effects, the flow approaches the flow behavior in micro-channels.

The velocity profile in the film around the drop depends highly on the viscosity ratio. For low viscosity ratios, it approaches the behavior in gas-liquid, while greater values of the viscosity ratio cause the maximum downward velocity to relocate to a middle position in the film flow. For low viscosity ratios, a stagnant film can be observed for conditions where bypass flow happens.

The stabilization distance below the drop presents a baseline for low drop Reynolds number and starts to increase around Reynolds 10. The cases where closed recirculations are observed appear in the higher Reynolds number range (hence, corresponding to the higher stabilization distances).

A linear relationship between the drop terminal velocity and the continuous phase velocity was found and the values for different conditions were reported. An adaptation of the data to an existing correlation to preview the drop velocity was done with success. It takes into account that, in liquid-liquid, the viscosity ratio is the major driving force. Comparison between these results and those obtained in non-gravity conditions suggests that the viscosity ratio acts mainly in the gravitational component of the drop velocity.

Both, viscous flow in gas-liquid and micro-channel flow constitute two bounds for the present set of studied conditions.

The present work presents important data for Taylor drop in co-current flow and it is, thus, an important step for a more general knowledge on liquid-liquid slug flow.

Acknowledgements

This work was funded by FEDER funds through the Operational Programme for Competitiveness Factors COMPETE and National Funds through FCT (Fundação para a Ciência e a Tecnologia) under the project PEst-OE/EME/UI0532. Filipe Direito gratefully acknowledge the financial support from the FCT through Ph.D. Grant SFRH/BD/79264/2011.

References

Abiev, R. and Lavretsov, I. (2012), ‘Intensification of mass transfer from liquid to capillary wall by Taylor vortices in minichannels, bubble velocity and pressure drop’, *Chemical Engineering Science* **74**, 59–68.

Abiev, R. S. (2009), ‘Circulation and bypass modes of the slug flow of a gas-liquid mixture in capillaries’, *Theoretical Foundations of Chemical Engineering* **43**(3), 298–306.

Araújo, J., Miranda, J. and Campos, J. (2013), ‘Simulation of slug flow systems under laminar regime: Hydrodynamics with individual and a pair of consecutive Taylor bubbles’, *Journal of Petroleum Science and Engineering* **111**, 1–14.

Araújo, J., Miranda, J., Pinto, A. and Campos, J. (2012), ‘Wide-ranging survey on the laminar flow of individual Taylor bubbles rising through stagnant Newtonian liquids’, *International Journal of Multiphase Flow* **43**, 131–148.

Aziz, I. A. B., Brandt, I., Gunasekera, D., Hatveit, B., Havre, K., Weisz, G., Xu, Z. G., Nas, S. and Spilling, K. E. (2015), ‘Multiphase Flow Simulation: Optimizing Field Productivity’, *Oilfield Review* **27**(1), 26–37.

Babadagli, T. (2007), ‘Development of mature oil fields A review’, *Journal of Petroleum Science and Engineering* **57**(3-4), 221–246.

Bannwart, A. C., Rodriguez, O. M. H., de Carvalho, C. H. M., Wang, I. S. and Vara, R. M. O. (2004), ‘Flow Patterns in Heavy Crude Oil-Water Flow’, *Journal of Energy Resources Technology* **126**(3), 184.

Bannwart, A., Rodriguez, O., Trevisan, F., Vieira, F. and de Carvalho, C. (2009), ‘Experimental investigation on liquidliquidgas flow: Flow patterns and pressure-gradient’, *Journal of Petroleum Science and Engineering* **65**(1-2), 1–13.

Bendiksen, K. H. (1985), ‘On the Motion of Long Bubbles in Vertical Tubes’, *International Journal of Multiphase Flow* **11**, 797–812.

Brackbill, J. U., Kothe, D. B. and Zemach, C. (1992), ‘A Continuum Method for modeling surface tension’, *Journal of Computational Physics* **100**, 335–354.

Brown, R. and Govier, G. (1961), ‘High-Speed Photography in the Study of Two-Phase Flow’, *The Canadian Journal of Chemical Engineering* **39**, 159–164.

Collins, R., Moraes, F. F. D., Davidson, J. F. and Harrison, D. (1978), ‘The motion of a large gas bubble rising through liquid flowing in a tube’, *Journal of Fluid Mechanics* **89**(03), 497–514.

Davies, R. M. and Taylor, G. (1950), ‘The Mechanics of Large Bubbles Rising through Extended Liquids and through Liquids in Tubes’, *Proceedings of the Royal Society A: Mathematical, Physical and Engineering Sciences* **200**(1062), 375–390.

Direito, F. J. N., Campos, J. B. L. M. and Miranda, J. M. (2016), ‘Rising of a single Taylor drop in a stagnant liquid – 2D laminar flow and axisymmetry limits’, *Physics of Fluids* **28**(5), 057101.

Direito, F. J. N., Morgado, A. O., Rocha, L. A. M., Miranda, J. M. and Campos, J. B. L. M. (2017), ‘Experimental and numerical 3D study of a Taylor drop rising in a stagnant heavier liquid’, *Physics of Fluids* **29**(3), 037109.

Fabre, J. and Line, A. (1992), ‘Modeling of 2-Phase Slug Flow’, *Annual Review of Fluid Mechanics* **24**, 21–46.

Govier, G., Sullivan, G. and Wood, R. (1961), ‘The Upward Vertical Flow of Oil-Water Mixtures’, *The Canadian Journal of Chemical Engineering* **39**, 67–75.

Hayashi, K., Kurimoto, R. and Tomiyama, A. (2011), ‘Terminal velocity of a Taylor drop in a vertical pipe’, *International Journal of Multiphase Flow* **37**(3), 241–251.

Hirt, C. W. and Nichols, B. D. (1981), ‘Volume of Fluid (VOF) Method for the Dynamics of Free Boundaries’, *Journal of Computational Physics* **39**, 201–225.

Issa, R. I. (1986), ‘Solution of the implicitly discretised fluid flow equations by operator-splitting’, *Journal of Computational Physics* **62**(1), 40–65.

Kurimoto, R., Hayashi, K. and Tomiyama, A. (2013), ‘Terminal velocities of clean and fully-contaminated drops in vertical pipes’, *International Journal of Multiphase Flow* **49**, 8–23.

Leonard, B. P. (1979), ‘A stable and accurate convective modelling procedure based on quadratic upstream interpolation’, *Computer Methods in Applied Mechanics and Engineering* **19**(1), 59–98.

Liu, H., Vandu, C. O. and Krishna, R. (2005), ‘Hydrodynamics of taylor flow in vertical capillaries: Flow regimes, bubble rise velocity, liquid slug length, and pressure drop’, *Industrial and Engineering Chemistry Research* **44**(14), 4884–4897.

Lu, X. and Prosperetti, A. (2009), ‘A numerical study of taylor bubbles’, *Industrial and Engineering Chemistry Research* **48**(1), 242–252.

Lyons, W. C. and Plisga, G. J. (1999), *Standard handbook of petroleum and natural gas engineering*, Elsevier.

Mandal, T., Das, G. and Das, P. (2008), ‘Motion of Taylor Bubbles and Taylor Drops in Liquid-Liquid Systems’, *Industrial & Engineering Chemistry Research* **47**(18), 7048–7057.

Mandal, T., Das, G. and Das, P. (2010), ‘An appraisal of liquidliquid slug flow in different pipe orientations’, *International Journal of Multiphase Flow* **36**(8), 661–671.

Mandal, T. K., Das, G. and Das, P. K. (2007), ‘Prediction of rise velocity of a liquid Taylor bubble in a vertical tube’, *Physics of Fluids* **19**(12), 128109.

Mandal, T. K., Das, G. and Das, P. K. (2009), ‘Liquid Taylor Bubbles Rising in a Vertical Column of a Heavier Liquid: An Approximate Analysis’, *Journal of Fluids Engineering* **131**(1), 011303.

Moissis, R. and Griffith, P. (1962), ‘Entrance Effects in a Two-Phase Slug Flow’, *Journal of Heat Transfer* **84**(1), 29.

Morgado, A., Miranda, J., Araújo, J. and Campos, J. B. (2016), ‘Review on vertical gas-liquid slug flow’, *International Journal of Multiphase Flow* **85**, 348–368.

Nicklin, D., Wilkes, J. and Davidson, J. (1962), ‘Two-Phase Flow in Verical Tubes’, *Trans. Inst. Chem. Eng* **40**.

Nogueira, S., Riethmuller, M., Campos, J. and Pinto, a. (2006), ‘Flow patterns in the wake of a Taylor bubble rising through vertical columns of stagnant and flowing Newtonian liquids: An experimental study’, *Chemical Engineering Science* **61**(22), 7199–7212.

Omebereiyari, N., Azzopardi, B., Lucas, D., Beyer, M. and Prasser, H. (2008), ‘The characteristics of gas/liquid flow in large risers at high pressures’, *International Journal of Multiphase Flow* **34**(5), 461–476.

Patankar, S. V. (1980), *Numerical Heat Transfer And Fluid Flow*, Hemisphere.

Pinto, A., Pinheiro, C. and Campos, J. (1998), ‘Coalescence of two gas slugs rising in a co-current flowing liquid in vertical tubes’, *Chemical engineering science* **53**(16), 2973–2983.

Quan, S. (2011), ‘Co-current flow effects on a rising Taylor bubble’, *International Journal of Multiphase Flow* **37**(8), 888–897.

Ray, B. and Prosperetti, A. (2014), ‘On skirted drops in an immiscible liquid’, *Chemical Engineering Science* **108**, 213–222.

Serapião, A. B. S. and Bannwart, A. C. (2013), ‘Knowledge Discovery for Classification of Three-Phase Vertical Flow Patterns of Heavy Oil from Pressure Drop and Flow Rate Data’, *Journal of Petroleum Engineering* **2013**.

Seyfried, R. and Freundt, A. (2000), ‘Experiments on conduit flow and eruption behavior of basaltic volcanic eruptions’, *Journal of Geophysical Research* **105**(B10), 23727.

Spedding, P., Woods, G., Raghunathan, R. and Watterson, J. (2000), ‘Flow Pattern, Holdup and Pressure Drop in Vertical and Near Vertical Two-and Three-Phase Upflow’, *Chemical Engineering Research and Design* **78**(3), 404–418.

Thulasidas, T. C., Abraham, M. A. and Cerro, R. L. (1997), ‘Flow patterns in liquid slugs during bubble-train flow inside capillaries’, *Chemical Engineering Science* **52**(17), 2947–2962.

Viana, F., Pardo, R., Yánez, R., Trallero, J. L. and Joseph, D. D. (2003), ‘Universal correlation for the rise velocity of long gas bubbles in round pipes’, *Journal of Fluid Mechanics* **494**, 379–398.

Villarreal, J., Laverde, D. and Fuentes, C. (2006), ‘Carbon-steel corrosion in multiphase slug flow and CO2’, *Corrosion Science* **48**(9), 2363–2379.

White, E. and Beardmore, R. (1962), ‘The velocity of rise of single cylindrical air bubbles through liquids contained in vertical tubes’, *Chemical Engineering Science* **17**(5), 351–361.

Youngs, D. L. (1982), Time-Dependent Multi-Material Flow with large Fluid Distorsion., *in* K. W. Morton and M. J. Baines, eds, ‘Numerical Methods in Fluid Dynamics’, Academic Press.

Zukoski, E. E. (1966), ‘Influence of viscosity, surface tension, and inclination angle on motion of long bubbles in closed tubes’, *Journal of Fluid Mechanics* **25**(04), 821.

6

Interaction between two consecutive axisymmetric Taylor drops flowing in a heavier liquid in a vertical tube

Authors' version of:

Direito, F. J. N., Campos, J. B. L. M. and Miranda, J. M. (2017), 'Interaction between two consecutive axisymmetric Taylor drops flowing in a heavier liquid in a vertical tube', *International Journal of Heat and Fluid Flow* **68**, 1-12.

Abstract

A study regarding the interaction between two consecutive Taylor drops flowing in a heavier liquid in a vertical tube is reported. Under certain conditions, due to the wake of the leading drop, the trailing drop accelerates, leading to coalescence of the two drops. This study was developed using a numerical model based in the Volume of Fluid method in an axisymmetric geometry. The simulations reported in the present work had to fulfill two conditions: axisymmetry (due to the numerical model) and a high enough drop Reynolds number (which is related to the disturbances in the wake of an isolated drop, and thus to the tendency to drop interaction). Relevant dimensionless numbers are used to assess the effect of the acting forces. Detailed flow patterns and drop shapes are provided. Furthermore, the approaching velocity acquired by the trailing drop is analyzed and velocity profiles between the leading and the trailing drop are also reported. In general, the trailing drop shows an accelerating region, followed by a deceleration near the leading drop. The increase of Eotvos number promotes higher accelerations, while the increase in Morton number and viscosity ratio has the opposite effect. By comparison to literature gas-liquid studies, it was also found that interfacial forces promote the shape stability of the drops.

6.1 Introduction

One of the foremost multiphase flow patterns is slug flow. Slug flow can be summarized as a flow pattern in which the dispersed phase forms long and large bullet-shaped drops or bubbles (Taylor bubbles or drops (Davies and Taylor, 1950, Govier and Aziz, 1972, Mandal et al., 2008)), flowing surrounded by the continuous phase (Fabre and Line, 1992). Earlier studies on slug flow concern gas-liquid phases (Davies and Taylor, 1950, Moissis and Griffith, 1962, Nicklin et al., 1962, White and Beardmore, 1962). Slug flow can occur in macro (gravity effects) (Mydlarz-Gabryk et al., 2014) or in micro tubes (no gravity) (Aoki et al., 2011, Jovanović et al., 2011). Slug flow can also appear in three phase flows, with a dominant liquid phase, and two other phases in drops and bubbles (Oddie et al., 2003, Liu et al., 2014).

The present work deals with vertical liquid-liquid slug flow with gravity effects.

Gas-liquid slug flow (Davies and Taylor, 1950, Nicklin et al., 1962, Morgado et al., 2016) is a well-known flow pattern, impelled by its importance in industrial applications, such as: vapor liquid absorbers, core cooling of nuclear reactors, reboilers and buoyance driven fermenters. Liquid-liquid slug flow has been observing an increase of interest due to its potential applications for example, in the petroleum industry (Hasan and Kabir, 1990, Bannwart et al., 2004, Mandal et al., 2010, Zhang et al., 2012).

Unlike gas-liquid though, liquid-liquid slug flow is still a pattern not well known. In order to gain a deeper knowledge of liquid-liquid slug flow, one must study the phenomenon step by step. The simpler approach is to analyze the flow of a single Taylor drop (dispersed phase) rising in a stagnant heavier liquid (continuous phase) in a vertical tube (Brown and Govier, 1961, Govier et al., 1961, Zukoski, 1966, Direito et al., 2016). The Taylor drop, in such conditions, reaches its terminal velocity (V_T), while the heavier liquid is forced, by the drop upward flow, to flow downwards (referential attached to the drop) in the narrow space between the drop and the wall, creating a thin annular film. Three regions of the continuous phase are of interest: the region above the drop ("I" in Figure 6.1), the film region ("II") and

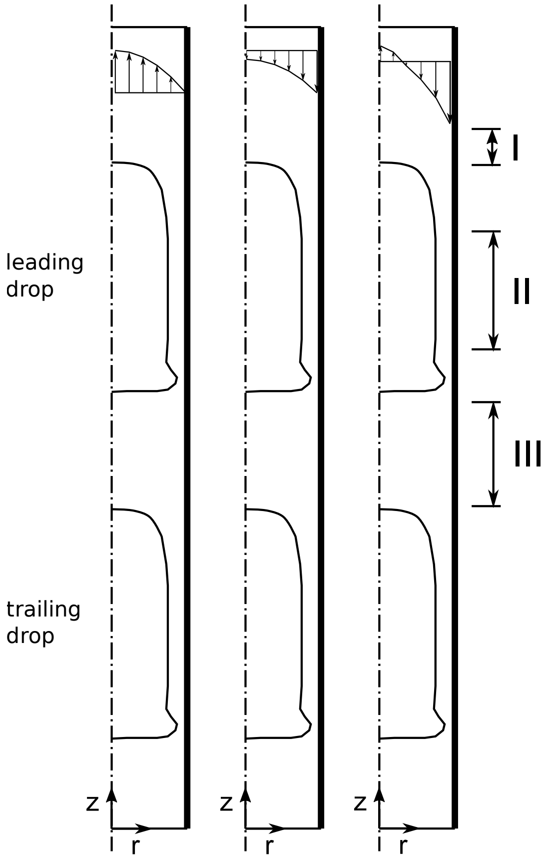

Figure 6.1: Axisymmetric domain with two drops. Velocity profiles: earth reference frame (left), leading drop nose reference frame for drops faster than undisturbed continuous phase (middle) and leading drop nose reference frame for drops slower than portions of undisturbed continuous phase (right). Marked region above the drop (I), leading drop continuous phase film (II) and leading drop wake (III).

the region below the drop ("III").

Concerning an isolated Taylor drop rising in a stagnant liquid, Mandal et al. (2007, 2008, 2009) studied the shape and velocity. Hayashi et al. (2011) presented experimental drop shapes as well as a dimensional analysis and data from numerical simulations. Kurimoto et al. (2013) also presented a correlation to predict the terminal velocity of Taylor drops rising in vertical tubes.

The aim of the present work is to analyze the flow behavior, drop shape and velocity when a trailing drop approaches a leading one flowing at its terminal velocity. The data was obtained by conducting numerical simulations (Computational Fluid Dynamics – CFD) using a two-dimensional axisymmetric model (Direito et al., 2016) and using, as starting point, previous simulations and experimental data regarding isolated Taylor drops flowing in stagnant (Direito et al., 2016) and co-current (Direito, Campos and Miranda, 2017) heavier liquid.

6.2 Physical background

In many applications, slug flow occurs in co-current flow. The behavior of single Taylor drops in liquid-liquid co-current flow was analyzed in a previous work (Direito, Campos and Miranda, 2017).

However in continuous liquid-liquid slug flow, consecutive Taylor drops interact with each other, leading to drop coalescence and the formation of longer drops. It is therefore relevant to describe the continuous liquid-liquid slug flow reformulating the terms previously stated for single Taylor drops (Direito et al., 2016). A dimensional analysis can be performed on the phenomena (Hayashi et al., 2011), in which it is important to consider the density ratio

$$\rho^* = \frac{\rho_\mathrm{D}}{\rho_\mathrm{C}}, \tag{6.1}$$

as well as the viscosity ratio

$$\mu^* = \frac{\mu_\mathrm{D}}{\mu_\mathrm{C}}, \tag{6.2}$$

where ρ is the density and μ the viscosity. The subscripts "D" and "C" refer to the dispersed and continuous phases. The density difference, $\Delta\rho = \rho_\mathrm{C} - \rho_\mathrm{D}$, also appears in some dimensionless numbers. Note also that the density ratio is always smaller than 1, as the present work deals with rising drops.

The ratio between inertial and gravity forces is represented by the Froude number, which is the dimensionless number usually used to quantify the drop terminal velocity:

$$\mathrm{Fr} = \frac{V_\mathrm{T}}{\sqrt{\Delta\rho\, gD/\rho_\mathrm{C}}}. \tag{6.3}$$

The ratio between buoyancy and interfacial forces is of foremost importance and is represented by the Eötvös number:

$$\mathrm{Eo} = \frac{\Delta\rho\, gD^2}{\sigma}, \tag{6.4}$$

with σ standing for the interfacial tension between the continuous and the dispersed phase.

Morton number balances gravitational, viscous and surface tension forces:

$$\mathrm{M} = \frac{\Delta\rho\, g\mu_\mathrm{C}^4}{\rho_\mathrm{C}^2\,\sigma^3}. \tag{6.5}$$

The combined analysis of Morton, Eötvös and viscosity ratio numbers is an important tool to inspect the flow behavior. When Eötvös number is high, i.e. low interfacial tension, and the viscosity ratio is low enough, the liquid-liquid isolated drop flow should resemble the flow of a gas Taylor bubble rising in a liquid in a macro tube. Such behavior is explained by the predominance of the gravity effect, i.e., by the large density difference. For low Eötvös, Morton number is required to quantify the importance of the viscous forces. Low Eötvös and high Morton numbers implicate a high viscosity of the continuous phase. If the viscosity ratio is high, such combination should be observed when, at the macro-scale, both fluids have close densities (viscous effects predominance). For low Eötvös and Morton numbers and low viscosity ratio, the flow should resemble that of a gas Taylor bubble flowing in a liquid contained in a micro tube (interfacial tension predominance) (Rocha et al., 2017).

In order to avoid confusion between the terminal velocity and the drop velocity in continuous co-current flow, the terminology V_TC will be used for the co-current drop velocity and V_T for the terminal velocity. Notice the following relationship between both (Fabre and Line, 1992, Nicklin et al., 1962):

$$V_\mathrm{TC} = V_\mathrm{T} + CU_\mathrm{C}, \tag{6.6}$$

where C is a constant that depends on the flow properties (Direito, Campos and Miranda, 2017) and U_C is the superficial velocity of the continuous phase when the superficial velocity of the dispersed phase is zero as is the case of the present study. Furthermore, the ratio between the superficial velocity and the drop terminal velocity can be used:

$$u^{*} = \frac{U_{\mathrm{C}}}{V_{\mathrm{T}}}. \tag{6.7}$$

If equation 6.6 is divided by V_{T}:

$$\frac{V_{\mathrm{TC}}}{V_{\mathrm{T}}} = 1 + C u^{*}. \tag{6.8}$$

Even though the presented dimensionless numbers suffice (eq. 6.1, 6.2, 6.3, 6.4 and 6.5) for the characterization of the problem, it is also useful to consider the ratio between inertial and viscous forces in the continuous phase regarding the disturbance caused by the drop passage in the continuous liquid which is represented by the drop Reynolds number,

$$\mathrm{Re}_{\mathrm{D}} = \frac{\rho_{\mathrm{C}}\, V_{\mathrm{T}}\, D}{\mu_{\mathrm{C}}}, \tag{6.9}$$

for stagnant continuous phase and

$$\mathrm{Re}_{\mathrm{D}} = \frac{\rho_{\mathrm{C}}\, V_{\mathrm{TC}}\, D}{\mu_{\mathrm{C}}}, \tag{6.10}$$

for co-current flow. This Reynolds number is determinant on the stabilization of the continuous phase below an isolated drop (Direito, Campos and Miranda, 2017).

However, when two drops rise close, the trailing drop achieves speeds that are higher than the corresponding velocity in a stabilized flow. Thus another velocity variable V_{D} must be introduced to account for the trailing drop speed.

The coalescence of two Taylor bubbles (gas-liquid) has been the subject of several experimental (Moissis and Griffith, 1962, Pinto and Campos, 1996) and numerical studies (Araújo et al., 2013*b*, 2015) and, due to the lack of liquid-liquid coalescence studies, serve as comparison to the present work results.

One of the most important parameter to analyze the coalescence in slug flow is the velocity that the trailing drop acquires when it approaches the leading one. In order to capture the essence of this feature, one must define a reference distance between the two drops, measured in the tube axis. The obvious choice for the trailing drop falls in the drop nose. Regarding the leading drop, Araújo et al. (2013*a*) analyzed two possibilities: the nose and the tail. Because, in some conditions, the leading drop may undergo shape changes (periodic oscillations), Araújo et al. (2013*a*) chose the leading drop tail to be a more reliable option. Araújo et al. (2013*a*) further observed that the approaching movement can have an accelerating period and then a decelerating one (occurring when the two drops are close to each other). For the acceleration region, Araújo et al. (2013*a*) proposes for the trailing velocity an exponential relationship with the distance between the drops (tail of the leading and nose of the trailing):

$$\frac{V_{\mathrm{D}}}{V_{\mathrm{T}}} = 1 + a_a\, e^{-b_a (-d')}, \tag{6.11}$$

where a_a and b_a are fitting parameters. The variable d' stands for the distance between the drops:

$$d' = -\,\frac{\text{distance between drops}}{D}. \tag{6.12}$$

The value of the distance between the drops is defined as negative, as it is the "lag" that the trailing bubble has towards the leading drop. Hence $d' < 0$. Note that $d' = 0$ corresponds to the exact moment when the interfaces touch. (Araújo et al., 2013*a*) also suggests a correlation for the deceleration region:

$$\frac{V_{\mathrm{D}}}{V_{\mathrm{T}}} = \sqrt{a_d + b_d\,(-d') + c_d\,(-d')\,(\ln{(-d')} - 1)}, \tag{6.13}$$

where a_d, b_d and c_d are the fitting parameters.

Concerning the coalescence of two Taylor drops (liquid-liquid), some important information can be extracted from analyzing the flow below an isolated drop. Direito, Campos and Miranda (2017) related the normalized stabilization length,

$$Z_{\mathrm{III}} = \frac{\text{stabilization distance}}{D}, \tag{6.14}$$

with the dispersed phase Reynolds number, observing that $\mathrm{Re_D}$ can be used to predict the behavior of the region below the drop, either in stagnant or flowing continuous phase. The stabilization length was evaluated by considering, in the tube axis, the distance from the drop tail needed for the axial velocity component to be less than 5 % from the undisturbed value.

Direito, Campos and Miranda (2017) showed two different regimes, regarding this feature. For low Reynolds number values, $\mathrm{Re_D} < 10$ no closed recirculations are observed at the drop bottom. At such conditions, the coalescence of two drops is unprovable because the recovery of the velocity profile below the drop takes an extremely short distance. At $\mathrm{Re_D} > 100$, closed recirculations below the leading drop start to appear and the stabilization length starts increasing dramatically. In such conditions, coalescence of two consecutive drops is expected.

In the present work, the conditions simulated with most interest had to fulfill two conditions: axisymmetry (due to the computational resources limitations) (Direito et al., 2016, Direito, Morgado, Rocha, Miranda and Campos, 2017) and a sufficiently high drop Reynolds number (Direito, Campos and Miranda, 2017) – Figure 6.2 (Kurimoto et al., 2013, Direito et al., 2016, Direito, Morgado, Rocha, Miranda and Campos, 2017). Therefore, at two dimensions, coalescence will occur in the region with $\mathrm{Eo} > 20$, $\log M < 0$ and $\mu^* > 1$, which is the scope of this study.

6.2.1 Numerical model

The physical model implemented in the present work follows the one already used in the research group (Direito et al., 2016).

An Ansys Fluent multiphase laminar incompressible flow model integrated with Volume of Fluid (VOF) method (Hirt and Nichols, 1981) was used. The interface is determined by geometric reconstruction (Youngs, 1982) ("Geo-reconstruct" in the software package) which can be summarized in three steps: determination of the slope for an interface within the cell based on the liquid volume fractions; computation of the momentum transport by advection through each face by using the created linear interface and the face velocity components; and determination of the new cell volume fractions balancing the advection fluxes. Regarding pressure-velocity coupling, a segregated algorithm PISO (Issa, 1986) was used, a non-iterative algorithm, which splits the solution into predictor and corrector steps. The scalar gradients were computed by the Green-Gauss node-based method. For pressure interpolations, a pressure staggering option scheme was chosen (Patankar, 1980) – "Presto!" in the software package. The QUICK (Leonard, 1979) scheme was used for solving the momentum equations. To account for the interfacial forces, the Continuum Surface Force model (Brackbill et al., 1992) was applied. It creates the interface between the two liquids as a transition region of finite thickness where the surface tension force term is proportional to the curvature in each location. Outside the interface, this force term is zero. A first order

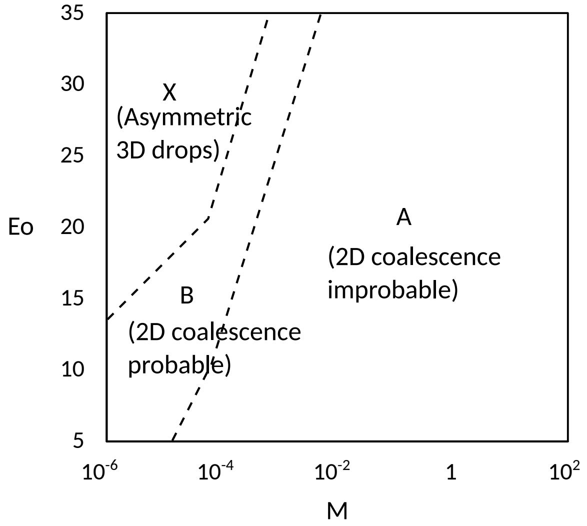

$\mu^* = 1$

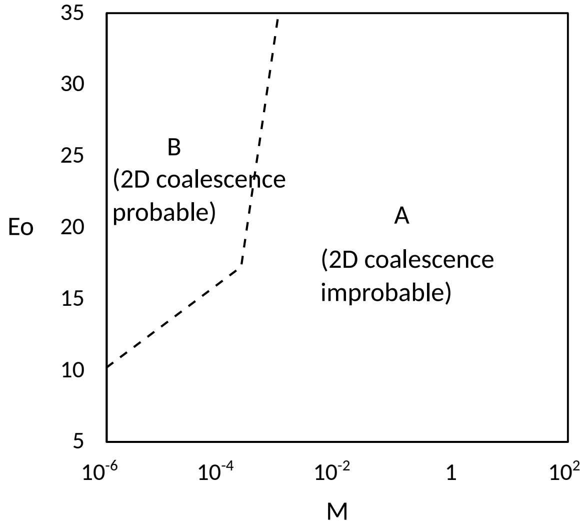

$\mu^* = 10$

Figure 6.2: Coalescence and non-coalescence regions, with non-axisymmetric region (X) and axisymmetric regions (A for $\mathrm{Re_D} < 10$ and B for $\mathrm{Re_D} > 10$).

implicit scheme was used for time discretization with a maximum Courant number of 0.25.

In order to deal with the two-phase flow, a variable α_i is defined. The value of α_i is 1 at any point occupied exclusively by the fluid i, 0 if no i exists there, or a number between 0 and 1, if both fluids exist in the same mesh element:

$$\alpha_C + \alpha_D = 1. \tag{6.15}$$

Note that cells with $\alpha_\mathrm{D} \neq 0 \wedge \alpha_\mathrm{D} \neq 1$ represent the interface between the two liquids. On such cells, density and viscosity are computed supposing linear contributions of each phase. For the purpose of flow analysis, the interface was located at $\alpha = 0.5$.

A 2D domain is represented in Figure 6.1 since axial symmetry (around the cylinder axis) – axisymmetry – holds for the present study. When concerning Taylor bubbles and drops, this approach has been widely used and observed, both in theoretical (Collins et al., 1978, Mandal et al., 2007), experimental (Davies and Taylor, 1950, White and Beardmore, 1962, Mandal et al., 2008, Araújo et al., 2012) and numerical studies (Hayashi et al., 2011, Kurimoto et al., 2013, Araújo et al., 2013*b*). The domain consisted of a rectangle with a width $D/2$ and 16.5 D long. The mesh consisted of a 52×1720 grid of quadrilateral and uniformly distributed cells. The mesh and numerical model were validated in previous works (Direito et al., 2016, Direito, Campos and Miranda, 2017).

A moving reference frame attached to the leading drop was used (Direito et al., 2016). In this reference frame, the drop is at rest and the continuous phase and the tube wall are moving downwards. The wall velocity boundary condition was set to the value of the drop terminal velocity. Moreover, an inlet flow boundary condition (at the top of the domain) was imposed. In the present work, two velocity boundary conditions were used. A downward uniform velocity (equal to V_T) is imposed when simulating the stagnant continuous phase. For the co-current case, the velocity profile at the inlet consists of the laminar parabolic profile subtracted by the drop velocity:

$$u(r) = -V_\mathrm{TC} + 2\,U_\mathrm{C}\left(1 - (2r/D)^2\right), \tag{6.16}$$

where r is the radial coordinate. This profile was implemented through an "user defined function" in Ansys Fluent. At the tube exit, pressure was set to zero gauge.

Simulations were initialized using the drop shape and velocity field from the corresponding stagnant case(Direito et al., 2016) or co-current case (Direito, Campos and Miranda, 2017). Afterwards, the drop and velocity fields are replicated at a relevant distance below the original drop. The simulation then runs until the two drops coalesce. Note that the phenomena analyzed concerns the approximation of the two drops, being the contact and merge of the interfaces outside the scope of this work.

6.3 Results

A study was performed, for a set of different flow conditions, using the numerical model presented in Section 6.2.1. The set of conditions was based on dimensionless numbers in order to identify the relative role of the forces involved. A total of five simulations were performed using a stagnant continuous phase (Table 6.1). Results from a previous work (Direito et al., 2016) were used as the starting conditions. Three simulations were run with a co-current flowing continuous phase (Table 6.2), based on simulations reported in (Direito, Campos and Miranda, 2017). The number in the simulations code refers to the u^* value. Following the cited works, the simulations were all run with $\rho^* = 0.792$. This value of the density ratio lies in the common range for liquid-liquid studies (Hayashi et al., 2011, Mandal et al., 2009).

Table 6.1: Simulation conditions with stagnant continuous phase.

id.	Eo	M	μ^*	max Re'_D
A	22	2.32×10^{-6}	10	50
B	30	2.32×10^{-6}	2	129
C	30	2.32×10^{-6}	3	112
D	30	2.32×10^{-6}	10	90
E	22	1×10^{-4}	10	11

Table 6.2: Simulation conditions with flowing co-current continuous phase.

id.	Eo	M	μ^*	u^*	max Re'_D
A2	22	2.32×10^{-6}	10	2	197
A5	22	2.32×10^{-6}	10	5	473
F2	8	100	10	2	1.9×10^{-3}

Moreover, a ratio of 1.147 between the drop volume-equivalent sphere diameter and the tube diameter was used (as reported in Direito et al. (2016) and Direito, Campos and Miranda (2017)).

Figures 6.3, 6.4 and 6.5 present the shapes and flow patterns for all the runs. Four instants are shown for each simulation. The first one ("t1" in Figures 6.3, 6.4 and 6.5) is a snapshot taken at an early stage while the second ("t2") is taken at a midpoint of the approaching path. Literature data (Araújo et al., 2013*b*,*a*, 2015) indicate that, in some flow conditions, there can be significant shape deformation when the drops are very close to each other. Therefore, the last two snapshots ("t3" and "t4") were taken just before coalescence.

Another important feature of the flow concerns the velocity profile between the two drops. Figure 6.6 presents the axial velocity profile (normalized by the leading drop velocity) along the tube axis, in the region between the leading drop tail and the trailing drop nose, for four different conditions.

Simulation data do not provide directly the trailing drop velocity. Instead, one must firstly track the position of the trailing drop nose throughout time. In order to obtain this velocity, the derivative of the position in order to time must be computed. Hence, the data were obtained using a second-order polynomial Lagrange interpolation, adequate for unequally spaced data (Chapra and Canale, 2006).

Even though the range where drops are axisymmetric (refer to Direito et al. (2016), Direito, Morgado, Rocha, Miranda and Campos (2017)) and, at the same time, likely to undergo coalescence is narrow (Figure 6.2), it was still possible to study the effect of the different relevant dimensionless numbers. The following subsections present flow data isolating the effect of each relevant dimensionless number.

6.3.1 No coalescence

In conditions with a small drop Reynolds number, two consecutive drops do not interact and, hence, do not approach each other and coalesce. An example of such behavior regards a simulation preformed at $\mathrm{M} = 100$, $\mathrm{Eo} = 8$, $\mu^* = 10$ and $u^* = 2$. In these conditions, the drop Reynolds number is 1.9×10^{-3}. Figure 6.7 presents the flow regarding those conditions. In this example, even an initial positioning of the trailing drop at $Z'/D = 0.2$ does not cause the two drops to coalesce.

6.3.2 Co-current effect

In order to evaluate how the continuous phase velocity can influence the coalescence, take into consideration simulations run under $\mathrm{M} = 2.32 \times 10^{-6}$, $\mathrm{Eo} = 22$ and $\mu^* = 10$ conditions. Figure 6.8 shows the relative velocity of the trailing drop as it approaches the tail of the leading one.

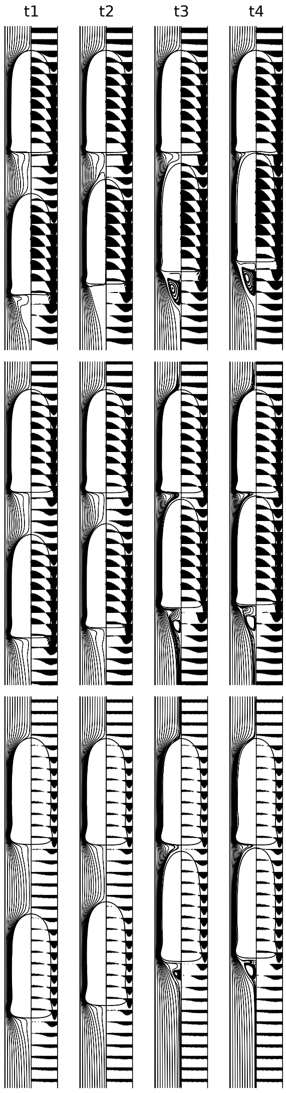

Figure 6.3: Viscosity ratio effect on velocity field and streamlines (leading drop reference frame) for Eo = 30 and M = 2.32×10^{-6}: $\mu^* = 2$ (top), $\mu^* = 3$ (middle), $\mu^* = 10$ (bottom), .

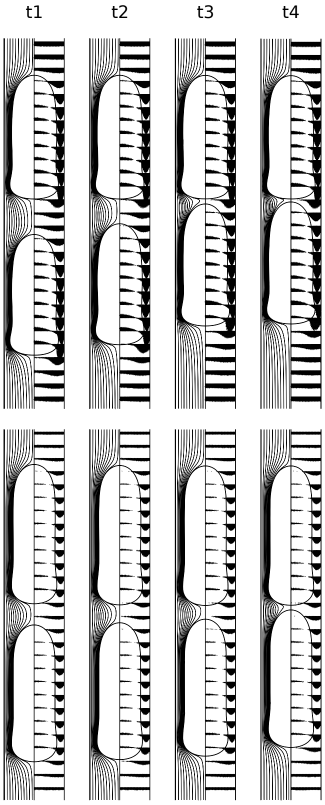

Figure 6.4: Morton number effect on velocity field and streamlines (leading drop reference frame) for Eo = 22 and $\mu^* = 10$, M = 2.32×10^{-6} (top) and M = 10^{-4} (bottom).

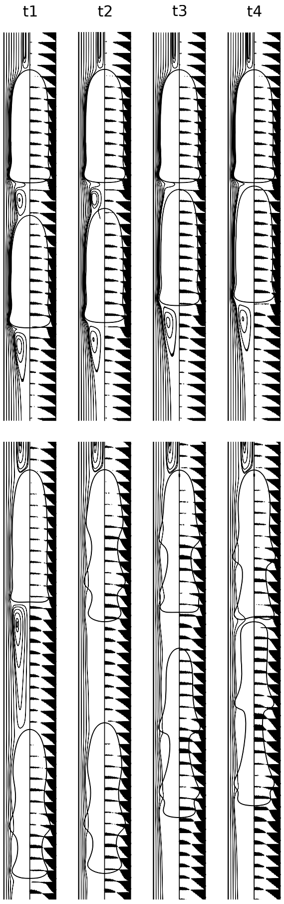

Figure 6.5: Velocity field and streamlines (leadind drop reference frame) with Eo $= 22$, M $= 2.32 \times 10^{-6}$ and $\mu^* = 10$. Top: $u^* = 2$. Bottom: $u^* = 5$.

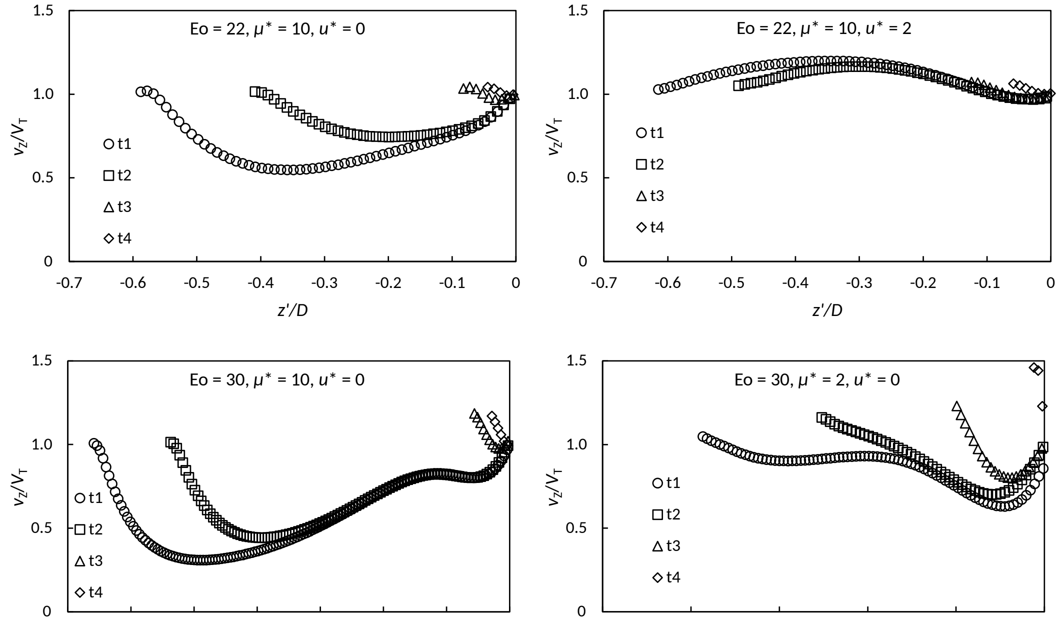

Figure 6.6: Axial velocity profile along the axis between the two drops for M $= 2.32 \times 10^{-6}$.

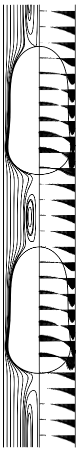

Figure 6.7: Velocity field and streamlines (leadind drop reference frame) for M = 100, Eo = 8, $\mu^* = 10$ and $u^* = 2$.

In the stagnant case ($u* = 0$), the trailing drop velocity increases linearly with distance. Near the leading drop, the trailing drop undergoes a small and short deceleration. The small acceleration is consistent with the behavior that Araújo et al. (2013*a*) reported for small Morton and Eötvös numbers. The small relative velocity observed during the acceleration period (notice that $V_\mathrm{D}/V_\mathrm{T} < 1.05$ all the time) is consistent with the almost undetectable drop shape deformation observable in Figure 6.4.

An overview on the continuous phase streamlines and velocity field (Figure 6.4) further supports the idea of almost undisturbed flow. Detail on the continuous phase flow near the trailing drop can give further information. Following the previous observations, it is not surprising that the velocity profile in the film (which is related to drop shape and velocity) keeps unchanged through the entire approach. Figure 6.9 shows the profiles in the film which are almost overlapped. As reported in Direito et al. (2016), the present profile shows, near the interface, an upward flow. This is due to the high shear forces related to the high viscosity of the dispersed phase. Moreover, the maximum downward velocity is not located at the interface, as it happens in gas-liquid flows.

Differences appear, though, for the velocity profile in a radial line passing the trailing drop nose (Figure 6.10). In an overview, the profile is consistent with a downwards flow near the wall, corresponding to fluid that is being pushed to give room for the trailing drop flowing upwards. Far from the wall, the effect of the drop pushing upwards liquid close to it gains preponderance. At $r/D = 0$ the velocity of the continuous phase matches the drop velocity. The general trend of these profiles is consistent with all the previous gas-liquid and liquid-liquid knowledge on the subject (Brown and Govier, 1961, Fabre and Line, 1992, Mandal et al., 2007, Direito et al., 2016, Morgado et al., 2016). The profile configurations found for the instants “t3” and “t4” (drops near each other) are related to the effect of the small jets in the tail of the leading drop promoted by the narrow passage of the liquid film flowing around. Because of that, there is a visible increase in the downward flow velocity near the wall. In order to compensate this downwards flow, at about $r/D = 0.35$ the axial velocity acquires an upward value which is higher than the observed in “t1” and “t2”. The radial component data are consistent with the behavior of the axial data. When the drops are far from each other (“t1” and “t2”), the radial component point towards the wall due to the drainage of the continuous phase occurring between the drops. At instants “t3” and “t4”, the leading drop jet forces the portions of continuous phase closer to the wall to have an inward direction. Closer to the tube axis, it is observable a region where the radial component points apart from the axis, corresponding to the drainage of the fluid that is between the drops. Increasing the continuous

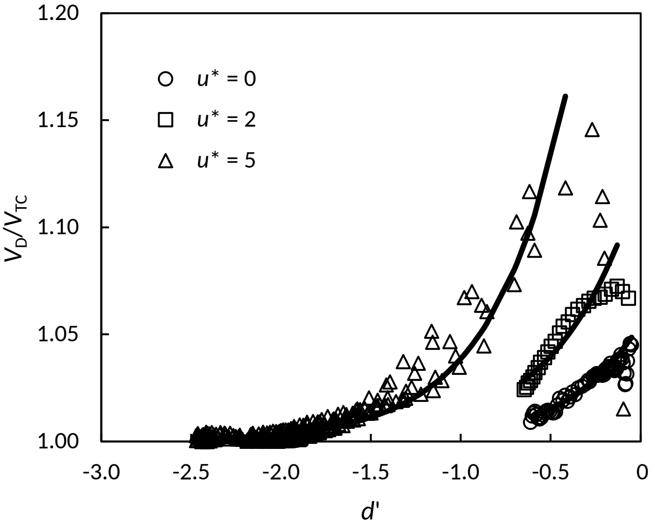

Figure 6.8: Trailing drop velocity for different co-current velocities for $\mathrm{M} = 2.32 \times 10^{-6}$, $\mathrm{Eo} = 22$ and $\mu^* = 10$ and fitting curves (black lines).

phase velocity (Figure 6.8), the fluid passing in the film has a higher velocity than the portions of liquid below the leading drop, and the jet exiting the film causes increasingly longer perturbations on the flow below.

At $u^* = 2$, the velocity curve (Figure 6.8) has an acceleration region followed by a small deceleration region. Such behavior is similar to that reported by Araújo et al. (2013*a*). At $u^* = 5$, the acceleration region is longer. Note that, at $u^* = 5$, both drops show shape deformations during the instants immediately before coalescence (Figure 6.5 – middle). Because of that, when drops are close to each other, drops distance, d', oscillates as seen in Figure 6.8.

In order to physically understand the interaction behavior for continuous liquid flow, recall the top and middle simulations presented in Figure 6.5. At $u^* = 2$, two flow patterns occur in the continuous phase (reported in Direito, Campos and Miranda (2017)): semi-infinite circulation streamlines ahead the leading drop and a closed recirculation behind, i.e., ahead the trailing drop. The presence of the closed recirculation accelerates, both the fluid coming from the film of the leading bubble (in the downwards direction in a referential attached the trailing bubble) and, by continuity, the liquid flowing near the tube wall ahead the trailing bubble (in the upwards direction). This accelerated liquid near the tube axis is responsible for the acceleration of the trailing drop. This acceleration only stops when the nose of the trailing drop is well inside the close wake of the leading one. The volume of this wake diminishes with the approximation of the trailing drop (Figure 6.5). From then on, the trailing drop decelerates and in a short period the drops coalesce.

This effect of the close recirculation below the leading drop can be further observed by analyzing the data regarding the axial velocity profile along the axis between the two drops (Figure 6.6). For the stagnant case ($\mathrm{M} = 2.32 \times 10^{-6}$, $\mathrm{Eo} = 22$ and $\mu^* = 10$), the axial velocity decreases below the leading drop tail, and increases again near the trailing drop. On the other hand, at $u^* = 2$, due to the closed recirculation in the flow the axial velocity between the two drops is higher than the velocity of the leading drop.

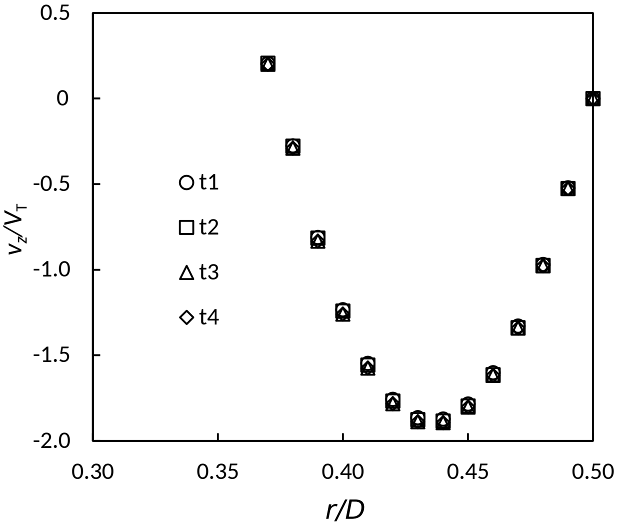

Figure 6.9: Axial velocity profile in the developed film around the trailing drop for stagnant continuous phase (M $= 2.32 \times 10^{-6}$, Eo $= 22$ and $\mu^* = 10$)

6.3.3 Morton number effect

The influence of the Morton number on the coalescence can be assessed by comparing the stagnant simulation at M $= 2.32 \times 10^{-6}$, Eo $= 22$ and $\mu^* = 10$, analyzed in Section 6.3.2, with that at M $= 10^{-4}$, Eo $= 22$ and $\mu^* = 10$. The resulting trailing drop velocities are compared in Figure 6.11. Like it was observed before for the M $= 2.32 \times 10^{-6}$ simulation, the M $= 10^{-4}$ profile shows an accelerating region but this starts at a much shorter distance from the tail of the leading drop, because of the shorter length required for the stabilization of the velocity in the fluid coming from the leading drop film. This effect of Morton number is consistent with the literature for gas-liquid (Araújo et al., 2013*a*).

Regarding M $= 10^{-4}$ (Figure 6.4) the trailing drop shape, is much more elongated due to the increased Morton and the liquid film flowing around the leading drop much more thicker. Moreover, the leading drop shape does not undergo visible deformation in the proximity of the trailing drop.

The elongation of the drop due to the increase in the Morton number reduces the jet-like effect due to the narrowing at the bottom of the leading drop (observe in Figure 6.4 the lessen of the bell-shaped drop bottom). Hence, the velocity profile in the horizontal line passing the trailing drop nose is less disturbed (Figure 6.12). The approaching of the two drops (in instant “t3”) affects slightly the radial profile, but it is only in the most close state (“t4”) that the inversion of the radial component closer to the wall takes place. Near the axis, the effect of the drainage of the continuous phase between the drops is still observed. Regarding the axial component, at the instant “t4” the influence of the leading drop film exit is small, with a slightly increased downward velocity near the wall, and a compensation (in the upwards direction) for radii below 0.35.

6.3.4 Eötvös number effect

The Eötvös number balances buoyancy and interfacial forces and has a strong influence in slug flow (Morgado et al., 2016). Figure 6.13 compares the trailing drop velocity for two cases with different Eötvös number values and constant M $= 2.32 \times 10^{-6}$ and $\mu^* = 10$. The increase of Eötvös number (decrease of interfacial forces in relation to buoyancy) causes an increase in the normalized trailing drop

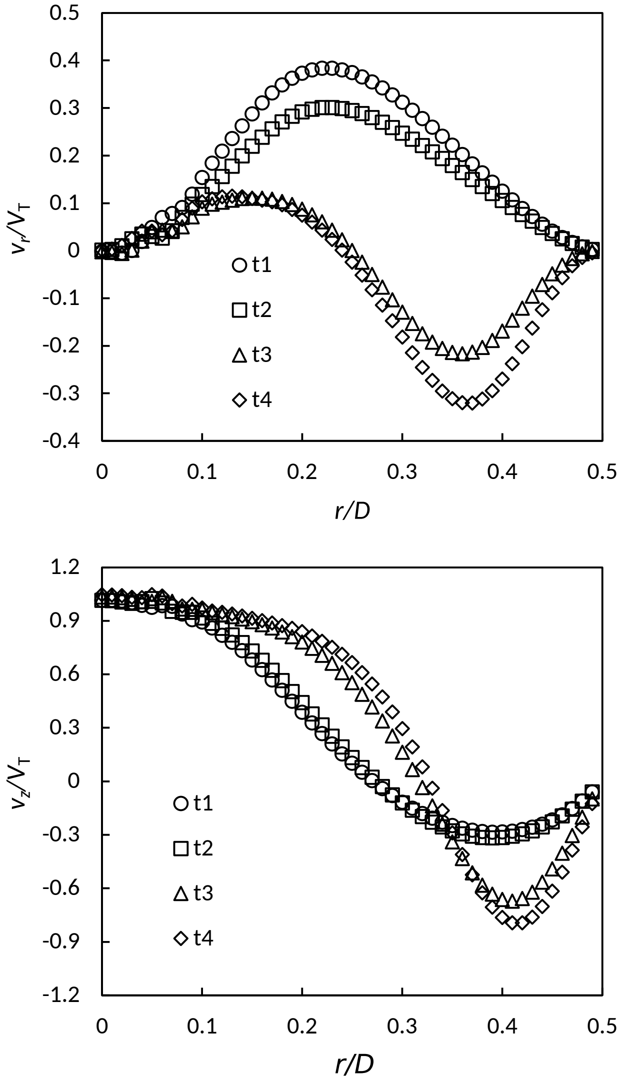

Figure 6.10: Velocity profile along radial direction from the trailing drop nose for stagnant continuous phase (M = 2.32×10^{-6}, Eo = 22 and $\mu^* = 10$)

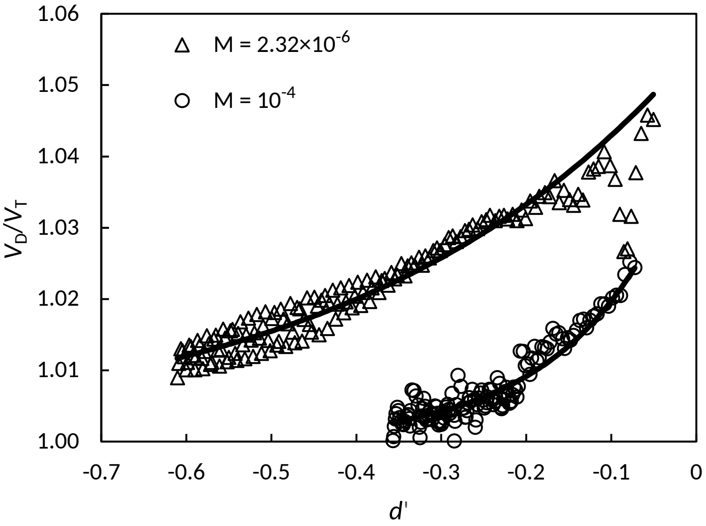

Figure 6.11: Trailing drop velocity for different Morton number values at Eo = 22 and $\mu^* = 10$ (stagnant) and fitting curves (black lines).

velocity (V_D/V_T). Furthermore, while at Eo = 22 the curve is almost a straight line with low slope, at Eo = 30 the acceleration region undergoes a significant increase at $d' = -0.5$ and has a deceleration region near the leading drop.

Velocity field and streamlines for the Eo = 30 case (Figure 6.3, bottom), show that at locations near the leading drop ("t3" and "t4"), a closed recirculation starts to appear in the wake of the trailing drop (see Table 6.1 for maximum drop Reynolds number, 90). As it was observed in liquid-liquid systems, the closed recirculations are "detached" from the drop, which keeps a slightly flatted rear.

Even though there are not any significant deformations on the trailing and leading drops body, unlike the Eo = 22 case, for Eo = 30 it is possible to observe a small change in the trailing drop length and radius (Figure 6.13). This implicates that a small effect should be observable in the film profile, which is confirmed by Figure 6.14.

6.3.5 Viscosity ratio effect

Using simulation Eo = 30, M = 2.32×10^{-6} and $\mu^* = 10$ as a starting point, one can analyze the influence of the viscosity ratio (Figure 6.3). The decrease in the viscosity ratio strengthens the effect of the closed recirculations. Hence, for the same continuous phase conditions, when the viscosity ratio is lower, the trailing drop velocity achieves a higher peak (Figure 6.16).

A small shape change is also observable at $\mu* = 2$ (Figure 6.17). Figure 6.18 presents the Axial velocity profile in the developed film.

Regarding the velocity in a horizontal line passing in the trailing drop nose, the case $\mu* = 2$ (Figure 6.19), shows greater axial velocity and smaller radial velocity than the $\mu* = 10$ case. At "t4", the radial velocity component has a peak near the tube center which points into the wall direction.

6.3.6 Further considerations

According to the conclusions in the previous sections, by increasing Eötvös number and decreasing Morton number, the trailing drop velocity achieves higher values (Figure 6.20).

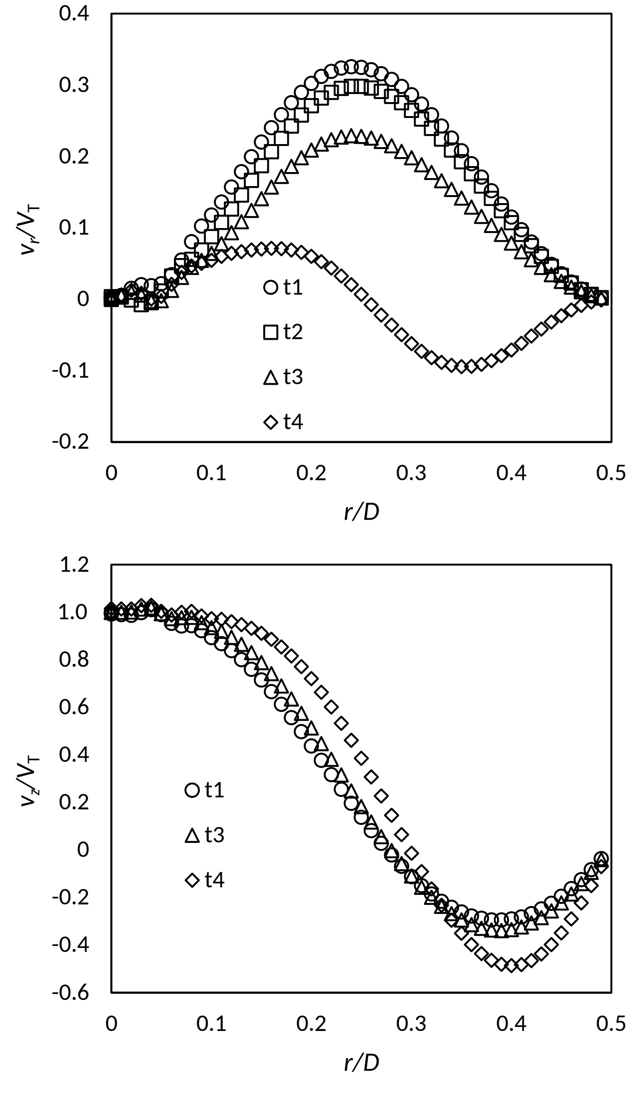

Figure 6.12: Velocity profile along radial direction from the trailing drop nose for stagnant continuous phase (M $= 10^{-4}$, Eo $= 22$ and $\mu^* = 10$)

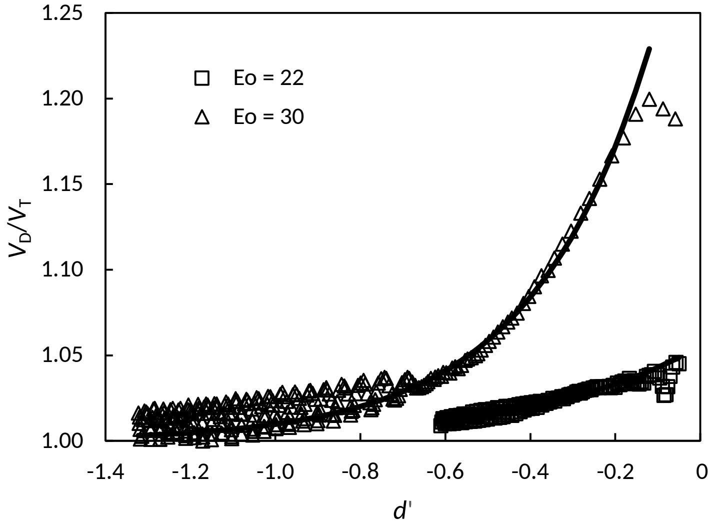

Figure 6.13: Trailing drop velocity for different Eötvös number values at M = 2.32×10^{-6} and $\mu^* = 10$ (stagnant) and fitting curves (black lines).

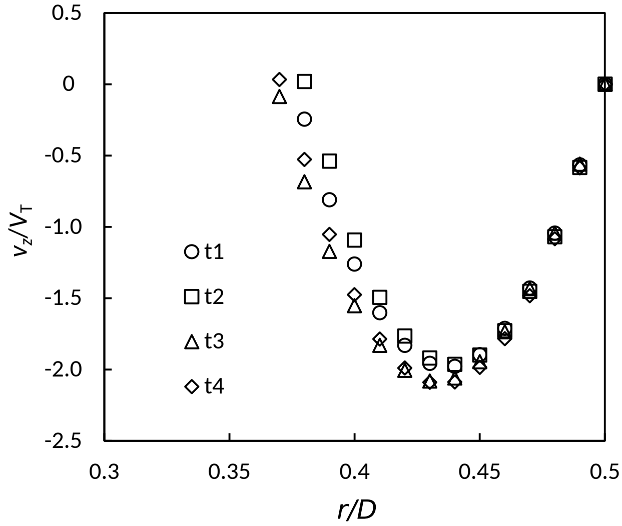

Figure 6.14: Axial velocity profile in the developed film around the trailing drop for stagnant continuous phase (M = 2.32×10^{-6}, Eo = 30 and $\mu^* = 10$)

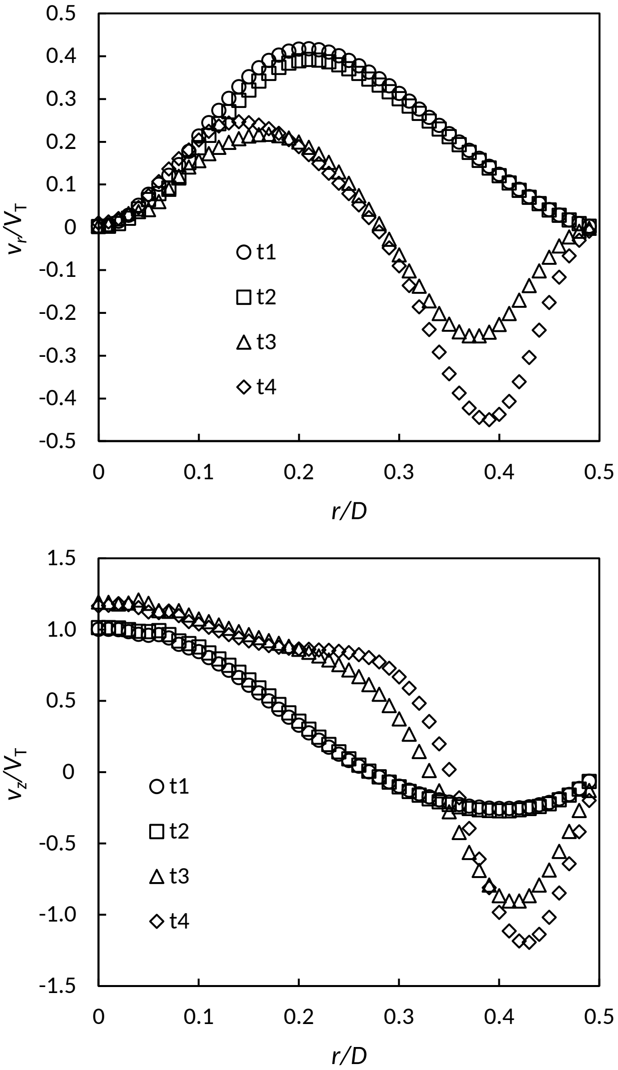

Figure 6.15: Velocity profile along radial direction from the trailing drop nose for stagnant continuous phase (M $= 2.32 \times 10^{-6}$, Eo $= 30$ and $\mu^* = 10$)

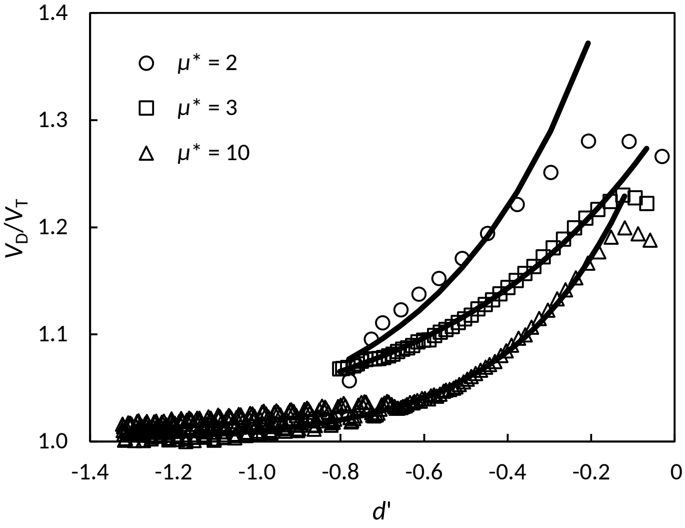

Figure 6.16: Trailing drop velocity for different viscosity ratio values at Eo = 30 and M = 2.32×10^{-6} (stagnant) and fitting curves (black lines).

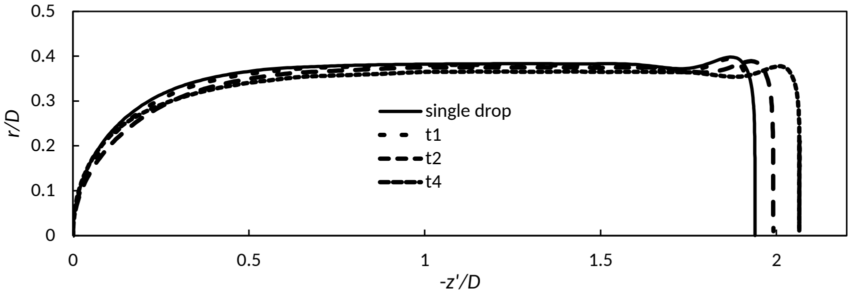

Figure 6.17: Trailing drop shape for stagnant continuous phase (M = 2.32×10^{-6}, Eo = 30 and $\mu^* = 2$)

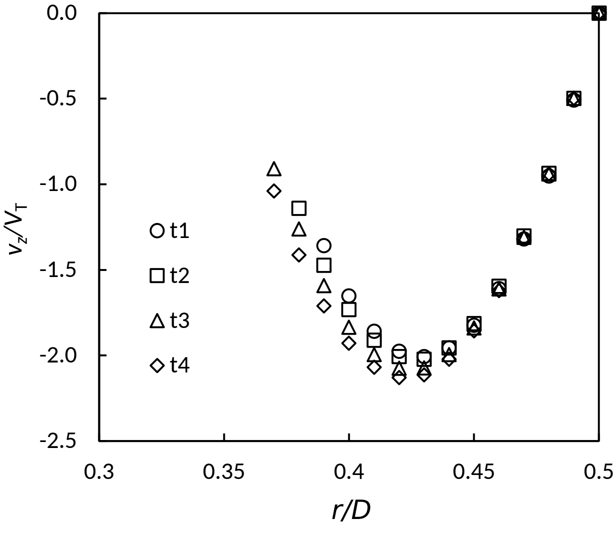

Figure 6.18: Axial velocity profile in the developed film around the trailing drop for stagnant continuous phase (M = 2.32×10^{-6}, Eo = 30 and $\mu^* = 2$)

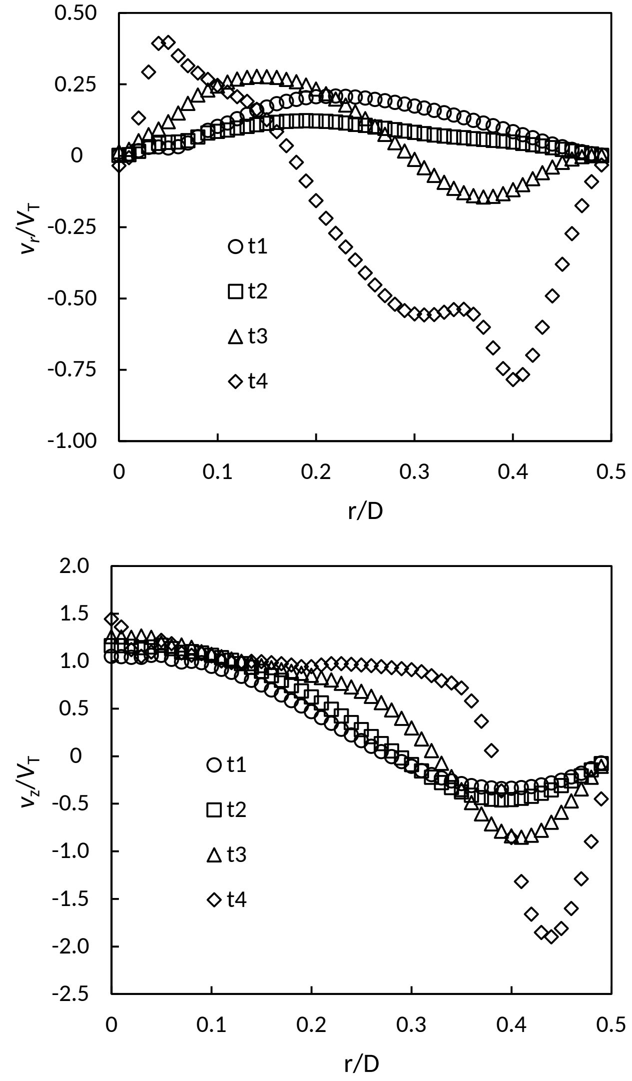

Figure 6.19: Velocity profile along radial direction from the trailing drop nose for stagnant continuous phase (M = 2.32×10^{-6}, Eo = 30 and $\mu^* = 2$)

Table 6.3: Accelerating region coefficients with stagnant continuous phase.

id.	Eo	$\log \mathrm{M}$	μ^*	a_a	b_a
A	22	2.32×10^{-6}	10	0.0554	2.55
B	30	2.32×10^{-6}	2	0.657	2.75
C	30	2.32×10^{-6}	3	0.312	1.95
D	30	2.32×10^{-6}	10	0.352	3.58
E	22	1×10^{-4}	10	0.0425	7.68

Table 6.4: Accelerating region coefficients with flowing co-current continuous phase.

id.	Eo	$\log \mathrm{M}$	μ^*	u^*	a_a	b_a
A2	22	2.32×10^{-6}	10	2	0.123	2.25
A5	22	2.32×10^{-6}	10	5	0.448	2.45

The trailing drop velocity results can be fitted by equation 6.11. Values for the coefficients are presented in Tables 6.3 (see also Figure 6.11, 6.13 and 6.16) and 6.4 (see also Figure 6.8).

At the conditions studied in the present work, small drop deformations were observed. In fact, in a previous study in gas-liquid (Araújo et al., 2013*a*), the gas bubble deformations were also very small for lower Eötvös number values (such as 34).

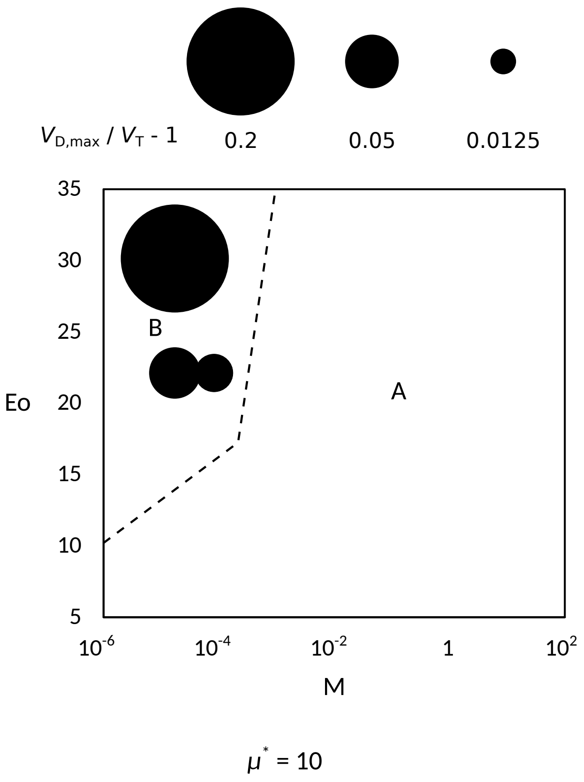

Figure 6.20: Coalescence and non-coalescence regions, with axisymmetric regions (A for $\mathrm{Re_D} < 10$ and B for $\mathrm{Re_D} > 10$), and maximum normalized trailing drop velocity.

6.4 Conclusions

The present study was conducted due to the increasing interest in multiphase flow. In particular, liquid-liquid slug flow is not yet fully understood. Therefore, a series of computer simulations were conducted to analyze the interaction of two Taylor drops near each other. On such occasions, the trailing drop is accelerated by the leading drop wake, leading to the coalescence of the two drops. The employment of a numerical model is of great interest due to the difficulties of analyzing the interaction experimentally.

The numerical model employed in the present work was based on a previously validated two-dimensional axisymmetric model for isolated Taylor drops. Previously studied stagnant and co-current systems with isolated Taylor drops served as the starting point for the simulations in the present work. The coalescence is highly influence by the wake of the leading drop. Within the valid range of the axisymmetric assumption, only a small region can undergo coalescence. Nevertheless, it was still possible to analyze the influence of the relevant dimensionless numbers: Eötvös number, Morton number and viscosity ratio. Furthermore, comparisons between stagnant and co-current continuous phase were also reported.

Detailed descriptions regarding the velocity field in the continuous phase were reported, as well as trailing drop velocity. This data includes instants when the drops are close to each other, which constitutes a significant success when compared to the limitations of the experimental techniques.

The velocity of the trailing drop (in respect to the leading drop velocity) was one of the flow features studied. An increase of Eötvös number (less interfacial forces, more buoyancy forces) causes an increase of the trailing drop velocity, while the increase in Morton number yields a decrease in the trailing drop velocity. These trends are in agreement to the gas-liquid trends reported in literature. Furthermore, the trailing drop velocity is increased by the decrease of the viscosity ratio and by the increase in the continuous phase velocity. The existence of closed recirculations below the leading drop has an important effect in accelerating the trailing drop.

The low trailing drop velocities achieved in most of the simulations performed (at most more 30 % than the isolated drop) and the limited Eötvös number (low when compared to gas-liquid – i.e. increased interfacial forces) yield leading and trailing drops that undergo only very small shape deformations when the drops coalesce.

The increase in the trailing drop velocity leads, in some conditions, to the formation or reinforcing of closed recirculations in the trailing drop wake.

Acknowledgements

This work was funded by FEDER funds through the Operational Programme for Competitiveness Factors COMPETE and National Funds through FCT (Fundação para a Ciência e a Tecnologia) under the project PEst-OE/EME/UI0532. Filipe Direito gratefully acknowledge the financial support from the FCT through Ph.D. Grant SFRH/BD/79264/2011.

References

Aoki, N., Ando, R. and Mae, K. (2011), 'Gas-liquid-liquid slug flow for improving liquid-liquid extraction in miniaturized channels', *Industrial and Engineering Chemistry Research* **50**(8), 4672–4677.

Araújo, J. D. P., Miranda, J. M. and Campos, J. B. L. M. (2013*a*), 'Flow of two consecutive Taylor bubbles through a vertical column of stagnant liquid-A CFD study about the influence of the leading bubble on the hydrodynamics of the trailing one', *Chemical Engineering Science* **97**, 16–33.

Araújo, J. D. P., Miranda, J. M. and Campos, J. B. L. M. (2015), 'CFD Study of the Hydrodynamics of Slug Flow Systems: Interaction between Consecutive Taylor Bubbles', *International Journal of Chemical Reactor Engineering* **13**(4), 541–549.

Araújo, J., Miranda, J. and Campos, J. (2013*b*), 'Simulation of slug flow systems under laminar regime: Hydrodynamics with individual and a pair of consecutive Taylor bubbles', *Journal of Petroleum Science and Engineering* **111**, 1–14.

Araújo, J., Miranda, J., Pinto, A. and Campos, J. (2012), 'Wide-ranging survey on the laminar flow of individual Taylor bubbles rising through stagnant Newtonian liquids', *International Journal of Multiphase Flow* **43**, 131–148.

Bannwart, A. C., Rodriguez, O. M. H., de Carvalho, C. H. M., Wang, I. S. and Vara, R. M. O. (2004), 'Flow Patterns in Heavy Crude Oil-Water Flow', *Journal of Energy Resources Technology* **126**(3), 184.

Brackbill, J. U., Kothe, D. B. and Zemach, C. (1992), 'A Continuum Method for modeling surface tension', *Journal of Computational Physics* **100**, 335–354.

Brown, R. and Govier, G. (1961), 'High-Speed Photography in the Study of Two-Phase Flow', *The Canadian Journal of Chemical Engineering* **39**, 159–164.

Chapra, S. C. and Canale, R. P. (2006), *Numerical Methods for Engineers*, internatio edn, McGraw-Hill.

Collins, R., Moraes, F. F. D., Davidson, J. F. and Harrison, D. (1978), 'The motion of a large gas bubble rising through liquid flowing in a tube', *Journal of Fluid Mechanics* **89**(03), 497–514.

Davies, R. M. and Taylor, G. (1950), 'The Mechanics of Large Bubbles Rising through Extended Liquids and through Liquids in Tubes', *Proceedings of the Royal Society A: Mathematical, Physical and Engineering Sciences* **200**(1062), 375–390.

Direito, F. J. N., Campos, J. B. L. M. and Miranda, J. M. (2016), 'Rising of a single Taylor drop in a stagnant liquid – 2D laminar flow and axisymmetry limits', *Physics of Fluids* **28**(5), 057101.

Direito, F. J. N., Campos, J. and Miranda, J. M. (2017), 'A Taylor drop rising in a liquid co-current flow', *International Journal of Multiphase Flow* .

Direito, F. J. N., Morgado, A. O., Rocha, L. A. M., Miranda, J. M. and Campos, J. B. L. M. (2017), 'Experimental and numerical 3D study of a Taylor drop rising in a stagnant heavier liquid', *Physics of Fluids* **29**(3), 037109.

Fabre, J. and Line, A. (1992), 'Modeling of 2-Phase Slug Flow', *Annual Review of Fluid Mechanics* **24**, 21–46.

Govier, G., Sullivan, G. and Wood, R. (1961), 'The Upward Vertical Flow of Oil-Water Mixtures', *The Canadian Journal of Chemical Engineering* **39**, 67–75.

Govier, G. W. and Aziz, K. (1972), *The Flow of Complex Mixtures in Pipes*, Van Nostrand Reinhold Co., New York.

Hasan, A. and Kabir, C. (1990), 'A New Model for Two-Phase Oil/Water Flow: Production Log Interpretation and Tubular Calculations', *SPE Production Engineering* **5**(May), 193–199.

Hayashi, K., Kurimoto, R. and Tomiyama, A. (2011), 'Terminal velocity of a Taylor drop in a vertical pipe', *International Journal of Multiphase Flow* **37**(3), 241–251.

Hirt, C. W. and Nichols, B. D. (1981), 'Volume of Fluid (VOF) Method for the Dynamics of Free Boundaries', *Journal of Computational Physics* **39**, 201–225.

Issa, R. I. (1986), 'Solution of the implicitly discretised fluid flow equations by operator-splitting', *Journal of Computational Physics* **62**(1), 40–65.

Jovanović, J., Zhou, W., Rebrov, E. V., Nijhuis, T. A., Hessel, V. and Schouten, J. C. (2011), 'Liquid-liquid slug flow: Hydrodynamics and pressure drop', *Chemical Engineering Science* **66**(1), 42–54.

Kurimoto, R., Hayashi, K. and Tomiyama, A. (2013), 'Terminal velocities of clean and fully-contaminated drops in vertical pipes', *International Journal of Multiphase Flow* **49**, 8–23.

Leonard, B. P. (1979), 'A stable and accurate convective modelling procedure based on quadratic upstream interpolation', *Computer Methods in Applied Mechanics and Engineering* **19**(1), 59–98.

Liu, X.-m., Zhong, H.-q., Li, Y.-c., Liu, Z.-n. and Wang, Q. (2014), 'Experimental study of flow patterns and pressure drops of heavy oil-water-gas vertical flow', *Journal of Hydrodynamics, Ser. B* **26**(4), 646–653.

Mandal, T., Das, G. and Das, P. (2008), 'Motion of Taylor Bubbles and Taylor Drops in Liquid-Liquid Systems', *Industrial & Engineering Chemistry Research* **47**(18), 7048–7057.

Mandal, T., Das, G. and Das, P. (2010), 'An appraisal of liquidliquid slug flow in different pipe orientations', *International Journal of Multiphase Flow* **36**(8), 661–671.

Mandal, T. K., Das, G. and Das, P. K. (2007), 'Prediction of rise velocity of a liquid Taylor bubble in a vertical tube', *Physics of Fluids* **19**(12), 128109.

Mandal, T. K., Das, G. and Das, P. K. (2009), 'Liquid Taylor Bubbles Rising in a Vertical Column of a Heavier Liquid: An Approximate Analysis', *Journal of Fluids Engineering* **131**(1), 011303.

Moissis, R. and Griffith, P. (1962), 'Entrance Effects in a Two-Phase Slug Flow', *Journal of Heat Transfer* **84**(1), 29.

Morgado, A., Miranda, J., Araújo, J. and Campos, J. B. (2016), 'Review on vertical gas-liquid slug flow', *International Journal of Multiphase Flow* **85**, 348–368.

Mydlarz-Gabryk, K., Pietrzak, M. and Troniewski, L. (2014), 'Study on oilwater two-phase upflow in vertical pipes', *Journal of Petroleum Science and Engineering* **117**, 28–36.

Nicklin, D., Wilkes, J. and Davidson, J. (1962), 'Two-Phase Flow in Verical Tubes', *Trans. Inst. Chem. Eng* **40**.

Oddie, G., Shi, H., Durlofsky, L. J., Aziz, K., Pfeffer, B. and Holmes, J. A. (2003), 'Experimental study of two and three phase flows in large diameter inclined pipes', *International Journal of Multiphase Flow* **29**(4), 527–558.

Patankar, S. V. (1980), *Numerical Heat Transfer And Fluid Flow*, Hemisphere.

Pinto, A. and Campos, J. (1996), 'Coalescence of two gas slugs rising in a vertical column of liquid', *Chemical engineering science* **51**(1), 45–54.

Rocha, L. A. M., Miranda, M. and Campos, J. B. L. M. (2017), 'Wide Range Simulation Study of Taylor Bubbles in Circular Milli and Microchannels', *Micromachines* **8**(5), 154.

White, E. and Beardmore, R. (1962), 'The velocity of rise of single cylindrical air bubbles through liquids contained in vertical tubes', *Chemical Engineering Science* **17**(5), 351–361.

Youngs, D. L. (1982), Time-Dependent Multi-Material Flow with large Fluid Distorsion., *in* K. W. Morton and M. J. Baines, eds, 'Numerical Methods in Fluid Dynamics', Academic Press.

Zhang, H.-Q., Sarica, C. and Pereyra, E. (2012), 'Review of High-Viscosity Oil Multiphase Pipe Flow', *Energy & Fuels* **26**(7), 3979–3985.

Zukoski, E. E. (1966), 'Influence of viscosity, surface tension, and inclination angle on motion of long bubbles in closed tubes', *Journal of Fluid Mechanics* **25**(04), 821.

7

Conclusions

7.1 Research conclusions

The importance of multiphase flows in industry in general, with a particular focus on petroleum exploitation and transport, justifies the pursuit of a deeper knowledge of a very relevant flow pattern, slug flow. While gas-liquid slug flow is already widely understood, liquid-liquid slug flow knowledge is still incomplete, albeit being extremely relevant. This motivated the present work.

The pursuit of that knowledge must start by observing its most basic characteristics and, afterwards, adding new complexities in order to reach a full description. Hence, the present work focused firstly on understanding the flow of an axisymmetric isolated Taylor drop in a stagnant liquid in a vertical tube. Afterwards, features such as asymmetries, co-current flow and drop interaction were added to the already studied scenarios.

In order to fulfill the objectives, the strategy employed was to use numerical tools. Using such tools, it is possible to easily create different, but relevant, operating conditions, as well as collecting a significant amount of data, such as drop shapes and velocity fields. The phenomena were modeled both in two dimensions (with axisymmetry) and three dimensions. The former is faster but limited in range due to the axisymmetry limits. The 3D model is of broader applicability, but extremely heavy for computation. Both models were validated through literature and in-house lab results. The numerical simulations were performed with a reference frame attached to the drop nose in order to reduce computational efforts.

The numerical simulations were planned in order to highlight the relevant forces (buoyancy, viscous, interfacial tension and inertia) through representative dimensionless numbers, following the practice of gas-liquid and liquid-liquid slug flow literature studies. Hence, drop shape, velocity field and drop velocity (through Froude number for stagnant continuous phase) were presented as functions of Morton and Eötvös numbers, as well as viscosity ratio, which is relevant in liquid-liquid flows. Hence, 2D model was found to be valid in the range $0.01 < \mu^* < 40$, $8 < Eo < 30$ and $2.32 \times 10^{-6} < M < 100$, with Eötvös number and Morton number ranges limited for the lower viscosity ratio values. Outside this range, it was necessary to used the 3D model. The 3D model was applied to the range: $0.01 < \mu^* < 100$, $8 < Eo < 30$ and $2.32 \times 10^{-6} < M < 100$, and was not limited in the lower viscosity ratio values.

For drops rising in stagnant continuous phase, Froude number was found to decrease with increasing viscosity ratio. Furthermore, high influence of interfacial tension (low Eötvös number values) also lowered Froude number. Froude also decreases with increasing Morton number values. Eötvös number greatly affects the drop shape, especially the drop bottom. Low Eötvös number correspond to a bulky and rounded shaped bottom, while an increase in Eötvös tends to flatten the bottom and elongate the drop.

The disturbed distance below the drop depends mainly on the drop Reynolds number (which can be computed by combining the aforementioned dimensionless numbers). It stays in fairly constant and low values until starting to increase in the region between drop Reynolds number 10 and 100. The drops in the studied range do not show closed recirculations.

Due to the increased stresses in liquid-liquid flows, the maximum downward velocity in the film along the radial direction can be located, unlike gas-liquid flows, in the middle of the film and not at the liquid-liquid interface.

Regarding the drop shape asymmetries, three ranges of viscosity ratio are relevant. For an intermediate range, drops are axisymmetric. Asymmetries appear for low viscosity ratio values. For high viscosity ratios, drops body tends to show a serpentine like movement. Comparison between 2D and 3D data show that the 2D model cannot predict well higher Froude number cases (low viscosity ratio, high Eötvös number and low Morton number).

The combination of low interfacial force and high viscosity of both liquids leads to oscillations in the drop body. These are related to the imbalance caused by small perturbations at the interface. An analogous behavior happens in the drop bottom due to the decrease of the interfacial force when combined with low viscosity of the liquids.

When co-current is introduced, the balance between gravity and convective co-current effects was found to be determinant to the drop behavior. The increase in the continuous phase velocity promotes inertial effects, causing closed recirculations to appear, at the drop bottom, for low Eötvös. Some closed recirculations are separated from the drop bottom by a small portion of non-circulatory fluid, flowing at the drop velocity. For high Eötvös number, the velocity increase of the continuous phase may also anticipate the occurrence of shape oscillations, particularly at low Morton number values. High enough continuous phase velocity also causes the inner (around the tube axis) portion of the flow to move, in average, at the drop velocity.

In co-current, the flow stabilization distance below the drop was found to follow a similar trend to the Taylor drop flowing in stagnant continuous phase.

Regarding the drop velocity in co-current, a linear dependence on the continuous phase velocity was found, confirming for liquid-liquid flow the observations pre-existing for gas-liquid. Furthermore, a pre-existing gas-liquid correlation that predicts drop velocity in co-current was adapted to cover the liquid-liquid results.

A most interesting result concerns the fact that micro scale was found to be a lower limit for the macro scale drop velocity. The increase of the viscosity ratio approximates the macro scale results to that limit.

The interactions between two drops was also studied, both in stagnant and flowing continuous phase. As predicted by the low influence distances of the isolated drops, coalescence in axisymmetric conditions is very limited.

Overall, the present study succeeded in describing relevant phenomena regarding liquid-liquid slug flow. Further studies are, though, necessary for a full understanding.

7.2 Other considerations

The present work was motivated mainly by the oil water slug flow due to its importance on petroleum industry. However, it soon became clear that this specific application would lay in the non-symmetric part of the range (in the region of serpentine-like drops), which was difficult to study due to the high computational effort required. This fact does not diminish, in any way, the usefulness of what was done in this study, but represents, clearly, a challenge that is still to be overcome. Hence, one of the next steps should focus on studying this range, both through numerical simulation and in lab/pilot experiments (which provide validation to the simulations)

Further work regarding co-current flow and coalescence (in particular, for the non-symmetric ranges) is also required for the complete understanding of liquid-liquid slug flow and, eventually, to produce a one-dimensional algorithm that would easily be used in industry to deal with or create slug flow, depending on each ones requirements.

The usefulness and interest in this work is proven by the publication in relevant journals. It is however important to point the limitations of the present work. They are mainly caused by the difficulties of working with liquid-liquid systems both in lab and in computational simulations. In the lab, the liquid-liquid systems are extremely sensible to the drop injection method and the storage of dispersed phase at the top of the installation is a challenge that does not exist in gas-liquid flows. Moreover, with the need of using 3D simulations, which are extremely costly in terms of computational resources, it is more difficult to study the full range of liquid-liquid flows.

Despite the limitations and the work that has still to be done, the present thesis successfully advanced in slug flow knowledge.